Design of Photonic Crystal Surface Emitting Lasers and the Realisation of Coherently Coupled Arrays

Richard James Edward Taylor

University of Sheffield

Department of Electronic and Electrical Engineering

Thesis submitted to the University of Sheffield for the Degree of Doctor of Philosophy

January 2015

“Nothing is so dangerous to the progress of the human mind than to assume that our views of science are ultimate, that there are no mysteries in nature, that our triumphs are complete and that there are no new worlds to conquer”

- Sir Humphrey Davy

Abstract

This thesis describes developments in all-semiconductor photonic crystal surface emitting lasers (PCSELs).

Initially, band structure modelling is used to examine the effect of varying atom radius on the photonic crystal (PC) band structure for cylindrical atoms on a square lattice. This is used to determine the coupling coefficients of PCSEL structures and to examine the nature of the modes (leaky/non-leaky). Two areas of interest are found which are expected to give high Q-factor, and high power PCSELs. Design limitations are discussed.

Wave guide modelling shows that all-semiconductor PCSELs have a higher PC mode overlap than void containing PCSELs for a number of structures operating at different wavelengths (different material types). More complex waveguide structures are explored, highlighting the need for careful design for void containing structures. For practically realisable PCSELs, significant advantages, in terms of choice of atom size and the selection of suitable in-plane and out-of-plane coupling coefficients, are observed for all-semiconductor structures.

Finally, a coherent 2D array of band edge PCSELs is demonstrated for the first time. Individual PCSELs are characterised and shown to have a lower threshold current density and divergence than previously studied all-semiconductor PCSELs. The 2D array of PCSELs is shown to have electronic control of coherence, with custom interference patterns possible. The individual PCSELs in the array are electronically and thermally isolated, with electronically controlled optical isolation. This offers new routes to power scaling of coherent arrays.

Acknowledgements

First and foremost, I would like to thank my supervisor Professor Richard Hogg for his tireless effort helping me with this thesis, my publications, and research in general, fellowship applications, supporting me in Japan, editing figures, and everything else. None of my achievement would have been possible without his support, and for that I will always be grateful.

I would like to thank the other people involved in this project Dr David Williams, Ian Tooley, Alex Crombie, Dr Nasser Babazadeh, Dr Ken Kennedy, Dr Ben Stevens, Dr Salam Khamas, and Dr Pavlo Ivanov. Their help and support has been invaluable. Special thanks must go to Dr David Childs, for helping in the lab and for Dave Wednesdays.

For Belgium beers, dinners and visits to Bruges I thank Nicky, Mike, Peter and Graham Goldberg.

Finally, for love and support through all my endeavours, and for putting up with me thus far. I would like to thank my parents John Taylor and Mandy Payton, my sisters Kate Skelton and Sophie Taylor, my niece and nephew London and Bentley Skelton, my brother in law Marcus Skelton and my girlfriend Izzy Jasper.

Publications

[1] D. M. Williams, K.M. Groom, D. Childs, R.J.E. Taylor, S. Khamas, R.A. Hogg, B.J Stevens, N. Ikeda, Y. Sugimoto

“Optimisation of coupling between photonic crystal and active elements in an epitaxially regrown GaAs based photonic crystal surface emitting laser”

Japanese Journal of Applied Physics, 51, 02BG05-1-3, February 2012

[2] D. M. Williams, K.M. Groom, D. Childs, R.J.E. Taylor, S. Khamas, R.A. Hogg, B.J. Stevens, N. Ikeda, Y. Sugimoto

“Epitaxially regrown GaAs-based photonic crystal surface emitting laser”

IEEE Photonics Technology Letters, 24, 11, 966-968, June 2012

[3] D. M. Williams, K.M. Groom, B.J Stevens, Q. Jiang, D. Childs, R.J.E. Taylor, S. Khamas, R.A. Hogg, N. Ikeda, Y. Sugimoto

“Realization of a photonic crystal surface emitting laser through GaAs based regrowth”

Proceedings of SPIE – The International Society for Optical engineering, 8255, Jan 2012

[4] Richard J E Taylor, David M Williams, Jon R Orchard, David T D Childs, Salam Khamas and Richard A Hogg

“Band structure and waveguide modelling of epitaxially regrown photonic crystal surface emitting lasers”

Journal of Physics D, 46, 26, 264005(8pp), July 2013

[5] R. J. E. Taylor, D.M. Williams, D.T. D. Childs, B.J. Stevens, L. R. Shepherd, S. Khamas, K.M. Groom, R.A. Hogg, N. Ikeda, and Y. Sugimoto

“Photonic crystal surface emitting lasers based on epitaxial regrowth”

IEEE Journal of Selected Topics in Quantum Electronics, 19, 4, 4900407, July 2013

Patent Application

[1] R.J.E. Taylor, D.T.D Childs, R.A. Hogg

“Improved laser design”

UK Patent Application Number 1414984.3

Conference Oral Presentations

[C1] R. J. E. Taylor, D.T. D. Childs, A. Crombie, B.J. Stevens, N. Babazadeh, K.M. Groom, G. Ternent, S. Thoms, H. Zhou, P.S. Ivanov, J. Sarma, S. Khamas and R.A. Hogg

“Coherently Coupled Photonic Crystal Surface Emitting Lasers”

International Semiconductors Lasers Conference 2014, Mallorca

[C2] R. J. E. Taylor, A.J. Crombie, P. Ivanov, D.T. D. Childs, S. Khamas, R.A. Hogg,

“Waveguide design of all-semiconductor photonic crystal surface emitting lasers”

International conference on optical, optoelectronic and photonic materials and applications 2014 , Leeds

[C3] R. J. E. Taylor, D.M. Williams, D.T. D. Childs, B.J. Stevens, L. R. Shepherd, S. Khamas, K.M. Groom, R.A. Hogg, N. Ikeda, and Y. Sugimoto

“Design Study: Photonic Crystal Surface Emitting Lasers”

UK semiconductor conference 2013, B-O-5, Sheffield

[C4] R. J. E. Taylor, D.M. Williams, D.T. D. Childs, B.J. Stevens, L. R. Shepherd, S. Khamas, K.M. Groom, R.A. Hogg, N. Ikeda, and Y. Sugimoto

“Photonic crystal surface emitting lasers based on epitaxial regrowth”

International semiconductor lasers conference 2012

[C5] R. J. E. Taylor, D.M. Williams, D.T. D. Childs, B.J. Stevens, S. Khamas, K.M. Groom, R.A. Hogg, N. Ikeda, and Y. Sugimoto

“Photonic crystal surface emitting lasers based on epitaxial regrowth”

UK semiconductor conference 2012, B-O-8

[C6] R. J. E. Taylor, D.T. D. Childs, A. Crombie, B.J. Stevens, N. Babazadeh, K.M. Groom, G. Ternent, S. Thoms, H. Zhou, P.S. Ivanov, J. Sarma, S. Khamas and R.A. Hogg

“Photonic crystal surface emitting lasers based on epitaxial regrowth” (Invited presentation)

16th International conference laser optics 2014, St Petersburg

[C7] R. J. E. Taylor, D.T. D. Childs, A. Crombie, B.J. Stevens, N. Babazadeh, K.M. Groom, G. Ternent, S. Thoms, H. Zhou, P.S. Ivanov, J. Sarma, S. Khamas and R.A. Hogg

“Photonic crystal surface emitting lasers based on epitaxial regrowth” (Invited presentation)

Progress In Electro-magnetics Symposium, 2014, Guangzhou

Awards and prizes

[A1] Japanese society for the promotion of science (JSPS) summer fellowship award 2014

[A2] Institution of engineering and technology (IET) postgraduate scholarship award 2014

Contents

1. Introduction

This chapter describes photonic crystal (PC) lasers and reviews progress made in the field of photonic crystal surface emitting lasers (PCSELs). Initially photonic crystal lasers are introduced, design of the photonic crystal is discussed, growth methods for PCSELs are described, key achievements in PCSELs are highlighted, and gaps in the existing knowledge are explored. Finally, the remainder of this thesis is outlined.

1.1 Photonic Crystal Lasers

This section describes the operating principles of PSCELs. Initially, definitions which will be used throughout this thesis are outlined, the origin of the photonic band structure is described, and finally operating principles of band edge and micro cavity lasers are discussed.

Band Edge Laser

In general, wave propagation is altered in a material where the propagation of the wave is modulated. In an atomic crystal (i.e. a semiconductor) it is the periodic variation in potential that determines the propagation of electrons through the material, while in a photonic crystal the periodic variation in refractive index determines the propagation of photons [1]. In this respect a photonic crystal can be considered analogous to a semiconductor crystal, and there is significant read across in terminology.

Light travelling within a PC will be scattered at the interfaces of refractive index variation. For a square lattice, light is scattered in orthogonal directions. Figure 1.1 shows the directions of wave scattering for a wave travelling in a 2D photonic crystal with circular atoms on a square lattice, blue arrows indicate in-plane scattering and red arrows out-of-plane scattering [2,3].

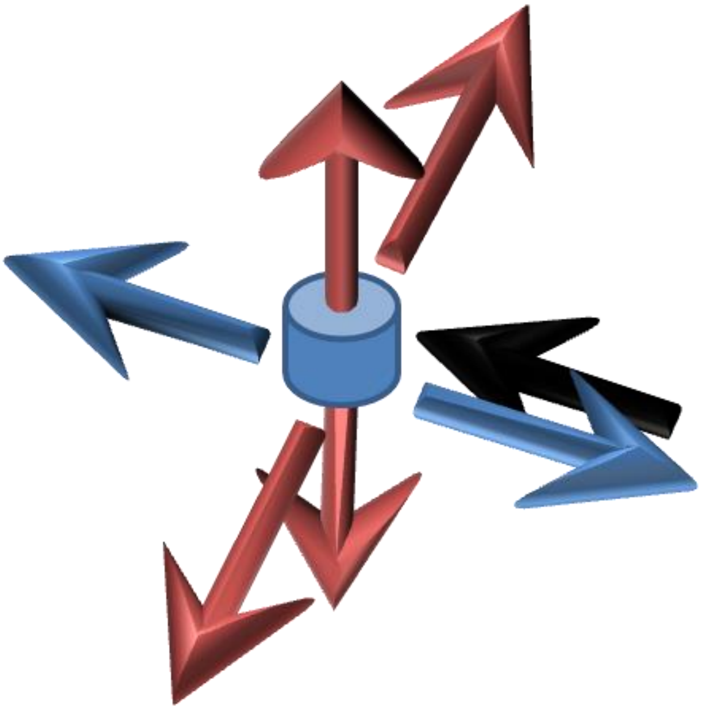

Figure 1.1 scattering direction for a PC with a square lattice where first order scattering (red), second order scattering and wave propagation (blue) are shown

Scattered light can interfere constructively or destructively, this interference results in permitted and forbidden energies [4]. Solving Maxwell's equations (discussed in detail in chapter 3) it is possible to plot the photonic band structure which is similar to a semiconductor electronic band structure showing the allowed photonic energy levels as a function of wave vector. Figure 1.2 shows the photonic band structure of a photonic crystal with circular atoms on a square lattice, the band edges are shown (in this case the band structure is modelled using Massachusetts institute of Technology (MIT) photonic bands [5,6] (MPB)).

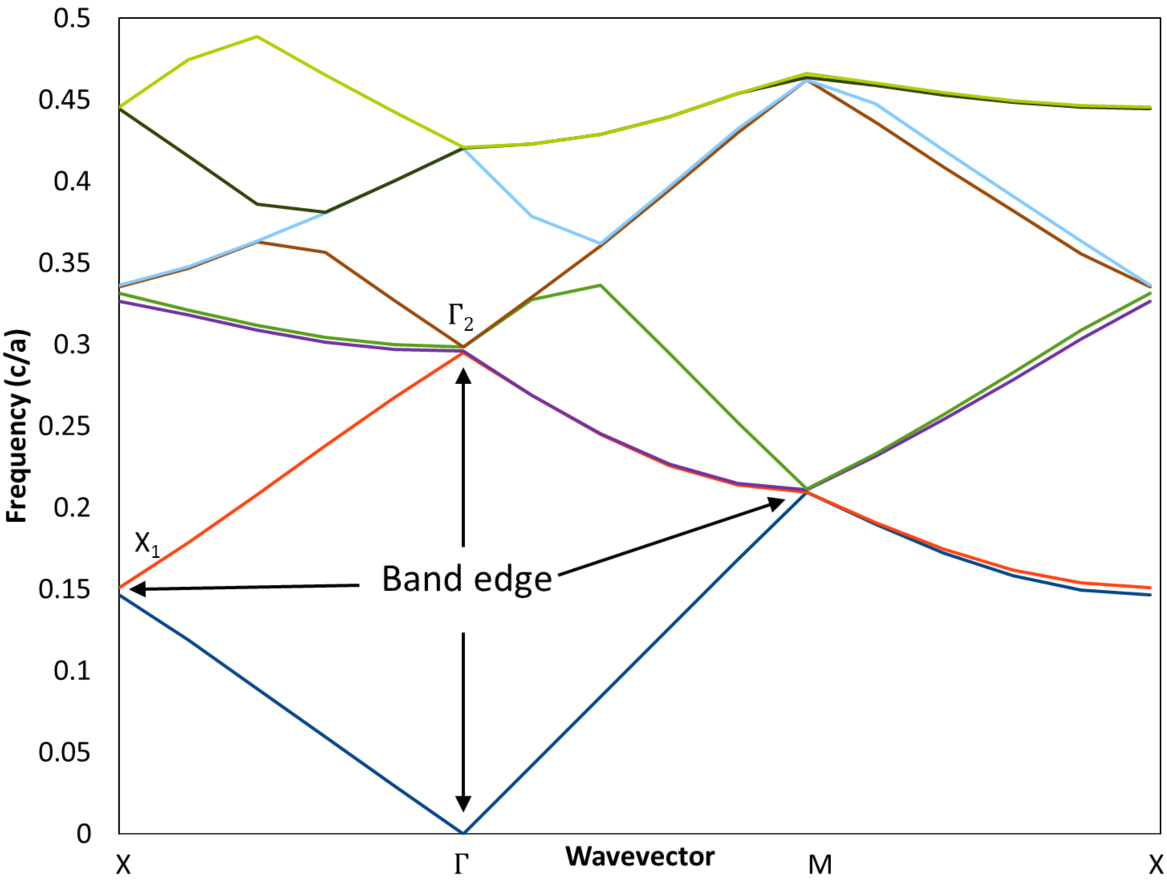

Figure 1.2 modelled band structure of a PC consisting of circular atoms on a square lattice

For a square lattice light travelling within the PC region will experience multiple Bragg diffractions. Light travelling in-plane is scattered in perpendicular directions (+90º and -90 º) because of first order diffraction and backwards due to second order diffraction (see figure 1.1). In a photonic band structure a band edge is a region where the gradient is zero. At this point, in-plane resonant modes (standing wave at the Γ point) are also diffracted out-of-plane due to first order Bragg diffraction. Different band edges correspond to coupling of different waves, and for a square lattice (shown in figure1.2) the X_1 band edge corresponds to coupling of forward and backward directions (the same feedback as used in a DFB), the Γ_2 band edge corresponds to coupling of orthogonal in-plane and vertical emission out of plane. It is the diffraction out-of-plane that causes surface emission in a PCSEL.[7]

The in-plane scattering of a PCSEL results in light being emitted from the whole PC surface. Emission from the whole surface of the PC gives PCSELs the promise of power which scales with area (and may therefore be large), gives low divergence, and excellent beam shape (i.e. $M^2=1$).

Micro Cavity Laser

As discussed in the previous section, there are regions of the band structure which may have a band gap i.e. no states are allowed. There is no complete band gap shown in figure 1.2, regions where there are no states in a particular direction act as a stop band in this case. Light travelling within the band gap of the PC will be evanescent (i.e. it will decay exponentially). If a defect is introduced into the PC then a micro cavity is formed, whereby a single localised mode (for a point defect) or a number of modes (for a line defect) can be formed within the band gap. These micro cavities can be used to control light within the structure. Light within a defect is forbidden to travel through the crystal and will be trapped within the defect, hence the PC surrounding the defect acts to confine the light [8]. Figure 1.3 shows the schematic of point defect cavities where a) an atom has been removed and b) where an atom size has been increased in size.

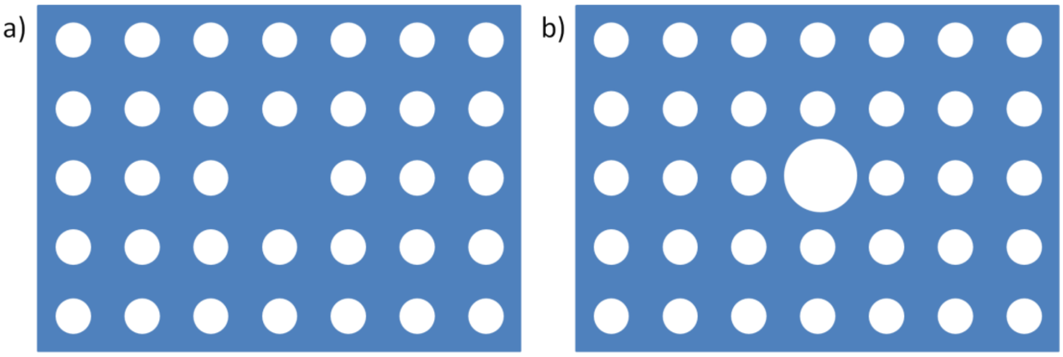

Figure 1.3 schematic of point defect cavities where one atom has been removed a) and one atom has an increased radius b)

Line defects can be fabricated by removing atoms in a line, these micro cavities have been used to, guide light along a wave guide [9] and have transmitted light around a sharp bend [10, 11]. Micro cavity lasers have a very low mode volume, which has led to lasing devices with extremely low threshold [12-14] and high Q-factors [15]. However the low modal volume of these devices limits them to low power. Generally the beam quality of these devices is low as the emission is highly divergent. Devices considered in this thesis are band edge lasers, not micro cavity structures.

1.2 Photonic Crystal Design

There has been a significant attempt in the past to optimise the PCSEL design. This has included:

- Changing the lattice geometry of the PC layer [16-18],
- Changing the atom shape of the PC [19], and
- Designing the wave guide [20].

This section considers the attempts to optimise the PCSEL design in these ways. Initially typical lattice geometries and their respective band structures are shown, then how the atom shape affects polarisation, output power and far field pattern of PCSELs is discussed.

Lattice Geometry

The lattice of a 2D photonic crystal has been extensively considered, typical lattice geometries include square [16], triangular [17] and Kagome [18] structure. Figure 1.5 a) shows a schematic of square, triangular and Kagome PC lattice structures, respectively. By changing the lattice geometry of a PC the symmetric directions change and hence the band structure is different. Given that for a band edge laser lasing occurs where the band is flat, different lattice shapes will give lasing in different directions.

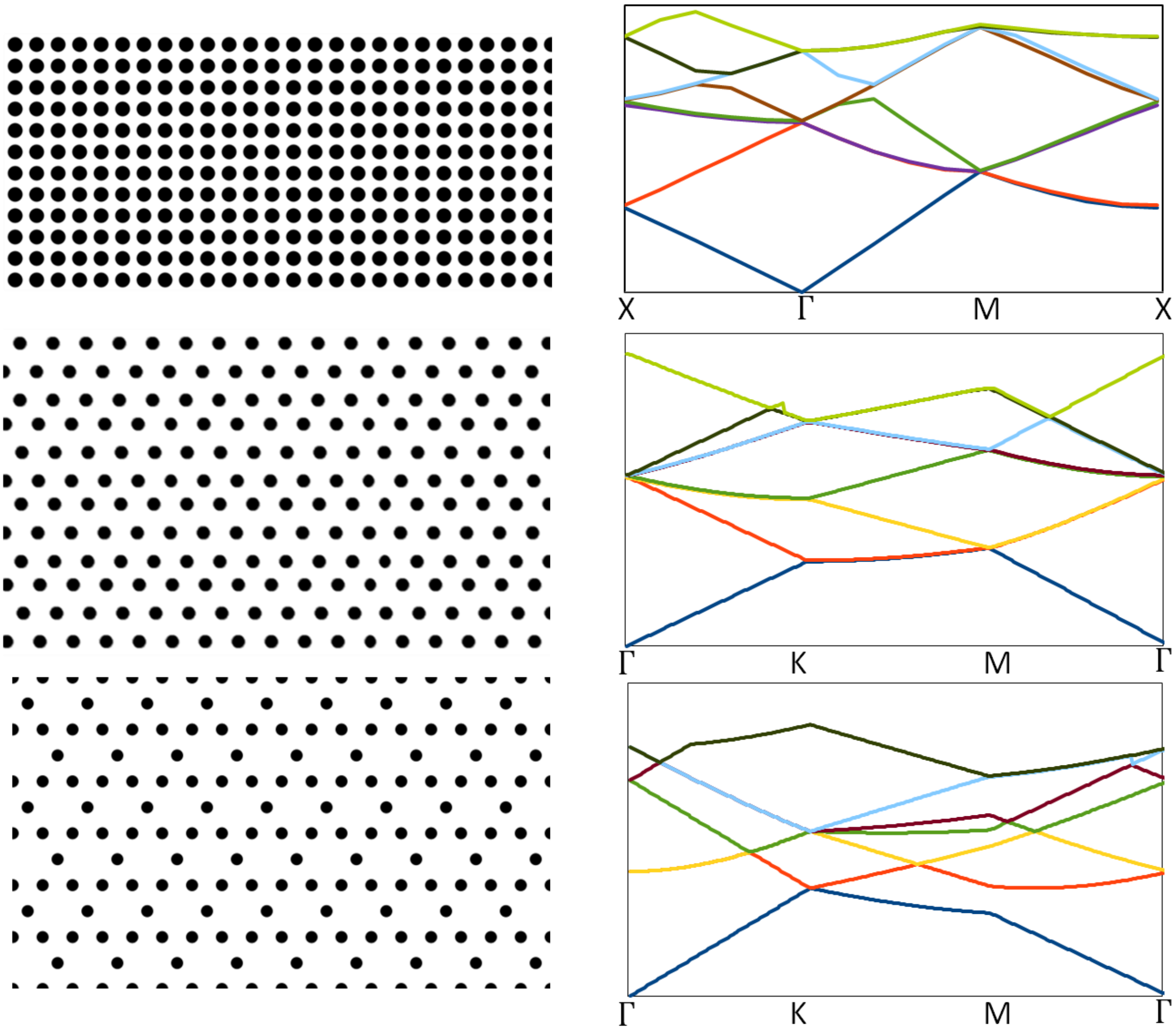

Figure 1.4 schematic of 2D photonic crystal square, triangle and Kagome lattice with associated band structures

Changing the lattice of a PC changes the number and direction of symmetric wave vectors within the structure, which changes the band structure, figure 1.4 shows the band structure of a) square b) triangle and c) Kagome lattice. A square lattice is generally chosen for PCSELs due to the simplicity of design and fabrication as there are fewer modes at the Γ point as compared to triangular PCs.

Atom Shape

There have been extensive studies into the effect of changing the atom shape within a photonic crystal. Initial studies on PCs focussed primarily on circular atoms, in part this was because circular atoms are easier to model and partly because they are easier to manufacture. However, the recent focus has been on changing the in-plane electric and magnetic fields of the PC which requires more complicated shapes.

The in-plane electric field determines the nature of the mode. If the in-plane electric field is anti-symmetric about the centre of the atom then light scattered in a vertical direction will be in anti-phase and will interfere destructively. This mode will therefore emit little light out-of plane and will be “non-leaky” [19]. If the in-plane electric field is not anti symmetric about the centre of the atom then the mode will be “leaky”. Leaky modes within a laser structure will act as a loss mechanism, prior to threshold being reached. As a result there is a fundamental issue in PCSEL design. The lowest threshold gain mode have the lowest output power. As discussed later, a perfectly circular PC should have ~zero output power. The engineering of the atom shape to deliver high output powers from the PCSEL is discussed later in this section. Additionally the polarisation of the lasing light can be determined by the in-plane electric field as well [21]. Directionally unified electric field vectors (shown in left had side of figure 1.5) lead to linear polarisation. Electric field vectors that are not directionally unified (shown in right hand side figure 1.5) do not have a singularly defined polarisation of the emitted light, these electric fields may exhibit polarisation mode hopping as with VCSELs, the polarisation may be random, or it may not be linearly polarised, and determining this from the model alone is difficult.

In general a PC consisting of circular atoms on a square lattice will, at the gamma point, give 4 bands where the in-plane electric field of two bands will give electric fields that are directionally unified and two bands that are anti symmetric about the centre of the atom [21]. Figure 1.5 shows the in-plane electric and magnetic fields of four bands at the gamma point for a PC with circular atoms on a square lattice, where amplitudes of the magnetic field perpendicular to the plane are indicated with red and blue denoting negative and positive, respectively, black circles represent the edge of the atom and black arrows represent in-plane electric field with arrow size representing magnitude. Plots a and b clearly have an electric field pattern that is directionally unified while plots c and d have an electric field pattern that is anti symmetric about the centre of the atom.

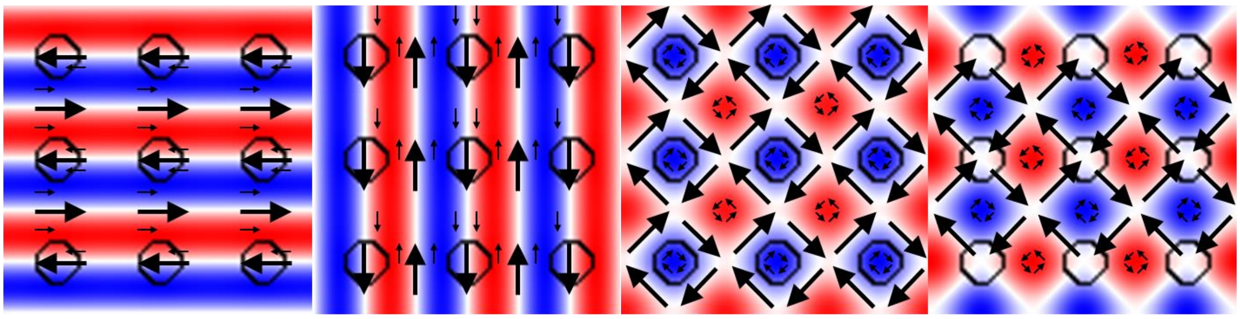

Figure 1.5 in-plane electric and magnetic fields of four bands at the gamma point for a PC with circular atoms on a square lattice, where amplitudes of the magnetic field perpendicular to the plane are indicated with red and blue denoting negative and positive, respectively, black circles represent the edge of the atom and black arrows represent in-plane electric field with arrow size representing intensity.

As discussed previously, the lowest threshold lasing band will have a low output power. By changing the atom shape it is possible to change the in-plane electric and magnetic field distribution of a PC, in particular the symmetry can be broken and the coupling can be controlled. Yokoyama *et, al.,* [21] and Noda *et, al.,* [22] demonstrated that they could obtain a PC which had a square lattice where each of the 4 gamma point bands have a directionally unified electric and magnetic field. This was achieved in a number of ways. Firstly they included additional atoms within the structure and secondly they changed from a circular atom to an oval shaped atom. Figure 1.6 shows the shapes considered in Yokoyama *et, al.,*

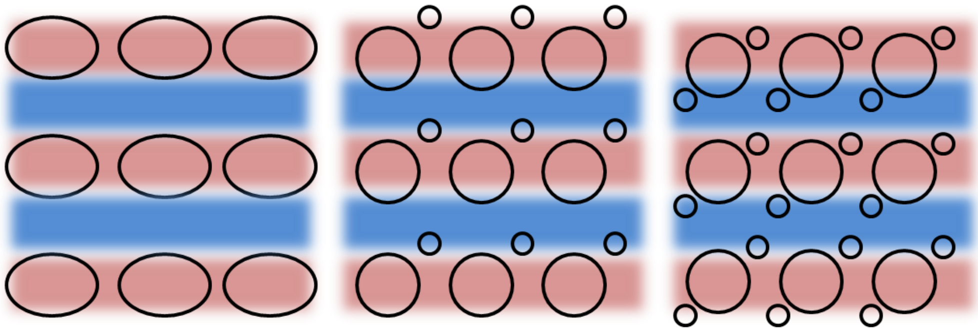

Figure 1.6 in-plane electric and magnetic fields of structures from Yokoyama *et, al.,* [21] where amplitudes of the magnetic field perpendicular to the plane are indicated with red and blue denoting negative and positive, respectively, black circles represent the edge of the atom

By changing from a circular to a triangular atom the output power was increased [19, 23]. Kurosaka *et, al.,* modelled PC atom shape, starting with a diamond shape and changing the shape to maximise to the output power of the device. Figure 1.7 shows the atom shapes considered. Initially a diamond was considered, through various modelling iterations the symmetry was modified until the atom was a triangular shape and then a chevron.

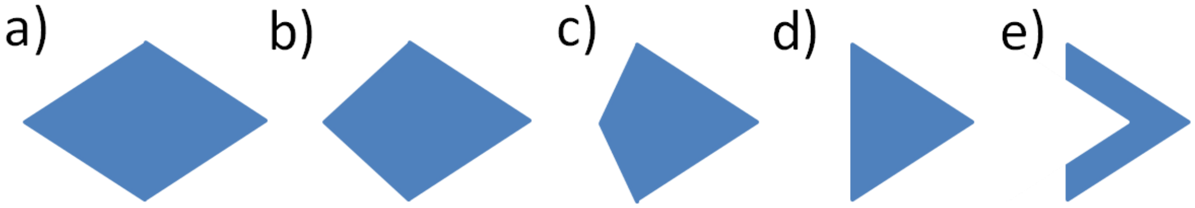

Figure 1.7 atom shapes from Kurosaka *et, al.*,[19]

Following on from this work, further attempts were made to break the symmetry of the PC by rotating and shifting the position of the atoms [23]. Figure 1.8 shows atom orientations considered in Kurosaka *et, al.*, [23]Figure 1.8 a) shows a square lattice of chevrons c) shows a square lattice of chevrons where chevrons are rotated and b) shows a square lattice of chevrons where adjacent chevrons are rotated by 90° and adjacent columns are shifted by half a period. Changing the atom orientation in this way changed the in-plane electric field and the band structure. As the symmetry is reduced the number of lattice points increase within the first brillouin zone and so the number of bands increases.

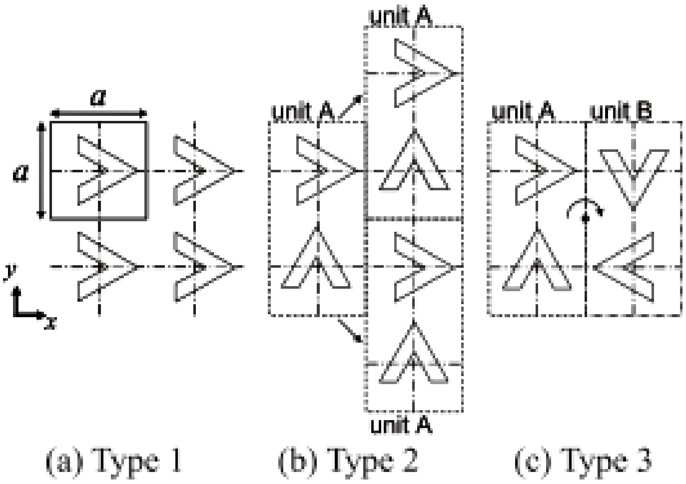

Figure 1.8 atom orientations considered in Kurosaka *et, al.*,[23]

The most recent work on atom shape by Hirose *et, al.*, [24] demonstrates watt level power from a single device. A right-angle-triangle was used as the atom shape which (along with using regrowth) was attributed to giving such high power. Figure 1.9 shows the atom shape used to produce a watt level PCSEL.

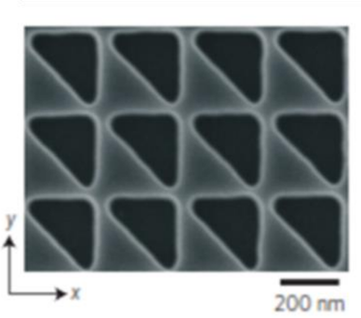

Figure 1.9 atom shape from Hirose *et, al.,* [24]

Control of far field has been shown in Miyai *et, al.,* [25]where for a void containing PCSEL with circular atoms on a square lattice gave an annular far field pattern and triangular atoms on a square lattice gave a circular far field pattern. Figure 1.10 shows:

a) a PC with circular atoms on a square lattice and the corresponding far field pattern,
b) a PC with circular atoms on a square lattice with a line defect,
c) a PC with circular atoms on a square lattice with a double line defect,
d) a PC with circular atoms on a square lattice with a cross defect,
e) a PC with circular atoms on a square lattice with multiple cross defects, and
f) a triangular atom on a square lattice.

The ability to realise a custom beam-shape tailored to the application was therefore demonstrated.

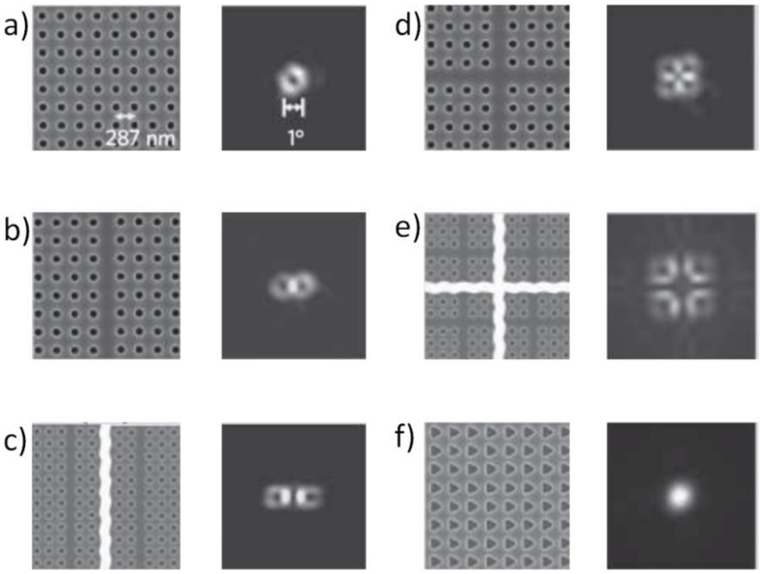

Figure 1.10 Lattice and farfeld patterns for lattices adapted from Miyai *et, al.,* [25]

In brief, a square lattice is chosen to minimise the number of bands. The circular atom is then replaced with lower symmetry features to enable power [19,24], or add higher order structure to the PC to tailor the beam shape [25] .

1.3 PCSEL Progress

This section describes some of the noteworthy accomplishments in the development of PCSELs.

Lasing

The first PCSEL was realised using an organic semiconductor by Berggren *et, al.,* [26]. A PC was etched into a SiO_2 layer and an organic gain medium was deposited within the etched holes. Lasing was reported at 830nm with the device being optically pumped.

The first laser action from a band edge inorganic semiconductor laser was demonstrated by Imada *et, al.*, in 1999 [27]. Where circular atoms of air on a background of InP were used on a triangular lattice. The PCSELs were fabricated through wafer fusion.

RT, CW, Single Mode

The first major step in any new semiconductor laser technology is to achieve room temperature, continuous wave, single mode emission. For PCSELs this was achieved by Ohnishi *et, al.*, in 2004 [28]. By using a GaAs based PC consisting of circular atoms on a square lattice fabricated by wafer fusion. A lasing power of 4mW was achieved with a threshold current of 70mA. Figure 1.11 shows the LI characteristics and spectra shown in Ohnishi *et, al.*, this result demonstrated the viability of PCSELs as a new type of PCSEL laser and was followed by development of PC design.

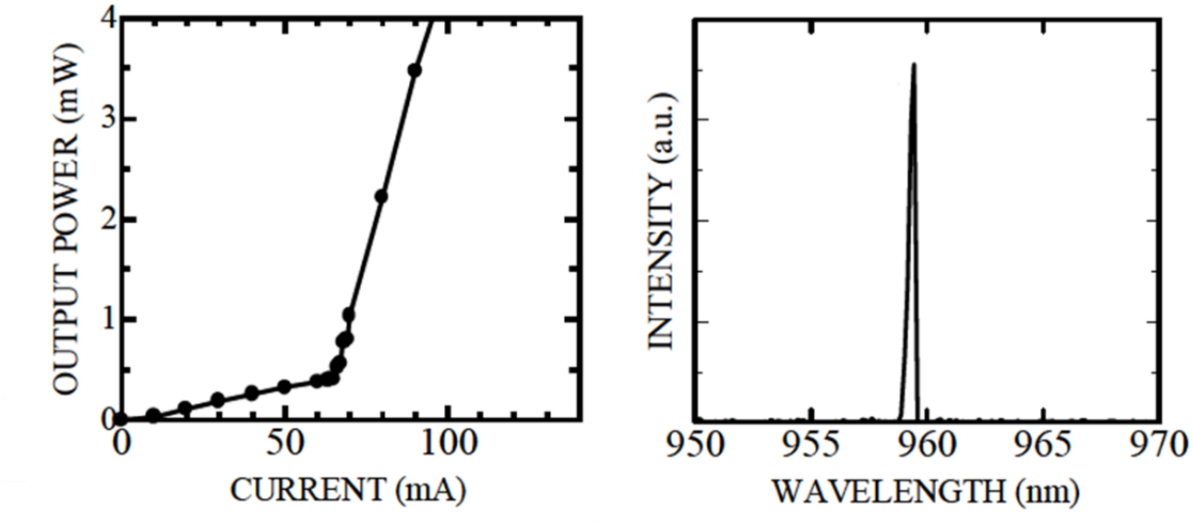

Figure 1.11 Li and spectra adapted from Ohnishi *et, al.*, [28]

Micro Cavity Coupling

Strong coupling between 2 micro cavities was demonstrated by Sato *et, al.*, in 2012 [29]. On a triangular lattice of air atoms on a GaAs background, 2 micro cavities were placed far apart (52 periods), with a line defect placed close to the micro cavities. Figure 1.12 shows the structure from Sato *et, al.*, Each micro cavity is a high Q-factor cavity consisting of an L3 defect (3 point defects in a row), and strong coupling between them is observed. Strong coupling is confirmed through the observation of Rabi oscillations, which was observed for 400ps with a period of 54ps. The coupling can be "turned off" by irradiation of a control pulse onto a remote cavity. The control of strong coupling in micro cavities has been proposed for applications in quantum information processing.

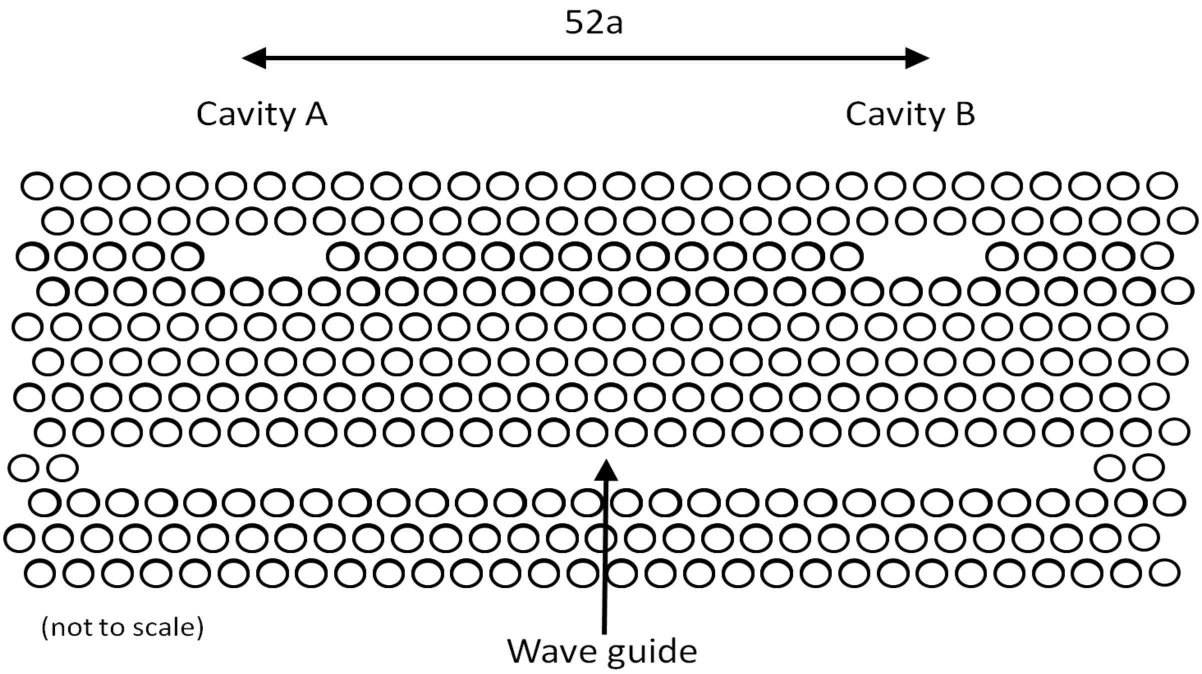

Figure1.12 schematic of 2 L3 cavities separated by 52a (not to scale) with a line defect acting as a coupler between them adapted from Sako *et, al.,* [29]

Beam Steering

Kurosaka *et, al.,* demonstrated beam steering from a single PCSEL chip in 2010 [30]. By varying the period of the PC across the device different device regions exhibited different emission angles, by controlling individual areas of the chip the emission angle of the device appears to shift and beam steering is achieved, the maximum beam steering observed was 60^{o}. Figure 1.13 shows the structure of the PC layer and the observed beam steering. The maximum beam steering is determined by the band structure of the various sections of the device, as the angle changes so does the origin of the emission.

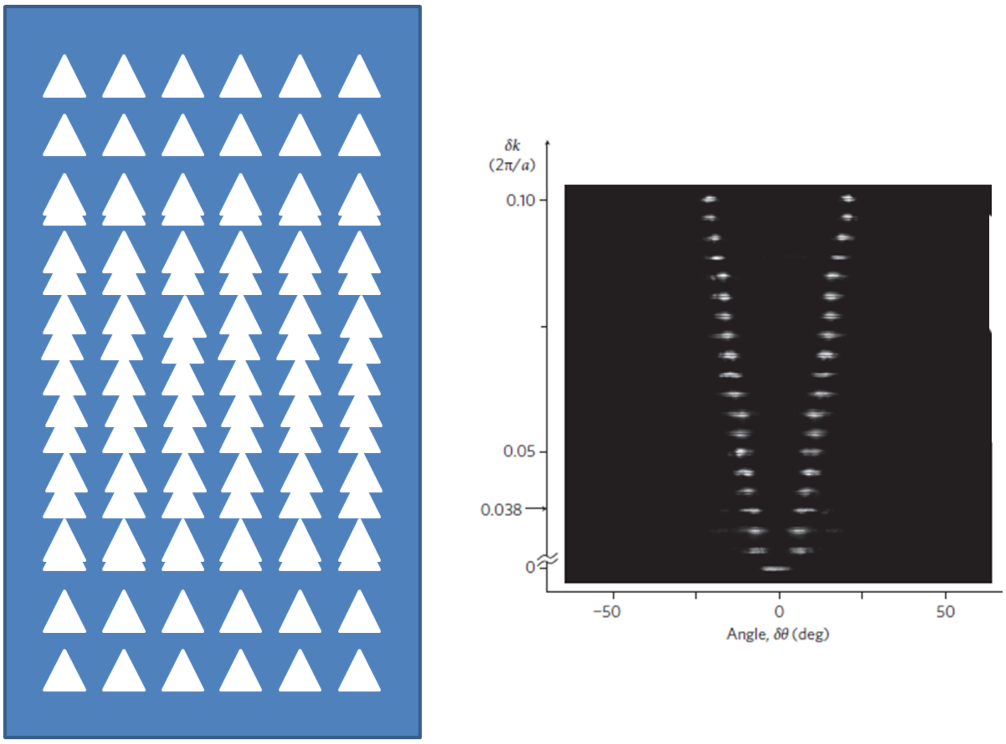

Figure1.13 lattice structure and demonstration of beam steering adapted from Kurosaka *et, al.,* [30]

Johnson *et, al.,* demonstrated beam steering from a 1 by 2 VCSEL array in 2013 [31]. In this structure a VCSEL is grown and a PC micro cavity region is etched into the top contact. A focused ion beam system is used to “split” the cavity in two so that the 2 halves are electrically isolated (now 2 devices). By designing the microcavity to be leaky in-plane the two devices behave independently and have a phase difference which is dependent on bias. By altering the bias applied to the device the relative phase is changed and beam steering is achieved. The power of these devices will be limited, due to both high heating from the resistive DBR stacks and because VCSELs have a limited area to maintain single mode operation. This work is similar to work on other VCSEL arrays where they have demonstrated to be coherently coupled and to exhibit beam steering where coupling is achieved through anti guided modes [32, 33].

Different Materials

Lasers are at the heart of many applications, including optical data storage[34], optical gyroscopes [35], laser lighting, biomedical applications [36], optical communications [37] and military applications such as laser guiding and gas sensing [38]. Each of these applications require specific wavelengths. Photonic crystal lasers have been shown to operate at a number of key wavelengths, utilising different material systems. Ohnishi *et, al,* demonstrated lasing at 960nm, by utilising GaAs/InGaAs/AlGaAs in 2004 [28], Imada *et, al.,* demonstrated lasing at 1.3µm, utilising InP/InGaAsP in 2002 [39], Matsubara *et, al.,* and demonstrated lasing at 406nm, utilising GaN/AlGaN in 2008 [40] .

All-semiconductor PCSELs were first demonstrated by Williams *et, al.,* in 2012, where a PC consisting of GaAs atoms on an InGaP background were grown using MOCVD regrowth [20,41, 42]. Modelling of these devices showed that they had coupling which was comparable to their void containing counterparts. In this work devices were shown to have a line width of 0.3nm and a half angle divergence of ~3º, while the peak wavelength was shown to be relatively insensitive to temperature, this is because the emission wavelength of a PCSEL is determined by the period of the PC. The band structure was measured and showed strong agreement with the modelled data.

High Power

Skakaguchi *et, al.,* demonstrated a PCSEL array which achieved 35W of power, the array area was 0.4mm^2 and was operated in pulsed mode. The individual devices within the array had an area of 0.02mm^2 and each emitted 800mW of power [43]. In this array the devices were not coherently coupled.

Most recently, high power from a single device as achieved by Hirose *et, al.,*. Watt class power being delivered by a single device [24]. In this work the high power is attributed to two key design aspects of the PCSEL, the use of MOCVD and the atom shape.

Output power of a PSCEL is strongly determined by the in-plane electric field, in particular high power is achieved when the atom shape is not symmetric. Hirose *at, al.,* used right angled isosceles triangles to deliver high power.

1.4 PCSEL Fabrication

I consider 2 types of PCSEL, all-semiconductor [41,42] and void containing [24,27,28]. For an all-semiconductor PCSEL the refractive index variation in the photonic crystal region is obtained by having two different semiconductor materials (i.e. GaAs/AlGaAs, InGaP/GaAs, GaN/AlGaN etc.), while in the void containing PCSEL it is obtained by having semiconductor material and pockets of air. This section describes the methods used to realise PCSELs, first describing the methods of patterning the PC and then considering the growth methods.

Patterning

For both all-semiconductor and void containing PCSELs, the PC needs defining, and this can be achieved in a number of ways. The period of a PC is ~λ/n (where n is refractive index), this means that for a PCSEL operating at 980nm the period will be ~300nm. Patterning is required at a nm scale with 300nm resolution which is too small to use standard photolithography, as the smallest feature size cannot be smaller than the wavelength of exposing light. This section considers the patterning methods used to produce PCs.

Electron beam (e-beam) lithography is the process of irradiating a thin film of resist with a focused beam of electrons. The electrons are emitted by an electron source and focused into a beam using magnetic or electrostatic lenses [44]. The short wavelength of the electron -beam allows ~nm scale patterning. For positive resist, the beam of electrons chemically alter the resist allowing it to be removed, while the unexposed regions remain intact. An etching process is used to etch the hard mask and a separate etching process is then used to remove semiconductor, the hard mask protects the semiconductor underneath, leaving "holes" in the semiconductor where the e-beam has be focused. Figure 1.14 shows the e-beam patterning process used to define a PC region in a PCSEL.

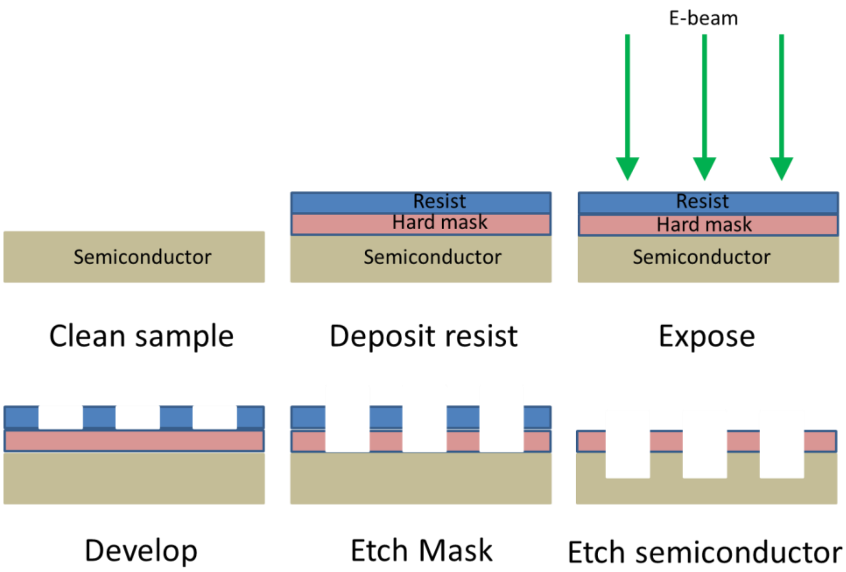

Figure 1.14 schematic of e-beam lithography patterning process

E-beam lithography can produce features of much smaller size than photolithography but the write time is much greater than optical lithography. The e-beam system has a limited field of view, which is determined by the maximum deflection of the lenses. Exposing an area greater than the field of view requires multiple exposures, mis-alignment of the fields may result in stitch errors and pattern overlays. As a consequence, high precision motion control and interferometric measurement systems are required, raising the cost of e-beam systems as compared to optical systems.

Similar to e-beam lithography, laser interference lithography is the process of irradiating a thin film of resist with a laser [45]. Laser interference splits the laser beam into multiple beams, recombining them on the surface of the resist. The recombined beams form an interference pattern, and the dark and light fringes define the PC. The number of recombined beams and the path length difference determines the interference pattern. 3 beams are required to produce a 2D pattern. Figure 1.15 shows the schematic of a LIL system. The major advantages of LIL over e-beam lithography are that it requires significantly less write time and it does not suffer from stitch errors. The patterns which are possible however, are limited by achievable interference patterns.

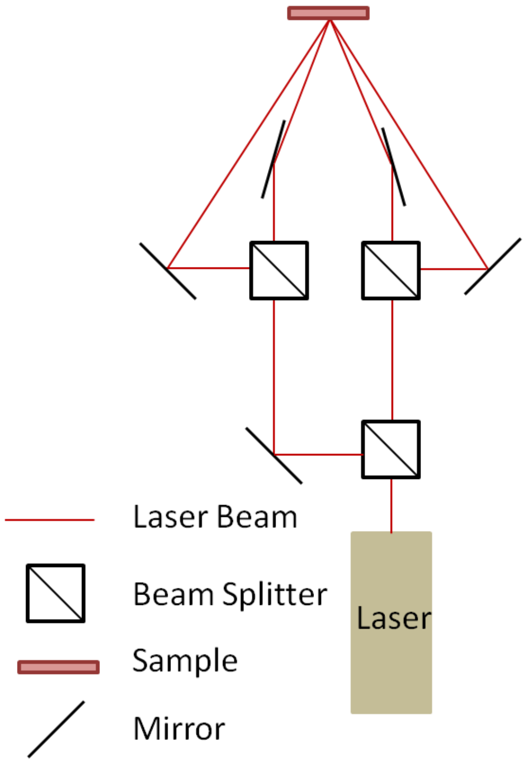

Figure 1.15 Schematic of a laser interference lithography system

Nano-imprint lithography (NIL) is the process of producing nano-scale patterns into resist through mechanical deformation. This process involves producing a patterned template which is forced against the resist, leaving an embossed pattern in the resist [46-48]. Figure 1.16 shows a schematic of the process of nano imprint lithography.

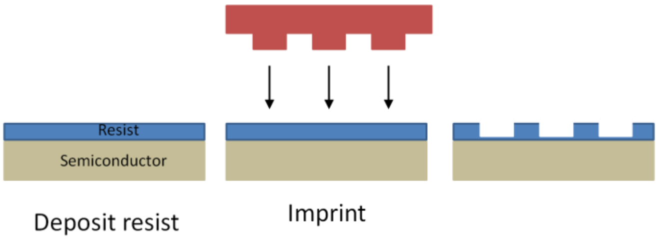

Figure 1.16 schematic of nano imprint lithography process

NIL allows very small and detailed structures to be produced rapidly and repeatedly, however each design requires the design and manufacture of a unique stamp which cannot be used for other structures. Once the photonic crystal region has been defined and etched the rest of the structure needs to be realised. This section describes the three main methods for PCSEL growth.

Wafer Fusion

Wafer fusion is the most widely used method of manufacturing PCSELs. Wafer fusion is the process of creating a complete structure from 2 wafers. The 2 wafers are compressed under high pressure, in a vacuum and heated until they fuse. To create a PCSEL one of the wafers needs to have a PC etched into the surface prior to fusion. Figure 1.17 shows a schematic representation of wafer fusion of two wafers a and b where wafer b has a PC etched into the top surface.

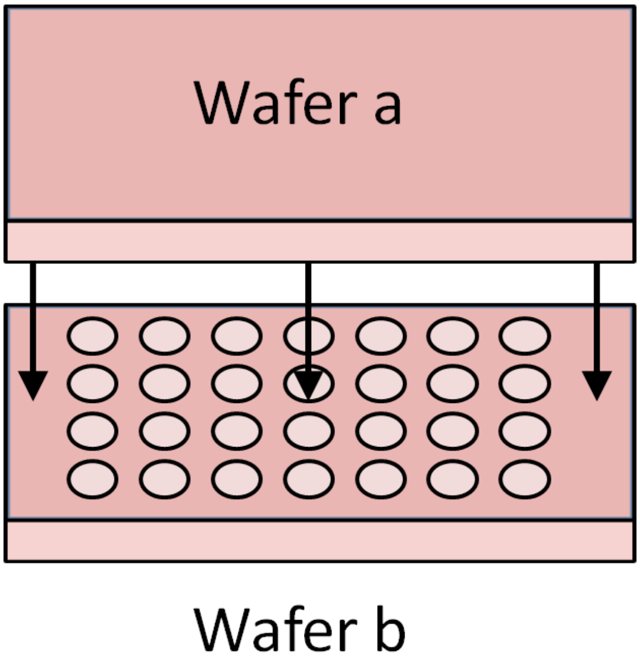

Figure 1.17 schematic of wafer fusion

MOVPE Re-Growth

Metal organic vapour phase epitaxy (MOVPE) is a deposition method used in epitaxial growth of semiconductors. In MOVPE, pure gases (metalorganics and hydrides) are passed over the surface of a heated semiconductor material. The decomposition of these gases causes atoms to bond to the substrate surface growing new layers. Figure 1.18 shows an illustration of the MOVPE process used to deposit epitaxial layers.

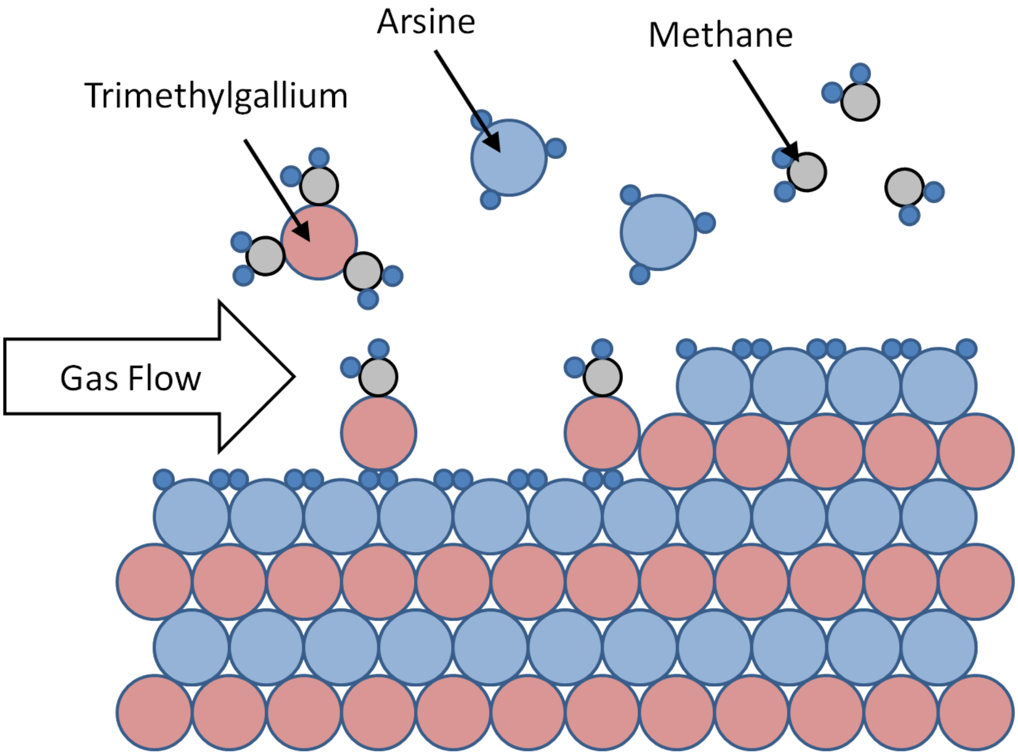

Figure 1.18 illustration of MOCVD process

MOVPE can be used to grow both all-semiconductor [41,42] and void containing PCSELs [24, 49]. In both cases a wafer is grown, PC features are etched into the top surface of the wafer, the wafer is placed back into the reactor and the remaining structure is grown. The second growth is known as the re-growth step. The growth of void containing PCSELs can be achieved through re-growth by depositing a thin layer of SiO_2 at the bottom of the holes to prevent growth and leave intact voids within the structure [49] or by adjusting the growth conditions so that a void remains within the structure. It is by MOVPE re-growth that the first all-semiconductor PCSELs were realised [41,42] and the current record for high power was achieved [24].

MBE Re-Growth

Molecular beam epitaxy (MBE) is a process of semiconductor growth, but unlike MOVPE, the sample is kept in an ultra pure vacuum (10^{-8} Pa). Elements such as Ga, In, As etc. are kept at ultra high purity in solid form in cells positioned around the sample. The cells are heated until the solid elements sublime and effuse, forming a beam of atoms which is then directed towards the sample and deposited upon it [50], deposition is controlled by shutter which when open allow material to be deposited. Figure 1.19 shows a schematic of an MBE system.

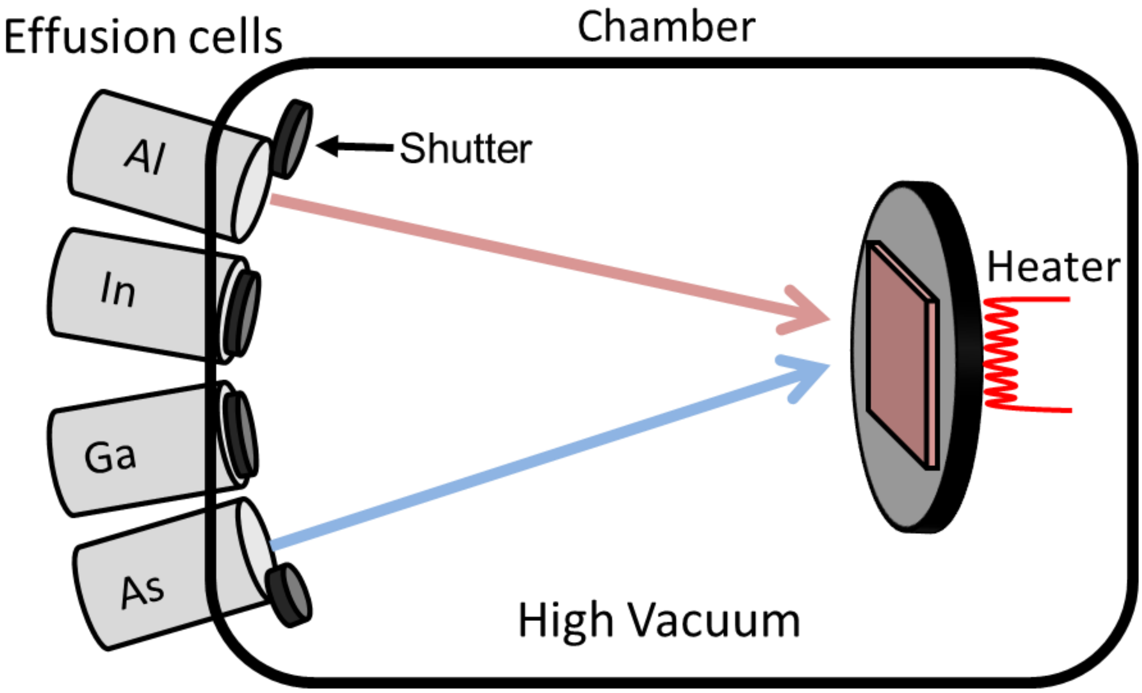

Figure 1.19 Schematic of an MBE system (adapted from an image provided by Professor Ozaki)

MBE has been be used to grow void containing PCSELs [51] but to date there have been no studies showing MBE regrowth of all-semiconductor PCSELs.

PC holes are etched into the top surface of the wafer, the wafer is placed back into the reactor and the remaining structure is grown. The growth of void containing PCSELs can be achieved through re-growth by depositing a thin layer of SiO_2 at the bottom of the holes to prevent growth and leave intact voids within the structure.

1.5 All-Semiconductor PCSELs

Williams *et, al.*, in 2012 [20,41,42], demonstrated an all-semiconductor PCSEL for the first time. Figure 1.20 shows the LI characteristics and spectra of a device operating at 100mA and 250 mA, operating under pulsed condition at room temperature.

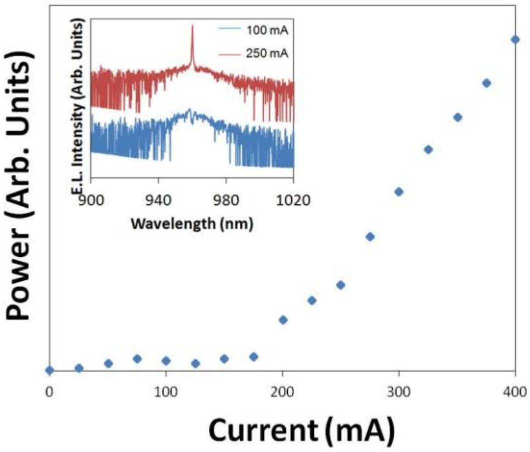

Figure 1.20 LI of an all-semiconductor PCSEL operated under pulsed conditions at room temperature inset shows the spectra at 100mA and at 250mA [41]

These devices were shown to have a low divergence ~3^o and a line width of 0.3nm. The devices were analysed over a range of temperatures and found to have a very small change in emission wavelength with temperature. Figure 1.21 shows emission wavelength of PCSELs with different periods over a range of temperatures. The peak wavelength of the PCSEL is not strongly dependent on temperature.

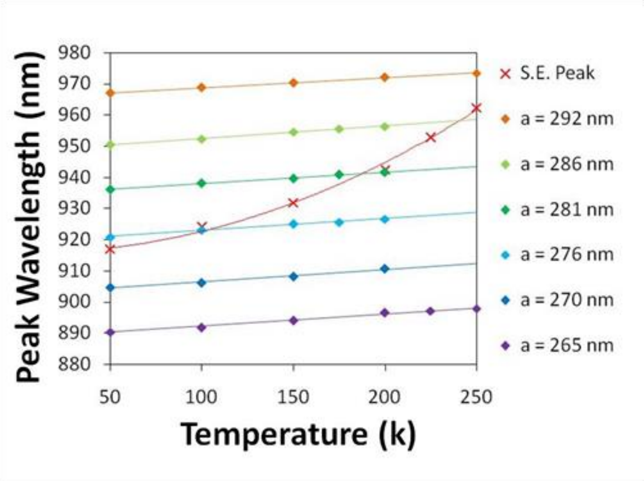

Figure 1.21 Peak wavelength of PCSELs with a period varying from 265nm to 292nm over a temperature range from 50K to 250K [40]

Waveguide modelling demonstrated that the all-semiconductor PCSEL exhibited higher mode overlap with the PC than the same structure where the PC region consisted of semiconductor and air. Figure 1.22 shows the modelled mode profile of a PCSEL where the PC consists of either InGaP/GaAs or InGaP/air, the location of the PC and the QW are shown.

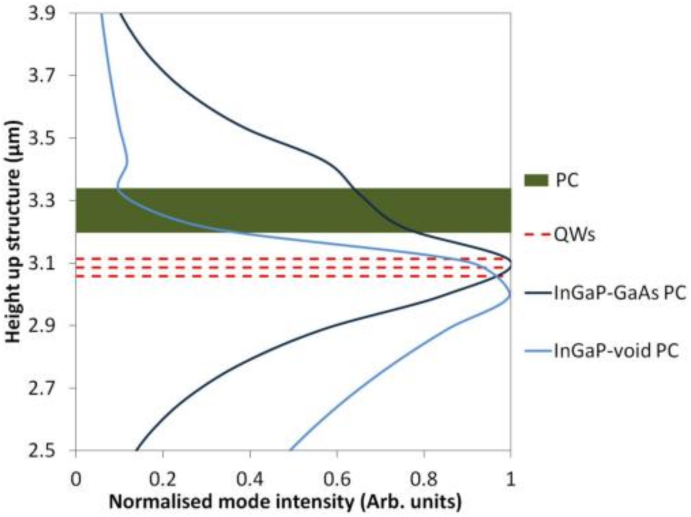

Figure 1.22 shows the mode profile of a PCSEL from Williams *et*, *al.*, [41] showing the location of PC layer and QW layers

1.6 Gaps in the Knowledge

Williams *et al.*, demonstrated the first all-semiconductor PCSEL based on eptaxial regrowth. The devices were operated under pulsed current injection at room temperature, however room temperature continuous wave operation was not achieved and devices had a relatively high threshold current density (~10kAcm^2). A push towards CW operation through reduced J_{th}, and high powers is therefore required.

These devices were modelled as a 1D waveguide using FIMMWAVE, and were able to show that mode overlap and coupling were higher in a waveguide which incorporated all-semiconductor PC rather than a void containing PC. However, a thorough study of the waveguide design for all-semiconductor and void containing PCSELs has not been reported. Additionally there has not been an extensive study to consider if a void containing structure can be engineered to realise greater coupling than all-semiconductor devices.

There has been significant effort to design the optimal atom shape and lattice geometry of PCSELs, this work being focused on void containing structures. Williams *et*, *al.*, did experimentally verify modelled band structure of an all-semiconductor PCSEL. However, a complete investigation into the effect of atom size and shape has to date not been conducted (excluding published work by Taylor *et, al.*, [52,53] which is the focus of this thesis).

High power has been demonstrated from both PCSEL arrays and individual PCSEL devices. However, coherent PCSEL arrays have not been shown, nor has anyone demonstrated that the coherence between the devices can be controlled. Power scaling with area provides significant problems to be overcome for laser arrays. For example in electrically pumped vertical cavity lasers (EP-VCSELs) the power has been shown to scale with diameter and not area due to current spreading and heat extraction issues [54, 55]. To date there has not been a demonstration of a PCSEL array where adjacent devices are thermally isolated, and contribute to increase the output power of neighbouring, coupled PCSELs

1.7 Thesis Outline

This thesis considers development in all-semiconductor PCSELs [20,41,42,52, 53], initially exploration of the waveguide design is considered, and then design of the PC is considered, progress in device performance is demonstrated and finally an array of all-semiconductor PCSELs is shown to give power scaling and electronic control of coherence.

Chapter 2 models the band structure of all-semiconductor PCSELs which have a PC consisting of circular atoms on a square lattice. Modelling results show how the band structure changes as atom radius increases from 0.01-0.45a (where a is the period of the PC) and show the nature of the bands considered. The location of the degenerate bands is shown to change as the radius increases, simultaneously the nature (leaky/non-leaky) of the bands around the gamma point are shown to change. The ability to tune the relative strengths of in-plane and out-of-plane coupling through the choice of atomic radius is demonstrated. Two regions of interest r~0.2a and r~0.4a are highlighted, and the influence of the mode nature and band structure on the choice of lasing band is described

Chapter 3 initially explores waveguide design of GaAs based PCSELs. The structure from Williams *et, al.,* is modelled for all-semiconductor and void containing PCSELs. The all-semiconductor PCSEL is shown to give a higher mode overlap with the PC region. Next, structural modifications to the waveguide are considered in an attempt to increase the mode overlap and coupling of the void containing structure. Finally, PCSEL structures of different material systems and at different wavelengths are considered. All-semiconductor and void containing PC regions are modelled to determine PC coupling coefficients. In all cases the structures are modelled as a 1D waveguide, where the PC region is considered as a refractive index given by a weighted average of the refractive index of its constituent parts, using FIMMWAVE [56]. It is shown that the coupling coefficients may be enhanced in void containing PCSEL by structural modifications of the waveguide and the importance of additional care in the design of void containing PCSEL waveguides is highlighted. An analysis of different material systems (GaN, InP) shows that all-semiconductor PCSELs have higher coupling than void containing structures in all cases investigated.

Chapter 4 describes progress in all-semiconductor PCSEL performance. Initially, growth and fabrication of all-semiconductor PCSELs is described, then continuous wave (CW) room temperature (RT) operation is demonstrated. Devices are shown to have narrow line width (0.5nm), lower divergence (1°) and a lower threshold current density ($800A/cm^2$) than previous devices, the low J_{th} allows CW room temperature operation. A coherent PCSEL array is then demonstrated for the first time, where independent PCSELs are separated by a relatively large distance (1mm), so they are electrically, optically and thermally isolated. The electronic control of coherence and power scaling is demonstrated, offering a route to high power PCSEL arrays and beam steering.

Chapter 5 briefly summarises this thesis and highlights areas of future work for this topic.

References

[1] J. D. Joannopoulos, P. Villeneuve, and S. Fan,

“Photonic crystals: putting a new twist on light”

Nature, **386**,143–149, 1997

[2] K. Sakai, E. Miyai and S. Noda,

“Coupled wave model for square-lattice two-dimensional photonic crystal with transverse-electric-like mode”

Applied physics letters, **89**, 021101, 2006

[3] K. Sakai, E. Miyai and S. Noda,

“Two-dimensional coupled wave theory for square-lattice photonic-crystal lasers with TM-polarisation”

Optics express, **15,** 7, 3981, 2007

[4] J. Joannopoulos, S. Johnson,

“Photonic crystals: modelling the flow of light”

second edition, Princeton university press,chapter 2, 2008

[5] http://ab-initio.mit.edu/wiki/index.php/MIT_Photonic_Bands

[6] S. Shi, C.Chen and D. Prather,

"Plane-wave expansion method for calculating bans structure of photonic crystal slabs with perfectly matched layers"

Journal of the optical society of America, 21, 9, 1769-1775, 2004

[7] M. Imada, A. Chutinan, S. Noda and M. Mochizuki,

"Multidirectionally distributed feedback photonic crystal lasers"

Physical review B, **65**, 195306, 2002

[8] J. Joannopoulos and S. Johnson,

"Photonic crystals: modelling the flow of light"

second edition, Princeton university press, chapter 5, page 83, 2008

[9] T. Lund-Hansen, S. Stobbe, B. Julsgaard, H. Thyrrestrup, T. Sünner, M. Kamp, A. Forchel, and P. Lodahlv,

"Experimental Realization of Highly Efficient Broadband Coupling of Single Quantum Dots to a Photonic Crystal Waveguide"

Physics Review Letters, **101**, 113903, 2008

[10] M. Tokushima, H. Kosaka, A. Tomita and H. Yamada

"Light wave propagation through a 120^{o} sharply bent single line-defect photonic crystal waveguide"

Appied physics letters, **76**, 952, 2000

[11] A. Mekis, J. C. Chen, I. Kurland, S. Fan, P Villeneuve, and J. Joannopoulos,

“high transmission through sharp bends in photonic crystal waveguides”

Physics review letters, **77**, 3787, 1996

[12] B. Ellis, M. Mayer, G. Shambat, T. Sarmiento, J. Harris, E. Haller & J Vučković,

“Ultralow-threshold electrically pumped quantum-dot photonic-crystal nanocavity laser”

Nature Photonics, **5**, 297–300, 2011

[13] M. Lončar, T. Yoshie, A. Scherer, P. Gogna andY. Qiu

“Low-threshold photonic crystal laser”

Applied physics letters, **81**, 2680, 2002

[14] O. Painter, R. Lee, A. Scherer, A. Yariv, J. O'Brien,P. D. Dapkus, I. Kim,

“Two-Dimensional Photonic Band-Gap Defect Mode Laser”

Science, 284, 5421, 1819-1821, 1999

[15] Y. Akahane, T. Asano, B. Song & S. Noda,

“High-*Q* photonic nanocavity in a two-dimensional photonic crystal”

Nature, **425**, 944-947, 2003

[16] K. Sakai, E. Miyai, T. Sakaguchi, D. Ohnishi, T. Okano and S. Noda.

“Lasing band edge identi_cation for a surface-emitting photonic crystal laser”

IEEE Journal of Selected Areas of Communication., **23**, No. 7, 1335, 2005

[17] M. Plihal and A. A. Maradudin.

“Photonic band structure of two-dimensional systems: The triangular lattice”

Physics Review B, **44**, No. 16, 8565, 1991

[18] J. B. Nielsen, T. Sondergaard, S. E. Barkou, A. Bjarklev, J. Broeng and M. B. Nielsen.

“two-dimensional Kagome structure, fundamental hexagonal photonic crystal configuration”

Electronics Letters, **35**, No. 20, 1736, 1999

[19] Y. Kurosaka, K. Sakai, E. Miyai, S. Noda,

“Controlling vertical optical confinement in two-dimensional surface-emitting photonic-crystal lasers by shape of air holes”

Optics express, 16, 22, 1848-18494, October 2008

[20] D. Williams, K. Groom, D. Childs, R. Taylor, S. Khamas, R. Hogg, B. Stevens, N. Ikeda, Y. Sugimoto

“Optimisation of coupling between photonic crystal and active elements in an epitaxially regrown GaAs based photonic crystal surface emitting laser”

Japanese journal of applied physics, 51, 02BG05-1-3, 2012

[21] S. Noda, M. Yokoyama, A. Chutinan, M. Imada, M. Mochizuki, “Polarization Mode Control of Two-Dimensional Photonic Crystal Laser by Unit Cell Structure Design”

Science, **293**, 1123, 2001

[22] M. Yokoyama, S. Noda,

“Polarisation mode control of two-dimensional photomic crystal laser having a square lattice structure”

IEEE journal of quantum electronics,**39**, 9, 1074,2003

[23] Y.Kurosaka, S. Iwahashi, K. Sakai, E. Miyai, W. Kunishi, D.Ohnishi and S. Noda

“Band structure observation of of 2D pgotonic crystal with various v shaped air hole arangements”

IEICE Electronics express, **6**, 13, 966, 2009

[24] K. Hirose, Y. Liang, Y. Kurosaka, A. Watanabe, T. Sugiyama & S. Noda,

“Watt-class high-power, high-beam-quality photonic-crystal lasers”

Nature Photonics, **8**, 406-411, 2014

[25] E.Miyai, K. Sakai, T. Okano, W. Kunishi, D. Ohnishi, S.Noda

“Lasers producing tailored beams”

Nature, **441**, 946, 2006

[26] M. Berggren, A. Dodabalapur, R.E. Slusher, Z. Bao, A. Timko and 0. Nalamasu, “Organic lasers based on lithographically defined photonic-bandgap resonators”

Electronics Letters, **34,** 1, 1998

[27] M. Imada, S. Noda, A. Chutinan, T. Tokuda, M. Murata and G. Sasaki.

“Coherent two-dimensional lasing action in surface-emitting laser with triangular-lattice photonic crystal structure”

Applied Physics Letters, **75**, 3, 316, 1999

[28] D. Ohnishi, T. Okano, M. Imada and S. Noda,

“Room temperature continuous wave operation of a surface emitting two dimensional photonic crystal laser”

Optics Express, **12**, No. 8, 1562, 2004

[29] Y. Sato, Y. Tanaka, J. Upham, Y. Takahashi and T. Asano,

”Strong coupling between distant photonic nanocavities and its dynamic control”

Nature photonics, 6, 1, 56, 2012

[30] Y. Kurosaka, S. Iwahashi, Y. Liang, K. Sakai, E. Miyai, W. Kunishi, D. Ohnishi & S. Noda,

“On-chip beam-steering photonic-crystal lasers”

Nature Photonics, **4**, 447 – 450, 2010

[31] M. T. Johnson, D. F. Siriani, M. P. Tan, and K. D. Choquette, "Relative phase tuning of coupled defects in photonic crystal vertical-cavity surface-emitting lasers"

Journal of Selected Topics in Quantum Electronics, **19**, 1701006, 2013.

[32] D. Siriani and K. Choquette,

"Implant defined anti-guided vertical cavity surface emitting laser arrays"

IEEE journal of quantum electronics, **47**, 2, 2011

[33] D. Serkland, K. Choquette, G. Hardley, K. Geib and A. Allerman,

"Two element array of anti-guided vertical cavity lasers"

Applied physics letters, **75**, 3754, 1999

[34] Y. Mitsuhashi,

"Optical storage: science and technology"

Japanese Journal of Applied Physics, **37**, 2079-2083, 1997

[35] A. Pavlath,

"Fiber-optic gyroscopes"

IEEE Lasers and Electro-Optics Society Annual Meeting Conference Proceedings, Volume 2, 237–238, 1994

[36] M. E. Brezinski,

"Optical Coherence Tomography: Principles and Applications"

Amsterdam, The Netherlands/Boston, MA: Academic Press, 2006

[37] F. Mitschke,

Fiber Optics - Physics and Technology, chapter 6, Springer, 2009

[38] P. Werlea, F. Slemra, K. Maurera, R. Kormannb, R. Mucke and B. Janker,

"Near- and mid-infrared laser-optical sensors for gas analysis"

optics and lasers in engineering, **37**, 101-114, 2001

[39] M. Imada, A. Chutinan, S. Noda and M. Mochizuki,

"Multidirectionally distributed feedback photonic crystal lasers"

Physics Review B, **65**, 19, 195306-1, 2002

[40] H. Matsubara, S. Yoshimoto, H. Saito, Y. Jianglin, Y. Tanaka and S. Noda,

"GaN photonic-crystal surface-emitting laser at blue-violet wavelengths"

Science, **319**, 445, 2008

[41] D. M. Williams

"All-semiconductor photonic crystal surface emitting lasers at 980 nm through epitaxial regrowth"

PhD thesis, University of Sheffield, 58, 2014

[42] D. Williams, K. Groom, D. Childs, R. Taylor, S. Khamas, R. Hogg, B. Stevens, N. Ikeda, Y. Sugimoto

“Epitaxially regrown GaAs-based photonic crystal surface emitting laser”

IEEE photonics technology letters, **24**, 11, 966-968, June 2012

[43] T. Sakaguchi1, W. Kunishi1, S. Arimura, K. Nagase, E. Miyai, D. Ohnishi, K. Sakai and S. Noda,

“Surface-Emitting Photonic-Crystal Laser with 35W Peak Power”

Conference on Lasers and Electro-Optics (CLEO) and the International Quantum Electronics Conference (IQEC), 2009

[44] M. McCord, M. J. Rooks

“SPIE Handbook of Microlithography”

Micromachining and Microfabrication, 2000

[45] L. Prodan, T. Euser, H. A. van Wolferen, C. Bostan, R. de Ridder, R. Beigang, K. Boller and L. Kuipers,

“Large-area two-dimensional silicon photonic crystals for infrared light fabricated with laser interference lithography”

Nanotechnology, **15**, 639, 2004

[46] S. Chou, P. Krauss, P. Renstrom, "Imprint Lithography with 25-Nanometer Resolution"

Science **272,** 5258, 1996

[47] V. Reboud, N. Kehagias, C. Sotomayor Torres, M. Zelsmann, M. Striccoli, M. Curri, A. Agostiano, M. Tamborra, M. Fink, F. Reuther and G. Gruetzner,

"Spontaneous emission control of colloidal nanocrystals using nanoim-printed photonic crystals"

Applied Physics Letters., **90**,011115, 2007

[48] E. Arakcheeva, E. Tanklevskaya, S. Nesterov, M. Maksimov, S. Gurevich, J. Seekamp and C. Sotomayor Torres,

"Fabrication of semiconductor and polymer based photonic crystals using nanoimprint lithography"

Technical Physics, **50,** 8, 1043, 2005

[49] H. Matsubara, S. Yoshimoto, H. Saito, Y. Jianglin, Y. Tanaka and S.Noda.

"GaN photonic-crystal surface-emitting laser at blue-violet wavelengths"

Science, **319**, 445, 2008

[50] B. Streetman, S. Banerjee

"solid state electronic devices"

sixth edition, chapter 2, page 23, prentice hall, 2000

[51] M. Nishimoto, K. Ishizaki, K. Maekawa, K. Kitamura and S. Noda

”Air-Hole Retained Growth by Molecular Beam Epitaxy for Fabricating GaAs-Based Photonic-Crystal Lasers”

Applied physics express, **6**, 4, 2013

[52] R. Taylor, D. Williams, D. Childs, B. Stevens, L. Shepherd, S. Khamas, K. Groom, R. Hogg, N. Ikeda, and Y. Sugimoto

”Photonic crystal surface emitting lasers based on epitaxial regrowth”

IEEE Journal of Selected Topics in Quantum Electronics, **19**, 4, 4900407, 2013

[53] R. Taylor, D. Williams, J. Orchard, D. Childs, S. Khamas and R. Hogg

“Band structure and waveguide modelling of epitaxially regrown photonic crystal surface emitting lasers”

Journal of Physics D, **46**, 26, 264005(8pp), 2013

[54] J. Orchard, D. Childs, L. Lin, B. Stevens, D. Williams, R. Hogg

“Design rules and characterisation of electrically pumped vertical exter-nal cavity surface emitting lasers”

Japanese Journal of Applied Physics, **50**, 04DG0S, 2011

[55] J. Orchard, D. Childs, L. Lin, B. Stevens, D. Williams, R. Hogg

“Trade-offs in the realisation of electrically pumped vertical external cavity surface emitting lasers J. Selected Topics in Quantum Electronics”

17, No. 6, 1745, 2011

[56] http://www.photond.com/products/fimmwave.htm

2. Band Structure Modelling

In this chapter the photonic band structure is modelled for GaAs based photonic crystals. This band structure is used to calculate in-plane (K_3) and out-of-plane coupling (K_1) for a PCSEL and the nature of the mode is considered by modelling the in-plane magnetic field of the band.

There are many ways to model the band structure of a PC i.e. plane wave expansion method (PWE) [1], finite difference time domain (FDTD) [2] and coupled wave theory (CWT) [3]. Here, band diagrams are modelled using MIT photonic bands (MPB) [4]. MPB is free Linux based software which computes the definite frequency eigenstates of Maxwell's equations for arbitrary wave vectors using a fully vectoral plane wave expansion method (PWE).

This chapter examines the effect of increasing the atom radius of a PCSEL where the PC layer consists of circular atoms on a square lattice. It will be shown in the next chapter that void containing PCSELs suffer from limitations in the size of void atom which may be used due to issues in waveguide design. As a consequence, a thorough analysis of a variation of this parameter on the various coupling coefficients has not been made. Similarly, due to difficulties in fabrication, inverting the index contrast of the PC has not been discussed. Initially the effect on the band structure is explored for a range of atom radius from 0.01a to 0.4a, for type I and type II PCs. The band structure is used to calculate the in-plane and out-of-plane coupling and atom radius effect on coupling is considered. Finally, a change in the character of the in-plane magnetic field is shown as atom radius increases and the effect on PCSEL design is discussed.

Definitions

Figure 3.1 shows a top view schematic of a photonic crystal where, key parameters are defined. In this chapter, as in Taylor *et al.*,[5]: the base material B shall be referred to as the background material, material A shall be referred to as the atom, a is the PC period and is consistent across the whole PC, r is the atom radius and is constant for each atom. The atom radius is expressed as a fraction of the period. Type I and type II PCSELs are defined as type I low refractive index material A and high refractive index material B, type II low refractive index material A and high refractive index material B. The model considers the PC to be infinitely thick. This assumption is reasonable as long as the mode profile does not vary across the thickness of the PC layer which we find to be a good approximation for all-semiconductor PCSELs. Referring to the materials within a PC shall take the form material A/material B i.e. GaAs/InGaP. A PC where the refractive index contrast is obtained through using semiconductor and air shall be referred to as the void containing while one where the refractive index contrast is obtained through different semiconductor materials shall be refered to as “all-semiconductor”.

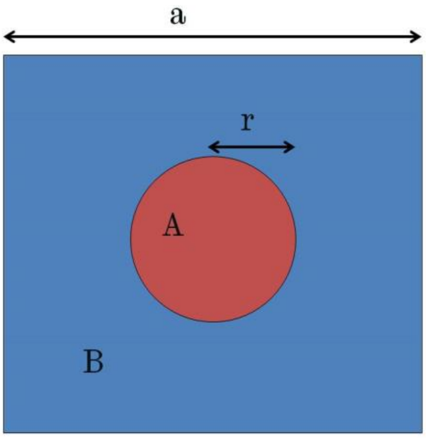

Figure 2.1 schematic of a photonic crystal, indicating nomenclature used for atom and background material (A and B respectively), atom radius (r) and unit cell size (a)

2.1 Theory

In a vacuum, the relationship between frequency and wave vector is defined as $\omega = ck$ (where ω is frequency, c is the speed of light in a vacuum and k is wave number) when propagating in any other material (with a constant refractive index) this becomes $\omega = \frac{ck}{n}$ (where n is refractive index) and is constant for all directions.

The band structure of a photonic crystal can be calculated using Maxwells equations

$$\boldsymbol{\nabla} \cdot \mathbf{H}\,(\mathrm{r,t}) = 0 \tag{1}$$

$$\boldsymbol{\nabla} \cdot (\varepsilon(\boldsymbol{r})\mathbf{E}\,(\mathrm{r,t})) = 0 \tag{2}$$

$$\boldsymbol{\nabla} \times \mathbf{E}\,(\mathrm{r,t}) + \mu_0 \frac{\partial \mathbf{H}\,(\mathrm{r,t})}{\partial t} = 0 \tag{3}$$

$$\boldsymbol{\nabla} \times \mathbf{H}\,(\mathrm{r,t}) - \varepsilon_0 \varepsilon_{(r)} \frac{\partial \mathbf{E}\,(\mathrm{r,t})}{\partial t} = 0 \tag{4}$$

Where **H**(r,t) is magnetic field strength, **E**(r,t) is electric field, ε_0 is the permittivity of free space (8.85×10^{-12} F/m), ε_r is relative permittivity and μ_0 is the permeability of free space ($4\pi\mathrm{x}10^{-7}$ Henry/m). It is assumed that: ε_r is real, positive and any frequency dependence is ignored, the structure does not change over time and there are no charges within the structure.

By considering a field that varies sinusoidally with time

$$\mathbf{E}\,(\mathrm{r,t}) = \mathbf{E}\,(\mathrm{r})\, e^{-i\omega t} \tag{5}$$

$$\mathbf{H}\,(\mathrm{r,t}) = \mathbf{H}\,(\mathrm{r})\, e^{-i\omega t} \tag{6}$$

Which gives

$$\boldsymbol{\nabla} \times \mathbf{E}\,(\mathrm{r,t}) - i\omega\mu_0\mathbf{H}(\mathrm{r}) = 0 \tag{7}$$

$$\boldsymbol{\nabla} \times \mathbf{H}\,(\mathrm{r,t}) + i\omega\varepsilon_0\varepsilon_r\mathbf{E}(\mathrm{r}) = 0 \tag{8}$$

By using (7) & (8) it is possible to calculate the modes within a structure, firstly divide (8) by ε_r, take the curl and substitute (7)

$$\boldsymbol{\nabla} \times \left(\frac{1}{\varepsilon_\mathrm{r}}\, \boldsymbol{\nabla} \times \mathbf{H}\,(\mathrm{r})\right) = \frac{\omega^2}{c^2}\,\mathbf{H}\,(\mathrm{r}) \tag{9}$$

Using this equation we can find **H**(r) and substitute it into (8) to find **E**(r). The solutions to (9) give the TM bands and substituting this into (8) gives the TE bands [6].

Consider a structure shown in figure 2.2 where a photonic crystal with circular pillars arranged in square lattice is shown. If we consider the two wave vectors α and γ it is clear that the spatial variation in refractive index is different for each wave. Due to symmetry there are equivalent directions within the structure; these directions will have the same allowed and forbidden states, so not all directions need to be calculated.

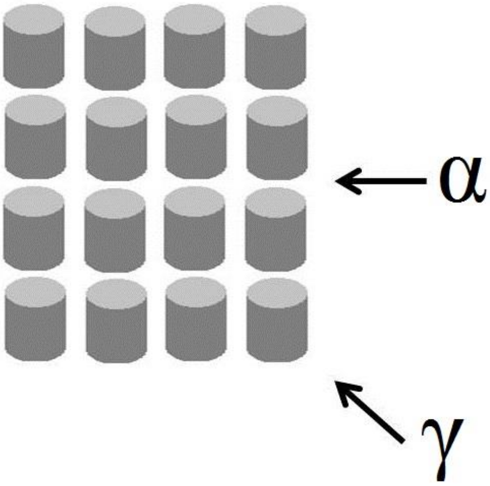

Figure 2.2 photonic crystal of cylinders in square lattice showing two different wave-vectors α and γ

Considering band structure in this manner is analogous to considering band structure in solid state physics [7] , where Bloch theory demonstrates that any wave vector in reciprocal space can be represented within the first Brillouin zone [8]. For the case above (Figure 2.2) the reciprocal lattice is shown in figure 2.3, the first and second Brillouin zones are indicated. In this Brillouin zone there are three highly symmetric directions Γ, X and M which are the boundary of the irreducible zone, any points outside the first Brillouin can be translated onto it.

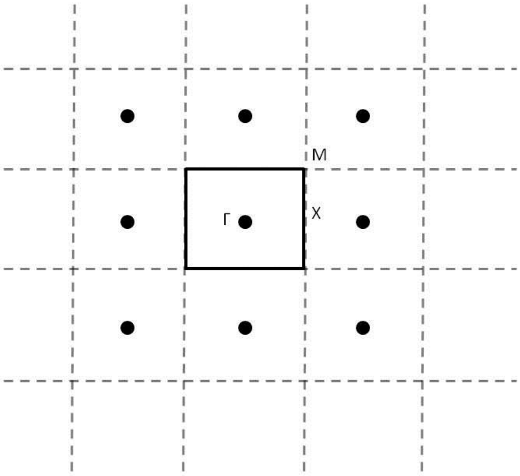

Figure 2.3 reciprocal lattice for a 2D square lattice showing first brilliouin zone (solid black square) and the most important symmetry points Γ, X and M

As discussed previously, light scattered at index contrast interfaces causes interactions which may lead to forbidden energies and band bending, this is seen on the band diagram as a band gap.

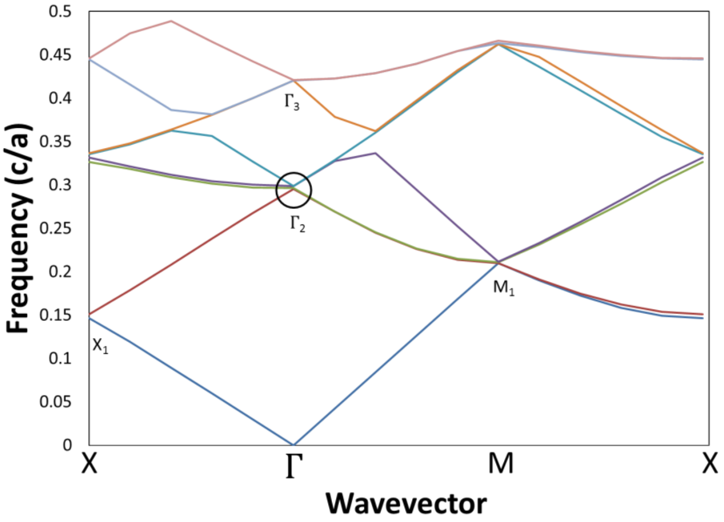

Figure 2.4 modelled band structure for a type I InGaP/GaAs PC with a circular atom in a square lattice where the radius r=0.4a

Figure 2.4 shows the complete band structure of a PC where the atom is an infinitely thick cylinder, of InGaP on background of GaAs, arranged on a square lattice, the atom radius is 0.4a. Wave vectors corresponding to symmetry points Γ, X and M are indicated and specific points of interest (X_1, Γ_2, M_1 and Γ_3) are highlighted. As discussed in Chapter 1, there are fundamentally 2 types of PC laser: a micro-cavity [9-12] and a band edge laser [13-18]. This work focuses on band edge lasers (where lasing occurs from a band edge) because the lasers considered here are designed to emit normal to the surface, we are interested in only the band edge at the Γ_2-point. Circled in figure 2.4 is the Γ- point lasing band edge that this chapter is most concerned with. It is at this band edge in which a local band gap appears, which increases as refractive index contrast increases. It is expected that lasing may occur from different band edges of the band diagram. Each of these points exhibits different wave coupling. Point X_1 corresponds to coupling of waves in forward and backward directions only, this coupling is the coupling exploited in a DFB and in a square lattice there are two directions in which this can occurs. Point M_1 corresponds to coupling of waves in 4 in-plane directions. Point Γ_2 is the point where waves propagating in 4 directions are coupled, in addition light is coupled and emitted perpendicular to the PC. Other regions exist where vertical emission occurs, for example the Γ_3-point. This region has components that scatter at angles between 0^o and 90^o as well as the purely vertical direction [3].

Band Edge Identification

Sakai *et, al.,* identified and measured the lasing band edge of a PCSEL in 2008, showing that it was consistent with modelling [19]. This was achieved by applying current to the device and measuring the angular dependence of emission spectra. The band structure can then be plotted as frequency against wave vector. The wave vector k is related to the emission angle θ by the equation $k = \frac{2\pi}{\lambda}\sin\theta$, where λ is free space wavelength. Figure 2.5 shows the schematic of the setup used.

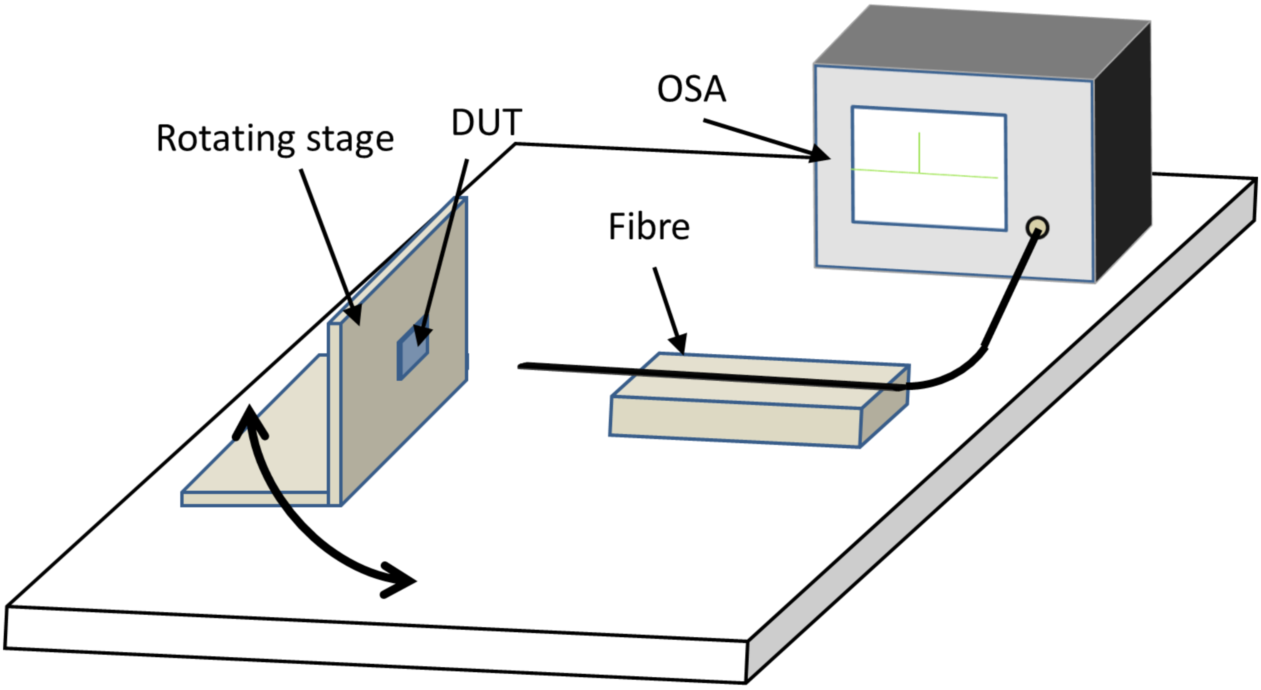

Figure 2.5 schematic of experimental setup used to measure band structure

Williams *et, al.*, and Taylor *et, al.*, used the same method to identify the lasing band edge of all-semiconductor lasers in 2012 and 2013, respectively [14-16, 20]. Figure 2.6 shows the measured band structure of an all-semiconductor PCSEL, the red line shows modelled band structure overlaid on the measured results. The result shows a good agreement between experimental and modelled data. The lasing is shown to occur at the split off band which is a leaky band (as will be shown later).

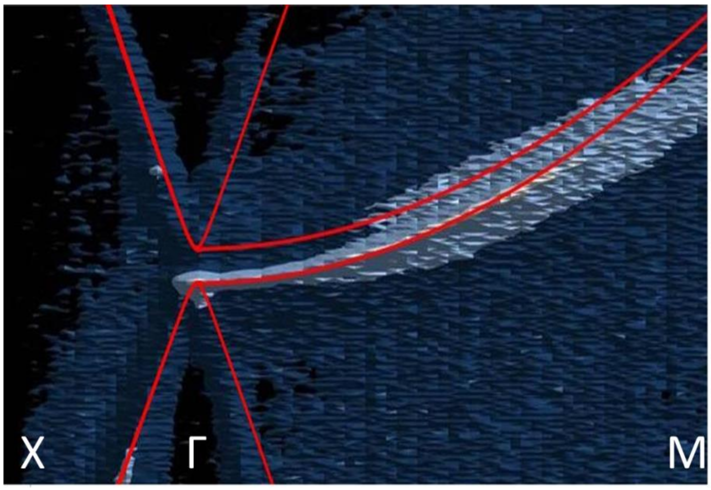

Figure 2.6 measure band structure of all-semiconductor PCSEL with modelled band structure overlaid (red line) from Taylor *et, al.*,

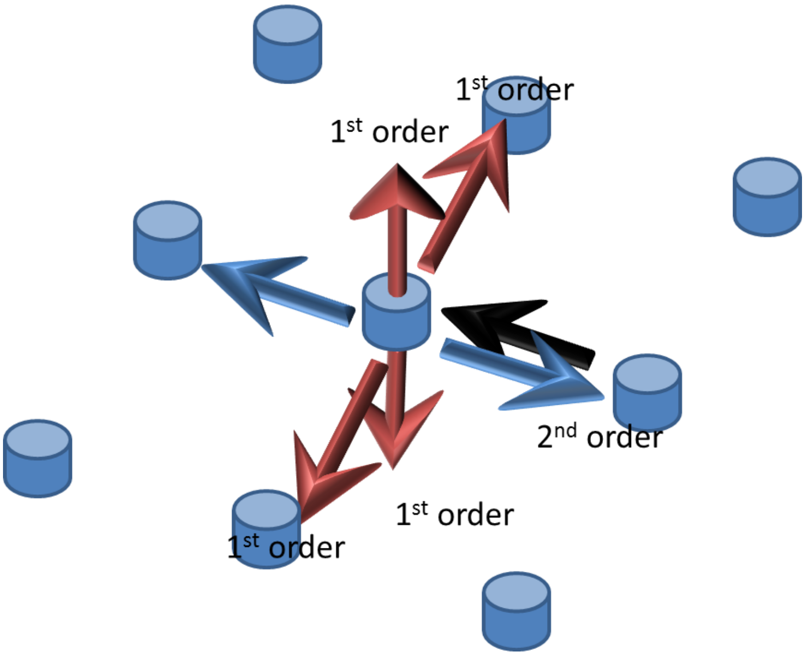

Figure 2.7 schematic of propagating directions of coupled waves of a square lattice PC initial wave direction is shown as a black arrow while first order scattering shown with red arrows and second order shown with blue arrows

Figure 2.7 shows a schematic of the possible scattering directions for an incident wave (black arrow) with second order scattering shown as blue arrows and first order scattering shown as a red arrow. It is worth noting that out-of-plane scattering occurs equally in both directions. From this point only the region close to the Γ_2-point will be considered, further modelling will show a region very close the Γ_2-point and the Γ_2-point will simply be referred to as the Γ-point.

Figure 2.8 shows the modelled band structure of a type PC with circular atoms on a square lattice, where the atom radius is 0.4a. It is plotted in the region of Γ_2.

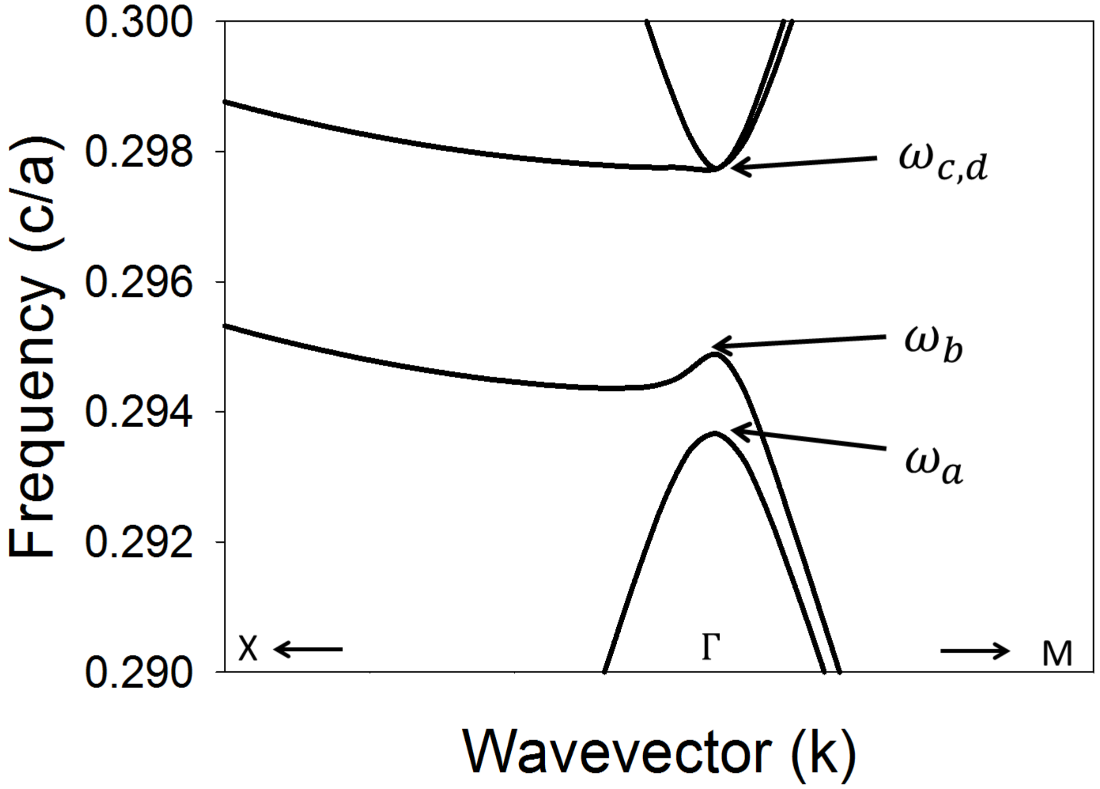

Figure 2.8 modelled band structure of a type II GaAs/InGaP PC with a circular atom on a square lattice

Equations (10), (11) and (12) are from Sakai e*t, al.,* showing the relationship between coupling and the band structure of a PC. Where c is the speed of light in a vacuum, n_{ave} is the average refractive index of the PC layer, β_0 is $2\pi/a$, K_1 is out-of-plane coupling and K_3 is in-plane coupling. The coupling coefficient is a measure of the strength of scattering and is the amount of feedback per unit length for in-plane K_1 and out-of-plane coupling and K_3. These equations can be used to determine the PC coupling coefficients from the band structure. Taylor *et, al.,* [5] found that coupling is dependent on atom radius (which is explored in detail in this chapter).

$$\omega_{c,d} = \frac{c}{n_{ave}}(\beta_0 + K_3)\left(1 - \frac{4K_1^2}{\beta_0^2 - K_3^2}\right) \tag{10}$$

$$\omega_b = \frac{c}{n_{ave}}(\beta_0 - K_3) \tag{11}$$

$$\omega_a = \frac{c}{n_{ave}}(\beta_0 - K_3)\left(1 - \frac{8K}{\beta_0^2 - K_3^2}\right) \tag{12}$$

Photonic band structure simulation can reveal various details about the expected performance of a PCSEL. In and out-of-plane coupling coefficients can be calculated using equations (10),(11) and (12) (Sakai *et, al,).* The frequency of the bands will give the possible lasing wavelengths and the in-plane magnetic field can determine the nature of the mode (discussed later).

Figure 2.9 shows the modelled in-plane magnetic field for 4 bands, where amplitudes of the magnetic field perpendicular to the plane are indicated with red and blue denoting negative and positive, respectively. Black circles represent the edge of the atom and black arrows represent in-plane electric field with arrow size representing intensity. The in-plane magnetic fields which are periodic in either the horizontal (b) or vertical (a) have directionally unified electric field vectors while the electric field vectors arising from (c) and (d) are anti-symmetric about the centre of the atom. Hence, a) and b) would give leaky modes with linear polarisation. While c) and d) would give non leaky modes [21-23], such a mode may give random polarisation as in a VCSEL[24-28].

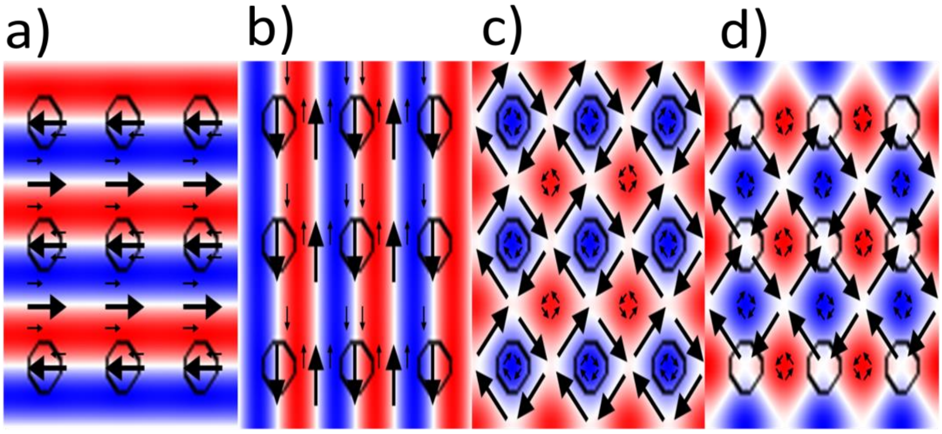

Figure 2.9 in-plane electric and magnetic fields of four bands at the gamma point for a PC with circular atoms on a square lattice, where amplitudes of the magnetic field perpendicular to the plane are indicated with red and blue denoting negative and positive, respectively, black circles represent the edge of the atom and black arrows represent in-plane electric field with arrow size representing intensity.

Type I vs Type II

To illustrate the effect that changing the refractive index contrast has upon a photonic crystal laser, and set the scene for a full discussion of the effect of changing the PC structure, figure 2.10(a) shows the band structure in the region of the gamma point. This is a type II GaAs/AlAs photonic crystal band structure for a range of frequencies between 0.29 and 0.33 c/a (where c is the speed of light and a is the lattice size). Figure 2.10(b) is a type I AlAs /GaAs photonic crystal band structure over the same range of frequencies. The insets show the in-plane magnetic field distribution for each band at the gamma point, the positive and negative amplitudes of the magnetic fields in the direction perpendicular to the plane are indicated by red and blue areas respectively.

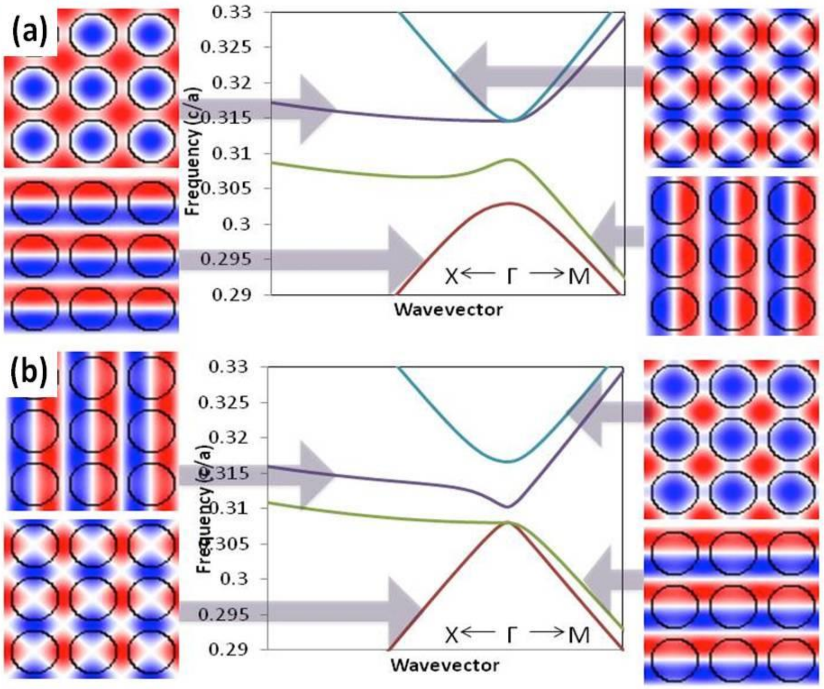

Figure 2.10 modelled band structure around the gamma point with 2.10(a) showing a type II GaAs/AlAs photonic crystal and 2.10(b) showing a type I AlAs/GaAs photonic crystal both shown over a frequency range of 0.29-0.33c/a

In the band structure for the type I PC the degenerate bands are the higher frequency bands whereas for the type II PC the degenerate bands are the lower frequency bands. A cursory inspection of the curves suggest that they are mirror images, but closer inspection (particularly of the split-off bands and band separation at the zone centre) indicates that this is not the case.

The symmetry of the in-plane electric field with regard to the unit cell centre determines the nature of the modes. If electric fields are anti symmetric with respect to the centre of the atom then destructive interference occurs and these modes are non leaky (i.e. they emit little light in the vertical direction) [21]. Leaky modes will emit light in the vertical direction and will be lossy prior to the lasing condition being met. This additional loss mechanism means that a higher gain is requires to reach lasing threshold (g_{th}), giving leaky modes a higher threshold than non-leaky modes. They will however have a higher output power once threshold is achieved. Non leaky modes on the other hand will have a lower g_{th} but a lower output power once threshold is achieved. Hence, attempts to design high power devices have focused on modifying non-leaky modes to become leaky [21-23]. An inspection of the magnetic field plot allows us to determine whether the modes are leaky or non leaky, important in device design [21-23].

In the type II PC (Figure 2.10(a)), the higher frequency degenerate bands are non-leaky due to the anti-symmetric nature of the electric fields. The two lower non-degenerate bands will be leaky. This contrasts the case for the type I structure (Figure 2.10(b)), where the anti-symmetric bands are the highest frequency non-degenerate band and one of the degenerate bands. The 4 bands also have different band edge frequencies which will result in them emitting light of a different frequency, even though the volume of A and B regions is equal.

This highlights the complexity of PC design. The nature of the mode is a key design parameter: low power applications benefit from a low threshold current density, so non-leaky modes would be desirable in this case; high power applications benefit from light scattered out of plane, so leaky modes are desirable though threshold current will be sacrificed. From the in-plane magnetic field it is possible to determine the mode polarisation which may also be a design parameter for the intended application. The format of the band-structure depends upon the PC structure and the emission wavelength depends on the period. Finally, from equations (10),(11) and (12) [29] the band structure can be used to interpret the expected coupling coefficients. Where, K_1 corresponds to out-of-plane coupling and K_3 corresponds to in-plane coupling. High in-plane coupling will give feedback and (like a leaky mode) will give low threshold, while high out-of-plane coupling will give high power.

2.2 Band Structure Variation

This section explores the effect of varying the hole size for both type I (InGaP/GaAs) and type II (GaAs/InGaP) photonic crystal lasers on the photonic band structure. Band structures are shown for PCs where the atom radius is between 0.1a and 0.4a.

Type I

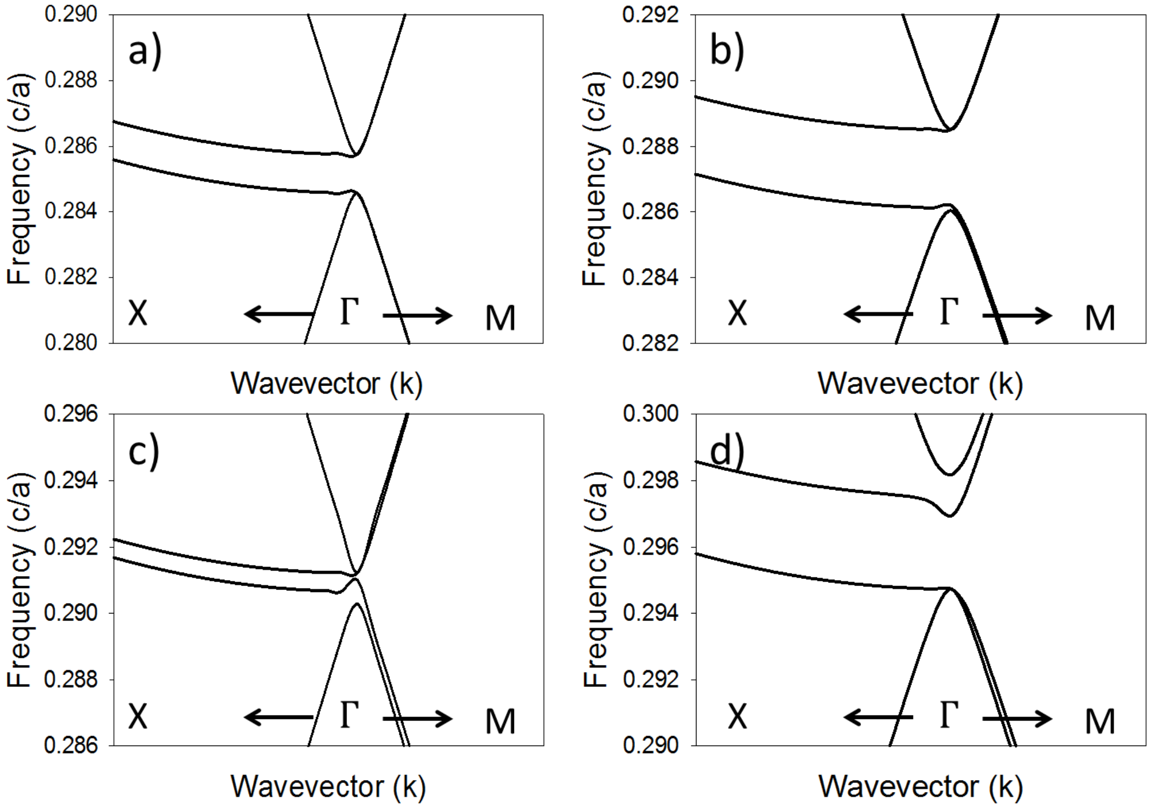

Figure 2.11 modelled photonic band structure for a type I InGaP/GaAs photonic crystal with circular atoms on a square lattice for radius a) 0.1a b) 0.2a c) 0.3a d) 0.4a

Figures 2.11 a), b), c) & d), plot the photonic band structure around the gamma point of a type I InGaP/GaAs photonic crystal for atom radii of 0.1a, 0.2a, 0.3a, and 0.4a, respectively. As the atom radius increases the band structure is seen to change. For r=0.1a (Figure 2.11a) both pairs of bands (2 higher energy and 2 lower energy bands) are degenerate. As r increases to 0.2a (Figure 2.11 b), the higher energy bands remain degenerate and the lower energy bands become non degenerate. As r increases to ~0.3a (figure 2.11c) the bands have shifted and become overlapped leaving no zone centre separation. Finally at r=0.4a (figure 2.11d) the zone centre separation has re-emerged with the higher frequency bands being split and the lower frequency bands being degenerate. As the radius r increases the frequency of each band increases and the average frequency of 4 bands at k=0 increases. This can be used to estimate/design the surface emission wavelength of a PCSEL, based upon the normalised frequency given being c/a.

Type II

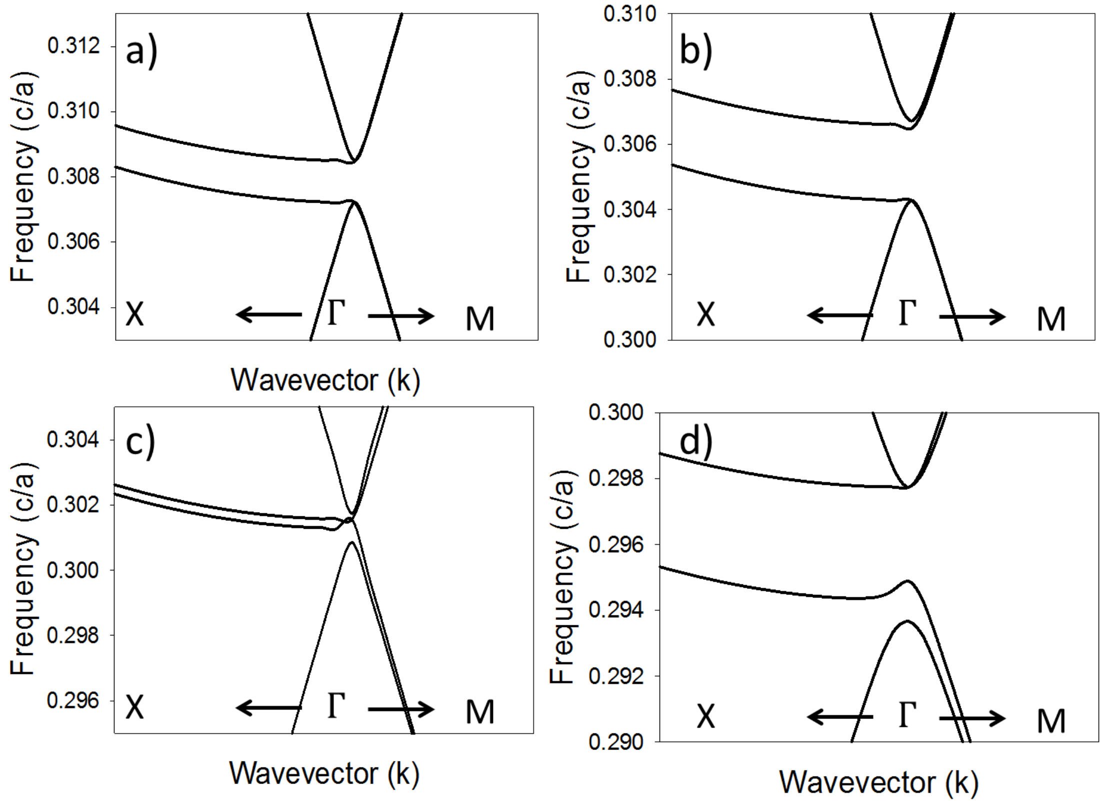

Figure 2.12 modelled photonic band structure for a type II GaAs/InGaP photonic crystal with circular atoms on a square lattice for radius a) 0.1a b) 0.2a c) 0.3a d) 0.4a

Figures 2.12 a), b), c) and D) plot the photonic band structure around the gamma point of a type II GaAs/ InGaP photonic crystal for atom radii of 0.1a, 0.2a, 0.3a, and 0.4a, respectively. As the atom radius increases the band structure is seen to change. For r=0.1a (Figure 2.12a) both pairs of bands (2 higher energy and 2 lower energy bands) are degenerate. As r increases to 0.2a (Figure 2.12b), the lower energy bands are degenerate and the higher energy bands are non degenerate. Again, as r increases to ~0.3a (figure 2.12c) the bands have shifted and become overlapped leaving no zone centre separation. Finally at r=0.4a (figure 2.12d) the zone centre separation has re-emerged with the lower frequency bands being split and the higher frequency bands being degenerate. As the radius r increases the frequency of each band increases and the centre frequency decreases.

Summary – Band Structure Variation

For both type I and type II structures the band structure is observed to change as atom radius increases. For type I, the higher frequency bands are degenerate for r~≥0.2a and the lower frequency bands are split, as r increases to ~0.3a the bands have shifted and overlapped leaving no zone centre separation, as the radius is increased further (to r=0.4a) the zone centre separation has re-emerged with the lower frequency bands being degenerate and the higher frequency bands being split. For type II: the higher frequency bands are split for r~≥0.2a but the lower frequency bands are degenerate. As r increases to ~0.3a the bands also shift and overlap leaving no zone centre separation. Again, as the radius is increased further (to r=0.4a) the zone centre separation has re-emerged but with the lower frequency bands being split and the higher frequency bands being degenerate. It is also of note that the centre frequency of the bands shifts in frequency; for type II the centre frequency increases as r increases while for type I the centre frequency decreases as r increases. This is in line with the change in n_{ave} being in the opposite sense for the two types of PC.

2.3 Coupling Calculation

There are multiple coupling mechanism within a photonic crystal, notably there is coupling that occurs in-plane (K_3) and there is coupling which is vertically out-of-plane (K_1) [21]. The band structure can be used to estimate these coupling coefficients [5, 29] from equations (10), (11) and (12). This section initially examines the band splitting of type I (InGaP/GaAs) and type II (GaAs/InGaP) PC then the coupling is calculated for a range of atom radius.

Figure 2.13 shows the measured band splitting (from modelling of the band structure), as radius increases from 0.01a to 0.5a, for a type I InGaP/GaAs PC. The splitting (frequency difference) between the 2 lowest frequency bands is shown with a solid line, the splitting between the 2 highest frequency bands is shown with a dotted line, and the difference between the highest and lowest frequency bands is shown with a dashed line.

Substituting frequency values into equations (10), (11) and (12) allows a simultaneous equation to be solved determining K_1 and K_3 for each atom size. The calculated values of K_1 and K_3 are plotted in figure 2.14. Values are normalised as the calculation considers an infinite PC thickness. For the calculation, I maintain the formalism that $w_{c/d}$ are the degenerate bands. In cases where no degenerate bands exist they are either the two highest (type I) or two lowest bands (type II). ω_a is the highest frequency of the two non-degenerate bands, when the degenerate bands are at low frequency, and is the lowest frequency when degenerate bands are at higher frequency.

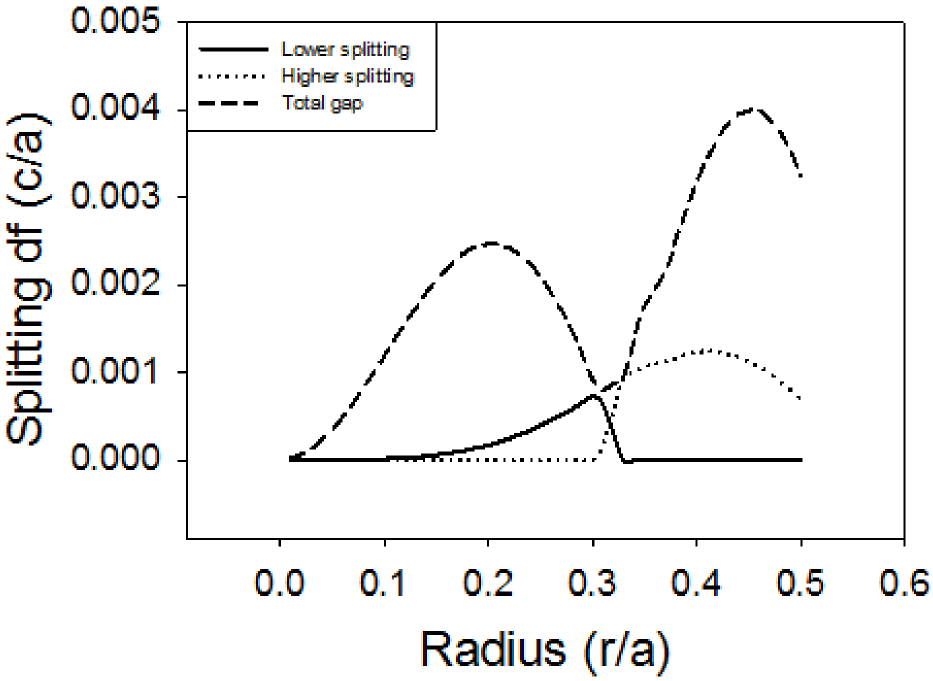

Figure 2.13 frequency splitting for lower splitting (solid line) higher splitting (dotted line) and total gap (dashed line)

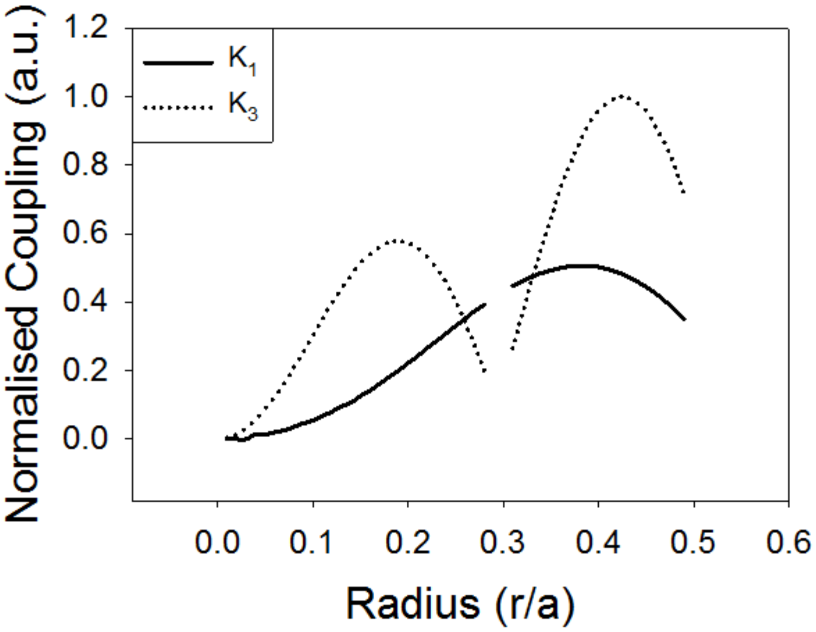

Figure 2.14 Coupling K_1 (Solid line) and K_3 (dotted line) for radius from 0.01a to 0.5a

The coupling coefficient, K_1, increases as the atom radius increases. When the volume of the atom is equal to the volume of the background (when the radius is ~0.4a) the coupling, K_1, is at a maximum. At radii greater than 0.4a the K_1 coupling decreases. At radius ~0.3a, the bands overlap and the assignment of degenerate and split off bands is not possible, as such this region is excluded from the plot. The coupling coefficient K_3 increases as atom radius increases for $0.01a<r<0.2a$, at $r\sim0.2a$ there is a local maxima and K_3 decreases as radius increases between $0.2a<r<0.3a$. Again, coupling is not plotted for $r\sim0.3a$, K_3 increases as radius increases for $0.3a<r<0.45a$ to a global maxima at $r=0.45a$, and decrease as r is further increased.

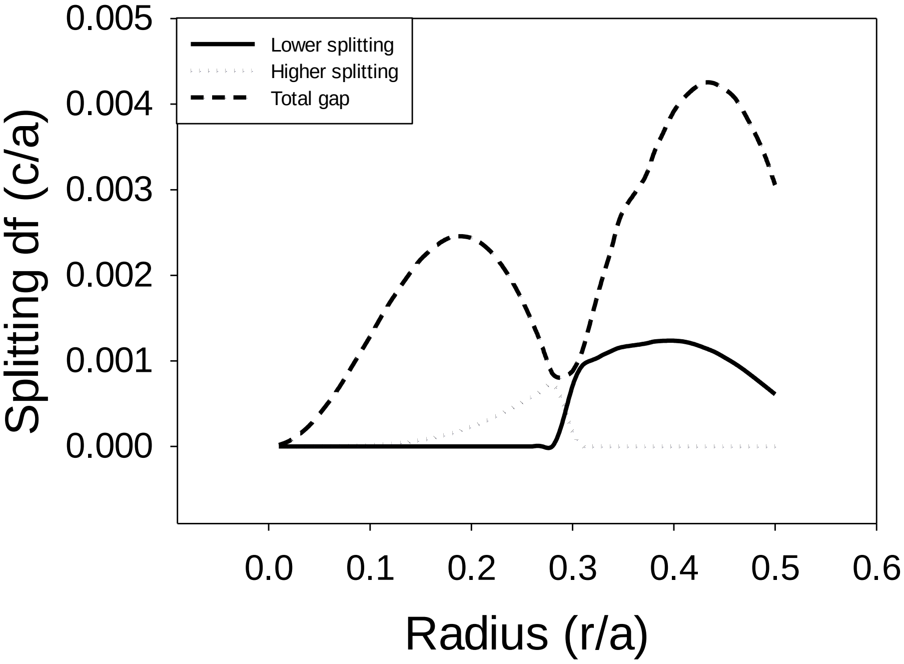

Figure 2.15 frequency splitting for lower splitting (solid line) Higher splitting (dotted line) and total gap (dashed line)

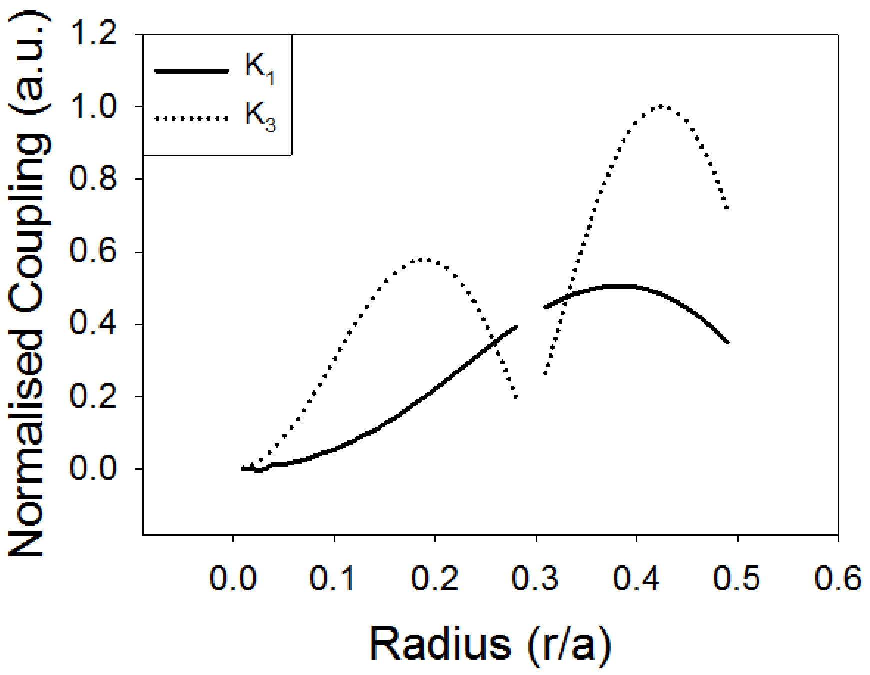

Figure 2.16 Coupling K_1 (Solid line) and K_3 (dotted line) for radius from 0.01a to 0.5a

Figure 2.15 shows the band splitting in a similar manner, from modelled band structure, as radius increases from 0.01a to 0.5a, for a type II GaAs/InGaP PC. Figure 2.16 shows the calculated values of K_1 and K_3 for a type II PC. Very similar trends are observed as in the type II structure with K_1 and K_3 plots being essentially identical.

Summary – Coupling Calculation

In this section in-plane and out-of-plane coupling for type I (InGaP/GaAs) and type II (GaAs/InGaP) PC with circular “atoms” on a square lattice are calculated from modelled band structure. Both PC types follow a similar pattern with the out-of-plane coupling K_1 having a peak at r~0.4a and in-plane coupling K_3 having 2 peaks at r~0.15a and r~0.45a. A choice of r~0.15a results in moderately high K_3 (in-plane coupling) and low K_1 out-of-plane coupling. On the other hand a choice of r~0.45a results in both K_3 and K_1(out-of-plane coupling) being high. The double peak nature of the in-plane coupling is similar to results founds by M. Yokoyama and S. Noda [30] where Q-factor is found to be dependent on band structure and exhibits a double peak at r=0.15a and r=0.4a. A higher Q is obtained at r=0.15a. This is attributed to an increase in the in-plane coupling with increasing r. The independent control of the relative strength of K_3 and K_1, with atom radius is highlighted in this section and is expected to be a valuable tool in PCSEL optimisation.

2.4 Magnetic Field Distribution

The in-plane magnetic field distribution of a PC band reveals information about the band, as discussed in chapter 1. If the electric field is anti-symmetric about the centre of the atom then light scattered out-of-plane will be in anti-phase and the band will be non-leaky [21]. The in-plane field also gives information about the polarisation of light emitted from that band [22, 23]. If the electric field vectors are not unified to one direction then polarization of the mode may be random as in a VCSEL. Directionally unified electric field vectors lead to linear polarisation. There is added complexity in cases where bands are degenerate, as the lasing at that band edge will have components from each band. This section considers the modelled in-plane magnetic field of the 4 bands at the Γ-point for a range of atom radius (0.1a, 0.2a, 0.3a and 0.4a) and determines which bands would be leaky and non-leaky and what the expected polarisation will be.

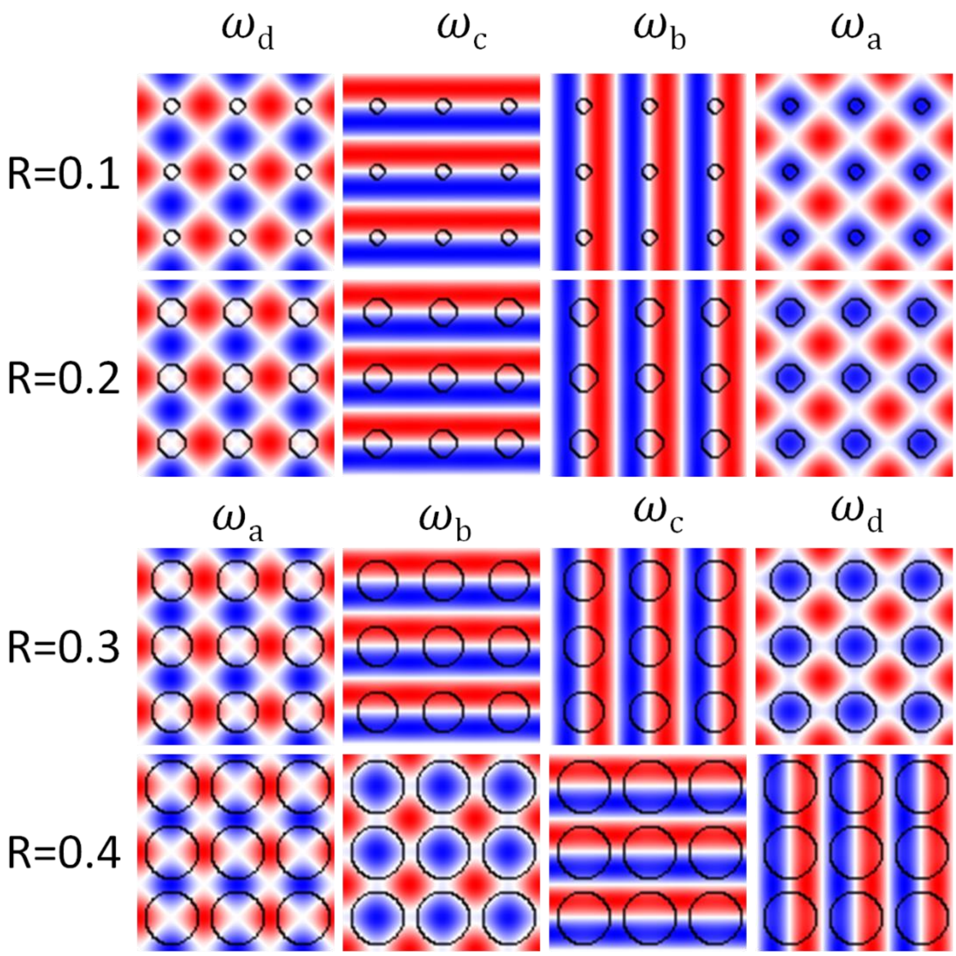

Figure 2.17 modelled in-plane magnetic field distribution of a type I (InGaP/GaAs) PC for each of the 4 bands at the Γ_2 point. Amplitudes of the magnetic field perpendicular to the plane are indicated with red and blue denoting negative and positive, respectively. Black circles indicate the boundary between atom and background.

Figure 2.17 shows the in-plane magnetic field distribution of a type I InGaP/GaAs PC for each of the 4 bands at the Γ_2 point. Results are again modelled using MPB. Amplitudes of the magnetic field perpendicular to the plane are indicated with red and blue denoting negative and positive, respectively. Black circles indicate the boundary between atom and background.

The top row shows the fields of each band for r=0.1a. Bands 1 and 4 have a magnetic field distribution that will give an electric field that is anti-symmetric about the centre of the atom; as such the bands are expected to be non-leaky and to have a complicated polarisation. Bands

2 and 3 have a magnetic field distribution periodic in the vertical and horizontal direction, respectively. These bands are expected to be leaky and to have linear polarisation. For bands 1, 2 and 3 at the centre of the atom the magnetic field is 0 while for band 4 the magnetic field is at its most negative. The second and third rows show the fields of each band for r=0.2a and r=0.3a, respectively. The same characteristic is observed as that discussed for r=0.1a.

The fourth row shows the fields of each band for r=0.4a. Bands 1 and 2 have a magnetic field distribution that is anti-symmetric about the centre of the atom; the bands are expected to be non-leaky and may have a random polarisation. Bands 3 and 4 have a magnetic field distribution that is periodic in the vertical and horizontal direction, respectively. The bands are expected to be leaky and to have linear polarisation. For bands 1, 2 and 3 at the centre of the atom the magnetic field is 0 while for band 4 the magnetic field is most negative. Bands 1 and 2 in this case are degenerate. Previous results for all-semiconductor PCSELs has shown lasing from the split band exhibiting linear polarisation [14-16].

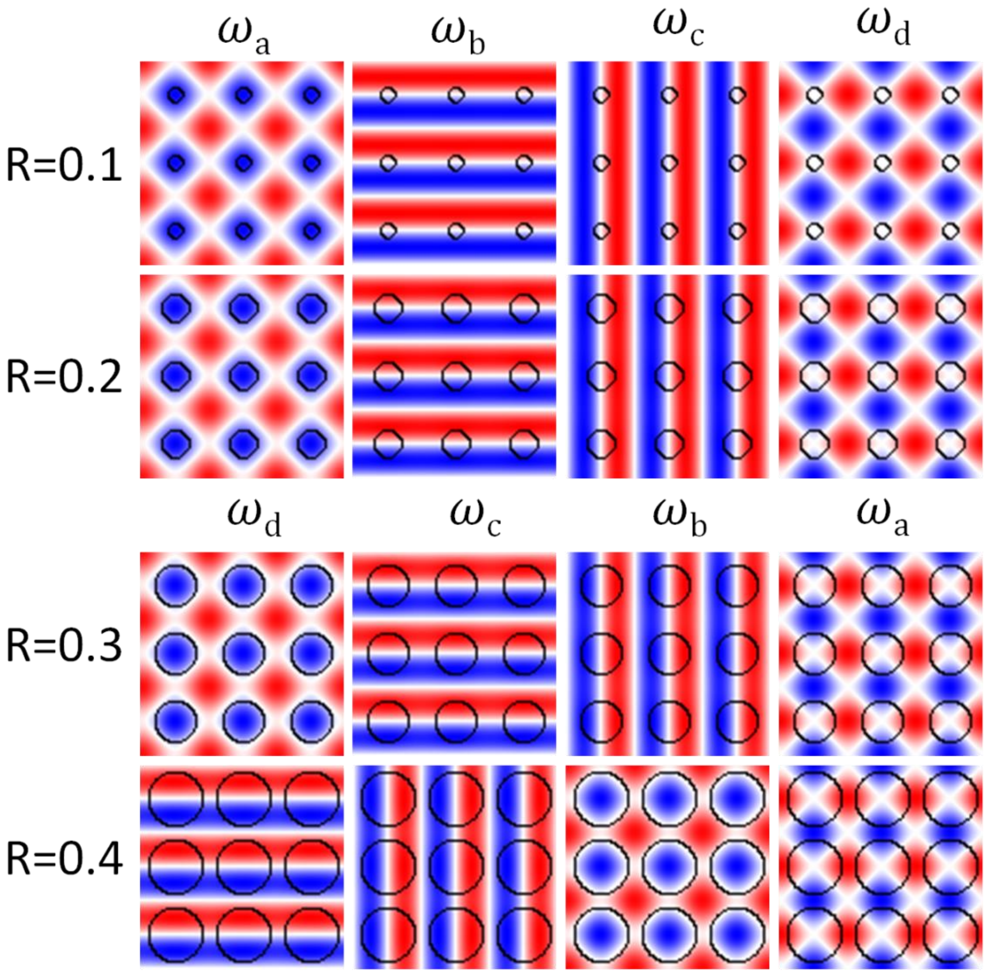

Figure 2.18 modelled in-plane magnetic field distribution of a type II (GaAs/ InGaP) PC for each of the 4 bands at the Γ_2 point. Amplitudes of the magnetic field perpendicular to the plane are indicated with red and blue denoting negative and positive, respectively. Black circles indicate the boundary between atom and background.

In a similar fashion, figure 2.18 shows the in-plane magnetic field distribution of a type I GaAs/ InGaP PC for each of the 4 bands at the Γ_2 point.

The top row shows the fields of each band for r=0.1a. Bands 1 and 4 have a magnetic field distribution that gives an electric field which is anti-symmetric about the centre of the atom. As such the bands are non-leaky and have a complicated polarisation. Bands 2 and 3 have a magnetic field distribution that gives an electric field that is periodic in the vertical and horizontal direction respectively; the bands are expected to be leaky and to have linear polarisation. For bands 1, 2 and 3 at the centre of the atom the magnetic field is 0 while for band 4 the magnetic field is at its most negative. The second and third rows show the fields of each band for r=0.2a and r=0.3a, respectively. Again, a similar characteristic is observed for r=0.1a-0.3a

The fourth row shows the fields of each band for r=0.4a. Bands 1 and 2 have a magnetic field distribution that is periodic in the vertical and horizontal direction, respectively. These bands are expected to be leaky and to have linear polarisation. Bands 3 and 4 have a magnetic field distribution that gives an electric field which is anti-symmetric about the centre of the atom. These bands are expected to be non-leaky and to have a complicated polarisation. For bands 1, 2 and 3 at the centre of the atom the magnetic field is 0 while for band 4 the magnetic field is most negative.

Summary - Magnetic Field Distribution

In addition to design considerations mentioned previously with respect to the relative strength of K_1 and $K_{3,}$ the effects of the magnetic field distribution brings about additional design considerations. Figure 2.19 plots the band structure of type I (InGaP/GaAs) and type II (GaAs/InGaP) photonic crystal with a circular atom on a square lattice for r=0.2a and r=0.4a. Indicating which bands are leaky and which are non-leaky.

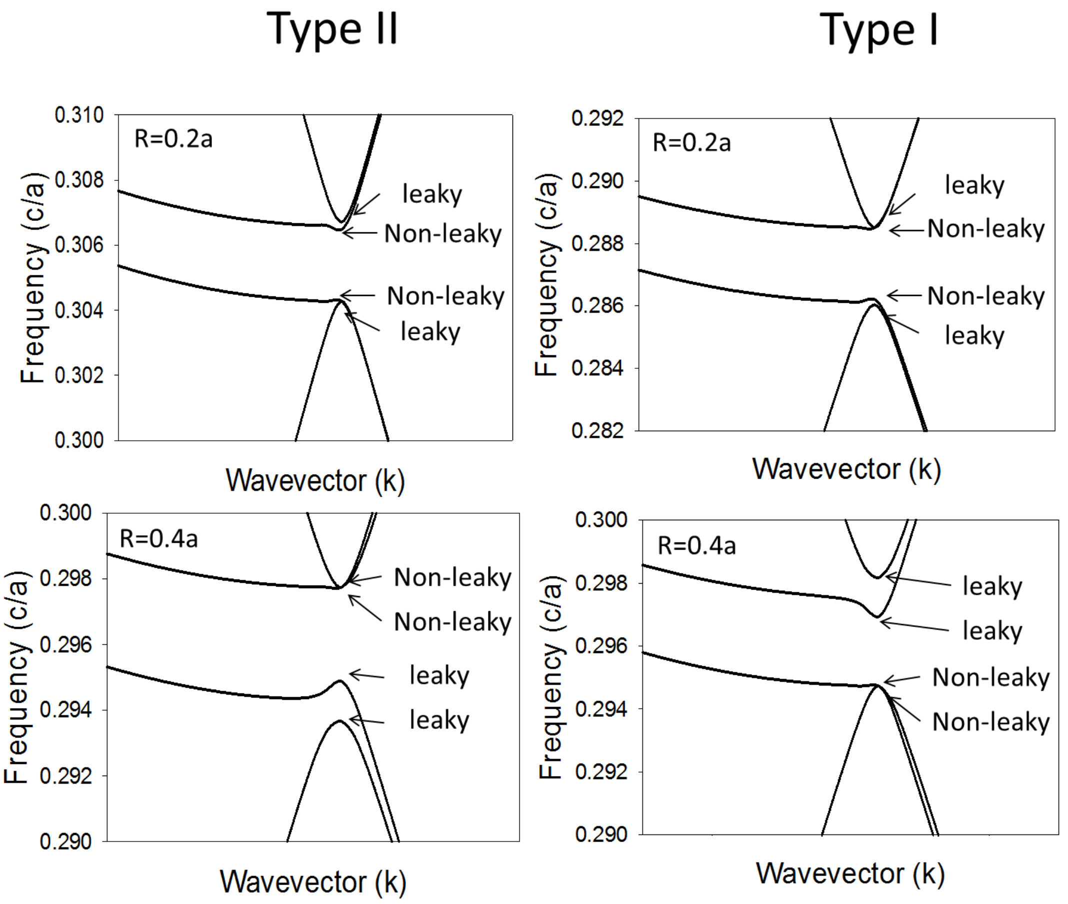

Figure 2.19 band structure of type I (InGaP/GaAs) and type II (GaAs/InGaP) photonic crystal where r=0.2a and 0.4a, showing which bands are leaky and which are non-leaky

For r~0.2a (highlighted as ideal for high Q, high K$_3$, low K$_1$) the choice of lasing band is limited in both type I and type II structures as there is only one non-degenerate non-leaky mode. A limited separation between the lasing band and its neighbouring mode is noted. It is also noted that the only non-degenerate non-leaky mode has a high dυ/dk away from the zone centre. The lower density of states with group velocity of 0 should lead to a comparatively high threshold, low divergence and low increase in divergence with increasing power.

For r~0.4a (highest K$_1$, K$_3$) in both type I and type II the leaky modes are non-degenerate and well separated. Positioning the gain band to higher or lower frequencies than the average frequency should enable required leaky band to be selected. Here a choice of lasing bands is possible with a range of dυ/dk outside the zone centre.

2.5 Conclusion

In this chapter the band structure of type I (InGaP/GaAs) and type II (GaAs/InGaP) PCs with a circular atom on a square lattice was modelled and analysed. The band structure was observed to change as the radius of the atom increases in particular a change in which bands are degenerate and which bands are non-degenerate is noted. From the modelling of the band structure the in-plane and out-of-plane coupling coefficients were calculated and showed a peak for both K_3 (in-plane coupling) and K_1 (out-of-plane coupling) at r~0.4a. The in-plane coupling (K_3) is observed to have a local maximum at r=0.2a. The out-of-plane coupling (K_1) is very low at this point. This result is similar to results founds by M. Yokoyama and S. Noda [30] where Q-factor is found to be dependent on band structure and exhibits a double peak at r=0.15a and r=0.4a. The low k_1 at this point results in Q being maximal at r=0.15a.

Finally, the in-plane magnetic fields of each of the calculated bands were plotted and analysed to determine which of the bands were leaky, which were non-leaky and the polarisation of those bands. The impact of this on the design of the PCSEL has been discussed.

References

[1] S. Xiao, L. Shen and S. He,

"A plane-wave expansion method based on the effective medium theory for calculating the band structure of a two-dimensional photonic crystal"

Physics Letters A, **313**, 132, 2003

[2] M. Qiu and S. He

"A non-orthogonal finite-difference time-domain method for computing the band structure of a two-dimensional photonic crystal with dielectric and metallic inclusions"

Journal of applied physics, **87**, No. 12, 8268, 2000

[3] K. Sakai, J. Yeu, S. Noda

"Coupled-wave model for triangular lattice photonic crystal with transverse electric polarisation"

Optics express, **16**, 9, 6033, 2008

[4] http://ab-initio.mit.edu/wiki/index.php/MIT_Photonic_Bands

[5] R. Taylor, D Williams, D. Childs, J. Orchard, S. Khamas, K. Groom, R. Hogg,.

"Band structure and waveguide modelling of epitaxially regrown photonic crystal surface emitting lasers"

Journal of Physics D, 46, 26, 2013

[6] J. Joannopoulos, S. Johnson,

“Photonic crystals modelling the flow of light”

Second edition, Princeton University Press, 2007

[7] C**.** Kitel

”introduction to solid state physics”

8th edition, wiley, 2005

[8] J. Hook and H. Hall

“solid state physics”

Second edition, wiley, 2007

[9] J. Joannopoulos, S. Johnson

”Photonic crystals: modelling the flow of light”

Second edition, Princeton university press, chapter 5, page 83, 2008

[10] B. Ellis, M. Mayer, G. Shambat, T. Sarmiento, J. Harris, E. Haller & J Vučković,

“Ultralow-threshold electrically pumped quantum-dot photonic-crystal nanocavity laser”

Nature Photonics, **5**, 297–300, 2011

[11] M. Lončar, T. Yoshie, A. Scherer, P. Gogna andY. Qiu

“Low-threshold photonic crystal laser”

Applied physics letters, **81**, 2680, 2002

[12] O. Painter, R. Lee, A. Scherer, A. Yariv, J. O'Brien,P. D. Dapkus, I. Kim

“Two-Dimensional Photonic Band-Gap Defect Mode Laser”

Science, **284**, 5421, 1819-1821, 1999

[13] K. Hirose, Y. Liang, Y. Kurosaka, A. Watanabe, T. Sugiyama & S. Noda

”Watt-class high-power, high-beam-quality photonic-crystal lasers”

Nature Photonics, **8**, 406-411, 2014

[14] D. Williams

“All-semiconductor photonic crystal surface emitting lasers at 980 nm through epitaxial regrowth”

PhD thesis, University of Sheffield, 58, 2014

[15] D. Williams, K. Groom, D. Childs, R. Taylor, S. Khamas, R. Hogg, B. Stevens, N. Ikeda, Y. Sugimoto

“Optimisation of coupling between photonic crystal and active elements in an epitaxially regrown GaAs based photonic crystal surface emitting laser”

Japanese journal of applied physics, **51**, 02BG05-1-3, February 2012

[16] D. Williams, K. Groom, D. Childs, R. Taylor, S. Khamas, R. Hogg, B. Stevens, N. Ikeda, Y. Sugimoto

"Epitaxially regrown GaAs-based photonic crystal surface emitting laser"

IEEE photonics technology letters, **24**, 11, 966-968, June 2012

[17] M. Imada, S. Noda, A. Chutinan, T. Tokuda, M. Murata and G. Sasaki.

"Coherent two-dimensional lasing action in surface-emitting laser with triangular-lattice photonic crystal structure"

Applied Physics Letters, **75**, 3, 316, 1999

[18] D. Ohnishi, T. Okano, M. Imada and S. Noda

"Room temperature continuous wave operation of a surface emitting two dimensional photonic crystal laser"

Optics Express, **12**, No. 8, 1562, 2004

[19] K. Sakai, E. Miyai, T. Sakaguchi, D. Ohnishi, T. Okano and S. Noda.

"Lasing band edge identi_cation for a surface-emitting photonic crystal laser"

IEEE Journal of Selected Areas of Communication., **23**, No. 7, 1335, 2005

[20] R. Taylor, D. Williams, D. Childs, B. Stevens, L. Shepherd, S. Khamas, K. Groom, R. Hogg, N. Ikeda, and Y. Sugimoto

"Photonic crystal surface emitting lasers based on epitaxial regrowth"

IEEE Journal of Selected Topics in Quantum Electronics, **19**, 4, 4900407, 2013

[21] Y. Kurosaka, K. Sakai, E. Miyai, S. Noda, “Controlling vertical optical confinement in two-dimensional surface-emitting photonic-crystal lasers by shape of air holes”

Optics express, 16, 22, 1848-18494, October 2008

[22] M. Yokoyama, S. Noda

“Polarisation mode control of two-dimensional photomic crystal laser having a square lattice structure”

IEEE journal of quantum electronics,**39**, 9, 1074,2003

[23] S. Noda, M. Yokoyama, A. Chutinan, M. Imada, M. Mochizuki

“Polarization Mode Control of Two-Dimensional Photonic Crystal Laser by Unit Cell Structure Design”

Science, **293**, 1123, 2001

[24] C. Wilmsen, H. Tekin, L. Coldren

“Vertical-cavity surface-emitting lasers: design, fabrication, characterisation, and applications”

Cambridge university press, chapter 6, page 243, 1999

[25] K. Choquette, R. Schneider, K. Lear, R. Leibenguth

”Gain-dependant polarisation properties of vertical-cavity lasers”

IEEE journal of selected topics in quantum electronics, **1**, 661-665, 195

[26] S. jiang, Z. Pan, M. Dagenais, R. Morgan, and K. Kojima

”High frequency polarisation self-modulation in vertical-cavity surface-emitting lasers”

Applied physics letters, **63**, 26, 1993

[27] K. Choquette, D. Richie, and R. Leibenguth

“Temperature dependence of gainguided verticalcavity surface emitting laser polarisation”

Applied physics letters, **64**, 2062, 1994

[28] D. Kuksenkov, H. Temkin, and S. Swirhun

”Polarisation instability and relative intensity noise in vertical-cavity surface-emitting lasers”

Applied physics letters, **67**, 2141, 1995

[29] K. Sakai, E. Miyai and S. Noda

“Coupled-wave model for square-lattice two-dimensional photonic crystal with transverse-electric-like mode”

Applied physics letters, **89,** 021101, 2006

[30] M. Yokoyama and S. Noda,

“Finite-difference time-domain simulation of two-dimensional photonic crystal surface-emitting laser”

Optics express, **13**, 8, 2869, 2005

3. Wave Guide Modelling

As has been shown in chapter 1 a PC can be placed within a laser structure to produce a PCSEL. In such a structure it is the PC which provides feedback, and it is therefore crucial that a PCSEL structure produces high overlap of the vertical mode and the PC region if a high power per unit area is to be obtained. In order to design the structure of a semiconductor laser, it is useful to be able to model the wave guide and evaluate which aspects of the structure have a significant impact on the optical mode. In the case of a PCSEL the key design parameters are those which affect the modal overlap with the PC, active regions and lossy heavily doped cladding regions.

Williams *et, al.,* [1-3] demonstrated the first all-semiconductor PCSEL based on GaAs epitaxial overgrowth operating at 980nm. By modelling the structure as a 1D waveguide they were able to show that the all-semiconductor PCSEL had a higher mode overlap than the same structure with a void containing PC region. The conclusion was that the low average refractive index of the void containing region distorted the mode and pushed it away from the PC region. The higher mode overlap of the all-semiconductor PCSEL was attributed to the refractive index of the PC region being similar to the rest of the waveguide. They did not however, explore the possibility of re-designing the structure to counter the effect of the void containing PC region, nor did they consider material systems suited to other wavelengths.

This chapter initially considers multiple structural designs for PCSELs operating at wavelengths in the region of 980nm, based on GaAs and its alloys. Structures are modelled as a one dimensional wave guide where the photonic crystal layers are considered as a single layer with a refractive index given by a weighted average of the refractive index of its constituent parts. The allowed optical modes are calculated using the fully-vectorial software

FIMMWAVE [4]. FIMMWAVE uses a mode matching method to model a wave guide as a set of vertical slices. [5] The mode profile which the structure generates is modelled and, from the mode profile, the PC coupling is calculated. In all GaAs based cases, the PC region consists of GaAs and InGaP with a 50% fill. A 50% volume fill is optimal for PC coupling (r=0.4a) [6] (discussed in chapter 2). The optimal Bragg diffraction out of the PC plane occurs when PC thickness $T = \frac{(2m-1)}{2}\frac{\lambda_0}{n}$, (where m is a real positive integer, n is refractive index and $\boldsymbol{\lambda}_0$ is vacuum wavelength) for m=1 and $\boldsymbol{\lambda}_0$=980nm, T=150nm [1], the PC layer thickness is 150nm.

Initially the structure from Williams *et, al.,* is modelled to confirm that results are similar. The structure is modified to include an additional GaAs waveguide layer (termed ballast layer) and to include an additional PC layer (termed double decker), in order to increase the modal overlap with the PC by distorting the mode and making the waveguide symmetric, respectively. These structures are modelled in the same way and compared to the original structure. Finally PCSEL structures operating at different wavelengths (i.e. ~400nm, 1300nm and 10μm) and material systems are considered (i.e. GaN and InP). For each of these structures all-semiconductor and void containing PC regions are modelled to obtain coupling coefficients. This allows a more universal comparison of the use of all-semiconductor, or void containing PCSELs.

3.1 Theory

An optical mode can be considered as a distribution of optical energy in space over one (or more) dimensions. A waveguide contains the optical mode, which travel within and are confined by it. Commonly found wave guides include optical fibres, ridge lasers, etc.

Propagation of light can be described using Maxwell's wave equation

$$\nabla^2 \mathbf{E}_{(\mathbf{r},t)} = \left[\frac{n_{(\mathbf{r})}^2}{c^2}\right] \frac{\partial^2 \mathbf{E}_{(\mathbf{r},t)}}{\partial t^2} \tag{2.1}$$

Where **E** is the electric field, n is refractive index and c is the speed of light in a vacuum. From here the derivation will consider only the electric field (it is worth noting that the same derivation is possible for the magnetic field)

Monochromatic waves have the form,

$$\mathbf{E}_{(\mathbf{r},t)} = \mathbf{E}_{(\mathbf{x},\mathbf{y})} e^{i\omega t - \beta z} \tag{2.2}$$

Where ω is radian frequency and β is the propagation constant.

Combining 2.1 and 2.2 leads to the Helmholtz equation [7]

$$\frac{\partial^2 \mathbf{E}_{(x,y)}}{\partial x^2} + \frac{\partial^2 \mathbf{E}_{(x,y)}}{\partial y^2} + \left[k^2 n_{(r)}^2 - \beta^2\right] \mathbf{E}_{(x,y)} = 0 \tag{2.3}$$

This equation can be used to determine wave propagation in a material. For a structure containing multiple layers (of different materials), each layer must satisfy (2.3) but each boundary must have a continuous variation in **E.**

The simplest waveguide structure consists of three layers which are infinite in two planes (i.e. y and z) with each layer containing a different refractive index, shown in figure 3.1, where in this case $n_2>n_3>n_1$.

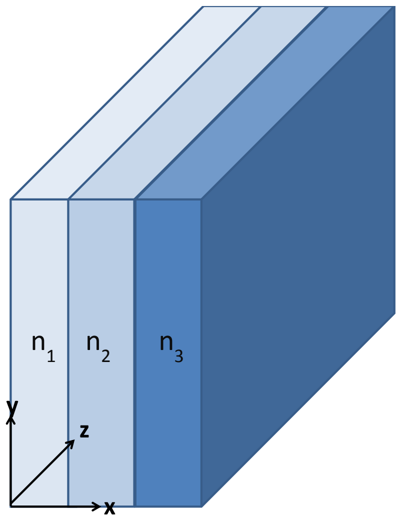

Figure 3.1 slab waveguide structure containing three layers

Consider waves propagating in the z direction with a fixed frequency ω and varying propagation constant β.

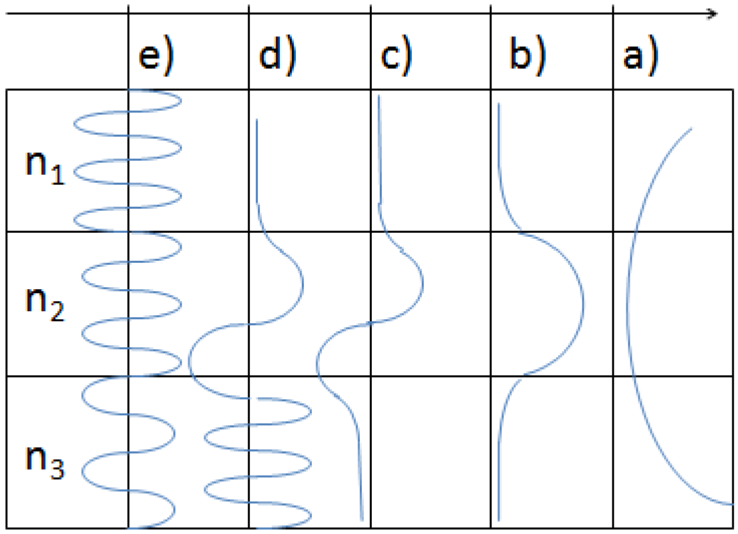

Figure 3.2 Diagram of possible modes in a planar waveguide

Figure 3.2 shows a schematic of the possible modes, for the structure shown in figure 3.1 mode a) represents $\beta > kn_2$; modes b) and c) represent the case where $kn_3 < \beta < kn_2$; mode d) represents $kn_1 < \beta < kn_3$ and mode e) $0 < \beta < kn_1$. Mode a) shows an unbound mode, where the electric field increases away from the centre of the structure [8] as the solution is unbound it does not represent a real wave. Unbound modes will be ignored.

3.2 Basic PCSEL Structure

This section considers a PC laser structure, similar to Williams *et al.*, [1-3] which consists of (from bottom to top) a n-type AlGaAs lower cladding layer, a three quantum well active layer consisting of three 8nm InGaAs quantum wells separated by 20nm GaAs layers, an etch stop layer, the photonic crystal region of 150nm which is InGaP/GaAs for the all-semiconductor case and InGaP/air for the void containing case, a p-type AlGaAs cladding layer and finally a highly doped p-type GaAs layer. The device is modelled as a 1D waveguide using FIMMWAVE [4]. The mode profile of the all-semiconductor PC region is then compared to a void containing PC region. During the fabrication of all-semiconductor PCSELs, due to possible reliability issues, the etching of the PC layer cannot intrude on the active layer, which means that one must either have complete confidence in the ability to control etch depth of the process or an etch stop layer should be included in the structure design. In this structure an etch stop layer is included, consisting of 20nm GaAs and 40nm of InGaP.

Structure

Figure 3.3 shows the layer structure of the PCSEL considered in this section. The structure can be used for either all-semiconductor or void containing PCSELs.

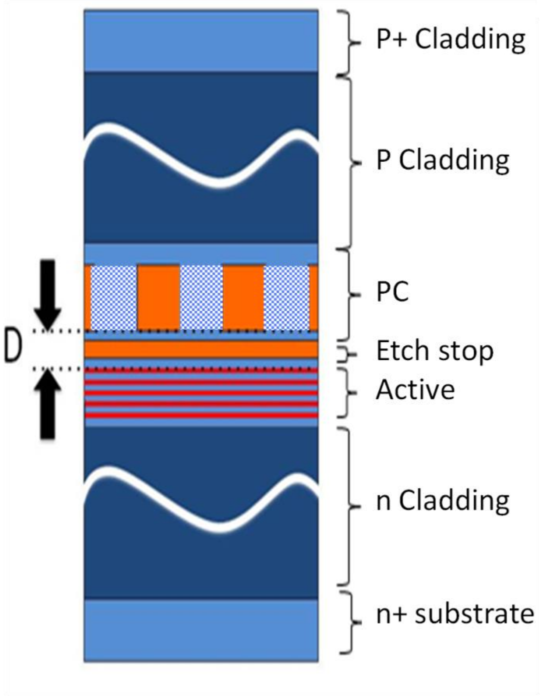

Figure 3.3 photonic crystal laser structure from Williams *et al.*,[1-3] from bottom to top a n-type cladding layer, a three quantum well active layer, an etch stop layer, the photonic crystal region, a p-type cladding layer and finally a highly doped p-type layer

Mode Profile

Figure 3.4a shows the modelled, normalised mode profile, overlaid upon the device structure for a void containing PCSEL (dashed line) and an all-semiconductor PCSEL (solid line). For the all-semiconductor structure the PC region consists of a 150nm thick layer containing an InGaP background with GaAs atom, where the atom volume is equal to the background volume. While for the void containing structure the PC region consists of a 150nm thick layer containing an InGaP background with air atom, where the atom volume is equal to the background volume. The upper and lower cladding are AlGaAs layers containing 40% Al.

It is observed that for the all-semiconductor PCSEL, much more of the mode overlaps with the PC and the mode peak is situated on the quantum wells. The void containing structure has very little mode overlap with the PC. For this void containing case, the low average refractive index of the PC layer distorts the mode and pushes it away from the PC region. This suggests that modification to the void containing structure design is required to maintain a bound mode and provide strong overlap with the PC region. For the all-semiconductor case the PC forms part of the waveguide, and benefits from a higher mode overlap with the PC.

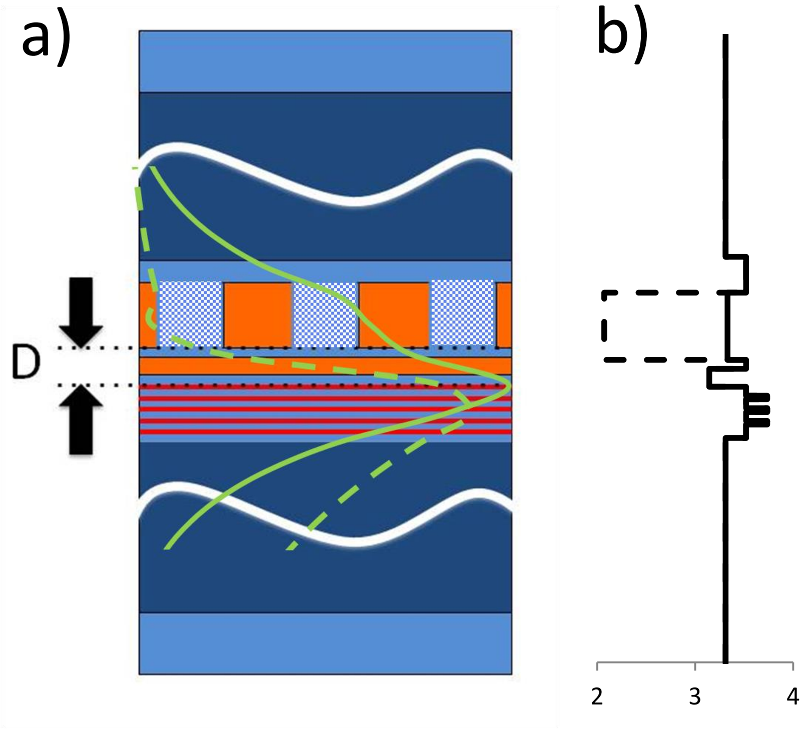

Figure 3.4 normalised mode intensity of InGaP/GaAs (solid) and InGaP/void (dashed) overlaid on the device structure b) the refractive index profile of the structure for InGaP/GaAs (solid) and InGaP/void (dashed)

Separation Distance Variation

From the mode overlap with the photonic crystal, it is possible to calculate the coupling coefficient

$$K_3 = \frac{2\,(\Gamma \times \Delta n)}{\lambda} \tag{1}$$

(where K_3 is the in-plane coupling coefficient, Γ is mode overlap with the PC, Δn is the difference in refractive index of materials in PC region and λ is wavelength) [9,10].

Here the effect of the position of the PC layer on $_{PC}$ coupling is considered, by increasing the AlGaAs thic$_{k}$ness between the QW active region and the PC.

Figure 3.6 shows the in-plane coupling coefficient (K_3) as separation width increases from 40nm to 200nm for all-semiconductor (solid) and void containing (dashed) PCSELs for a cladding layer Al composition of 40%. In both cases the coupling decreases as the separation thickness D increases, and as expected, coupling tends to zero for large values of D. The higher coupling for the all-semiconductor device may be surprising because the refractive index contrast (Δn) of a void containing photonic crystal is much greater. Despite the higher refractive index contrast in void containing PCs, the all-semiconductor PCSEL enjoys a higher PC coupling coefficient for this structure. The higher value of coupling for all-semiconductor PCSEL is due to higher mode overlap with the PC seen in figure 3.4 and, as discussed, is considered to be due to the modal distortion of the void containing PC region.

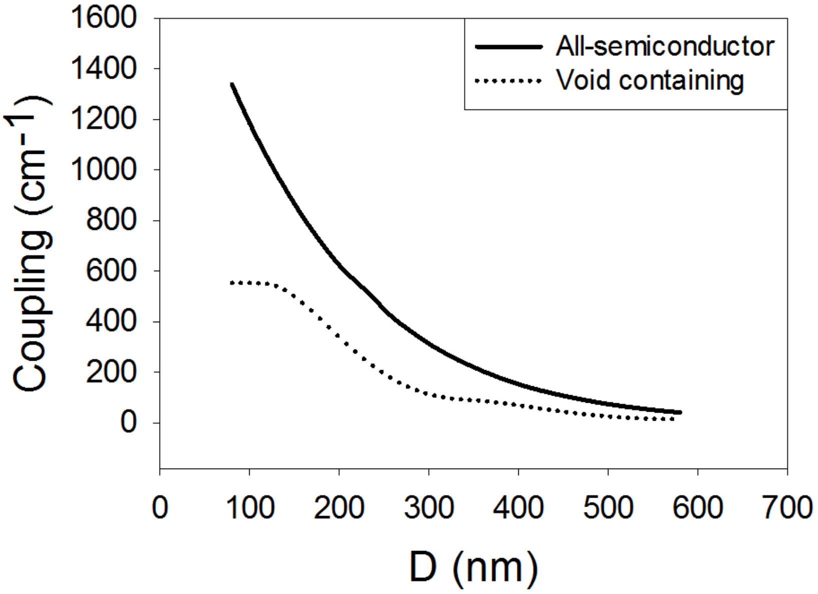

Figure 3.5 Coupling variation for seperation thickness D from 40 to 600nm for InGaP/GaAs (solid) and InGaP/void (dashed)

Varying Cladding Layer Aluminium Composition

A simple parameter to vary in order to push the mode upwards is the Al% in the lower cladding. Increasing the Al% should achieve this as with increase in Al% the refractive index reduces [11].

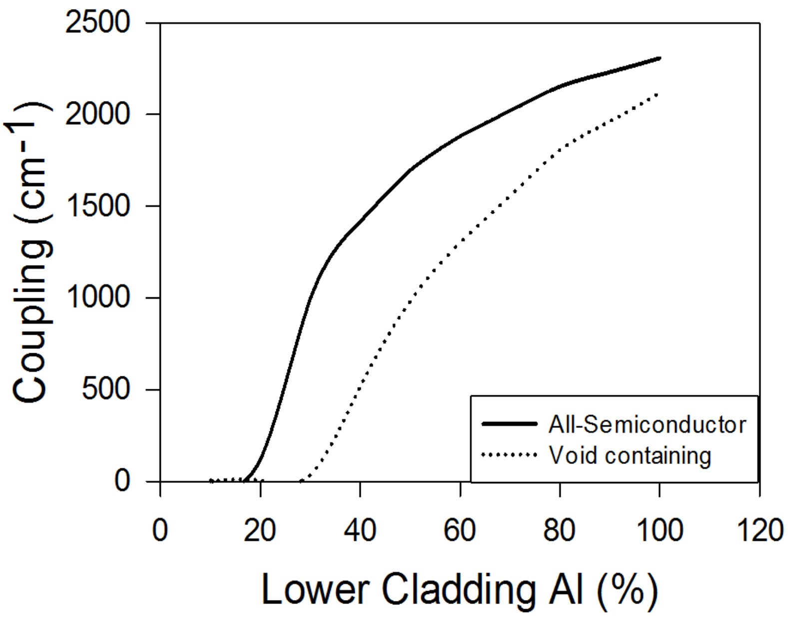

Figure 3.6 coupling variation as cladding layer Al % varies from 0 – 100% for all-semiconductor (solid) and void containing (dotted) PCSEL

Figure 3.6 shows the calculated PC coupling for lower cladding layer variation in Al composition, from 0-100%, for both all-semiconductor (solid line) and void containing (dotted line) PCSELs, in both cases the upper cladding layer Al composition is kept constant at 40%. In both cases the value of coupling increases with higher Al composition. The all-semiconductor device is observed to have a higher value of coupling for the full range of Al composition.

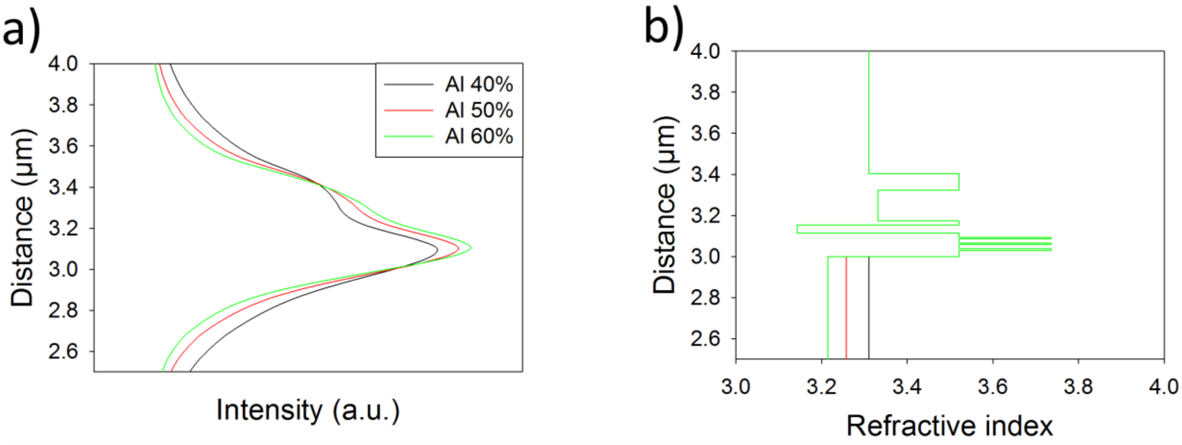

Figure 3.7a) normalised mode intensity of InGaP/GaAs PCSEL where the lower cladding Al composition is 40% (black), 50% (red) or 60% (green) b) the refractive index profile of the structures

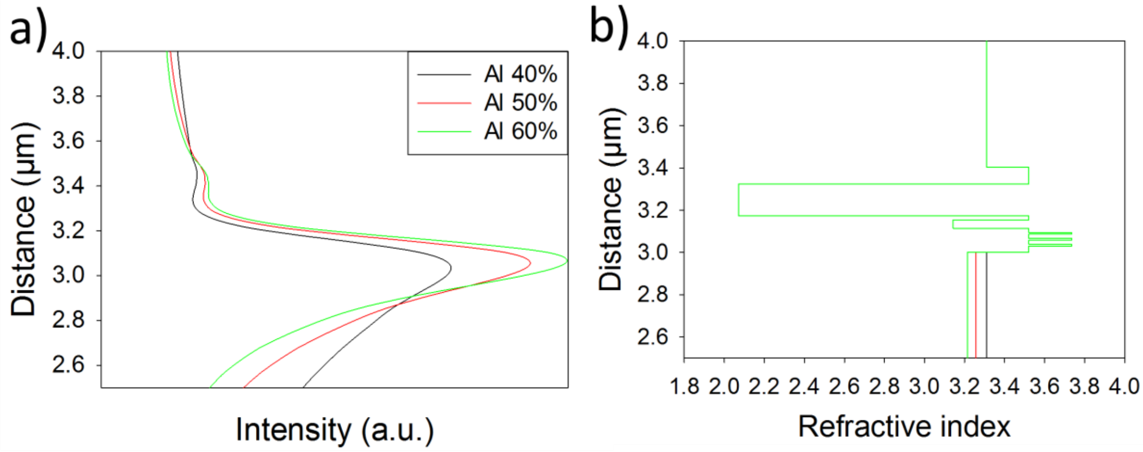

Figure 3.8a) normalised mode intensity of InGaP/void PCSEL where the lower cladding Al composition is 40% (black), 50% (red) or 60% (green) b) the refractive index profile of the structures

Figures 3.7 and 3.8 show the mode profile for an all semiconductor and void containing PCSEL respectively, in each case the lower cladding Aluminium composition is varied from 40 to 60%. For AlGaAs, higher Al composition reduces refractive index in the lower cladding layer and it is this reduction in refractive index that more tightly confines the mode and increases the coupling. This result seems to suggest that high aluminium composition is desirable. However AlGaAs becomes an indirect bandgap material at compositions higher than 40% [8,9, 12]which significantly reduces the conductivity of the material, increasing the resistance and degrading the electrical properties of the device, making this approach unattractive.

Varying the upper Al% had limited effect on the void containing PCSEL, as a bound mode was only found for 40% ± 5% Al composition. The fact that the mode is not well-bounds is evidenced by the mode profile in fig 3.4.

Summary – Basic PCSEL Waveguide

This section studied a basic PCSEL structure, considering the effects of cladding layer refractive index (varied through variation in Al composition in the AlGaAs region) and PC - QW separation thickness, for all-semiconductor and void containing photonic crystal layers. In the structure considered the all-semiconductor PCSEL gives higher PC coupling coefficients in all cases. Regardless of Al% in the cladding layers and PC position, the mode profile suggest that the low refractive index given by a weighted average of the refractive index of its constituent parts of a void containing PC region is acting to push the mode away from the PC region which is giving the all-semiconductor PCSEL higher coupling, in spite of the lower refractive index contrast (Δn) between mark and space.

3.3 Ballast Layer PCSEL

As discussed in section 3.2, PCSEL structures containing voids have low coupling of the optical mode to the photonic crystal because of the low refractive index of the PC layer distorting the optical mode. In order to address the problem of the low refractive index layer pushing the mode away (mentioned in the previous section), a structure is considered which uses an additional p-type GaAs waveguide region above the PC region in order to pull the mode peak higher in the structure and hopefully increase mode overlap with the PC region.

The possibility that this additional layer will increase the PC coupling, particularly for the void containing PCSEL, is expected by giving both high refractive index contrast (Δn) and high mode overlap (Γ).

Structure

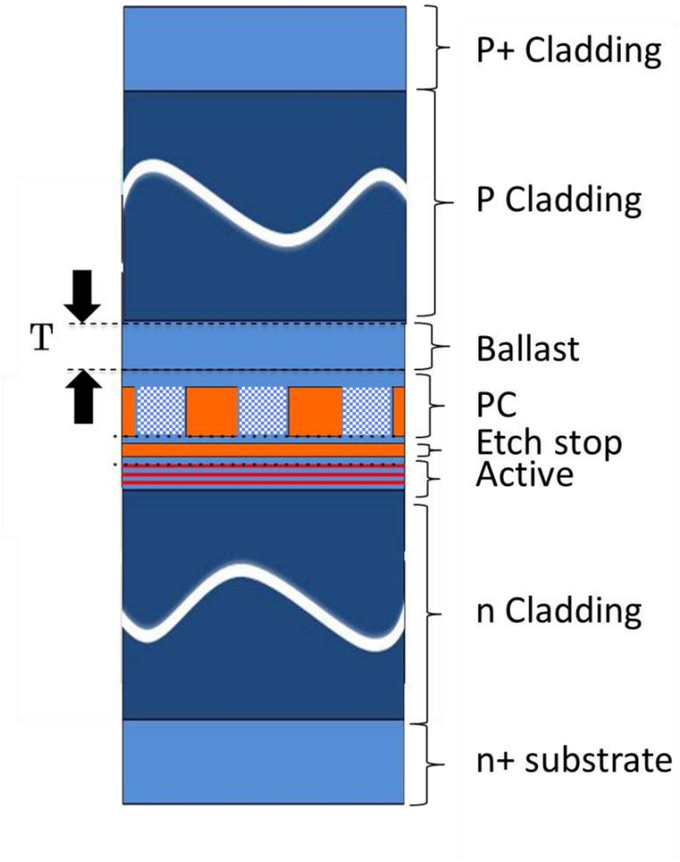

Figure 3.9 Photonic crystal laser structure incorporating a ballast layer

Figure 3.9 shows a ballast layer PCSEL structure where the structure consists (from bottom to top) a n-type cladding layer, a three quantum well active layer, an etch stop layer, the photonic crystal region, a p-doped ballast layer, a p-type cladding layer and finally a highly doped p-type layer.

Figure 3.10 shows the modelled normalised mode profile, device structure, and refractive index profile for a void containing PCSEL (dashed line) compared to an all-semiconductor PC (solid line) ballast layer PCSEL where the ballast layer thickness is 20nm. The all-semiconductor PCSEL again has more of the mode overlapping with the photonic crystal.

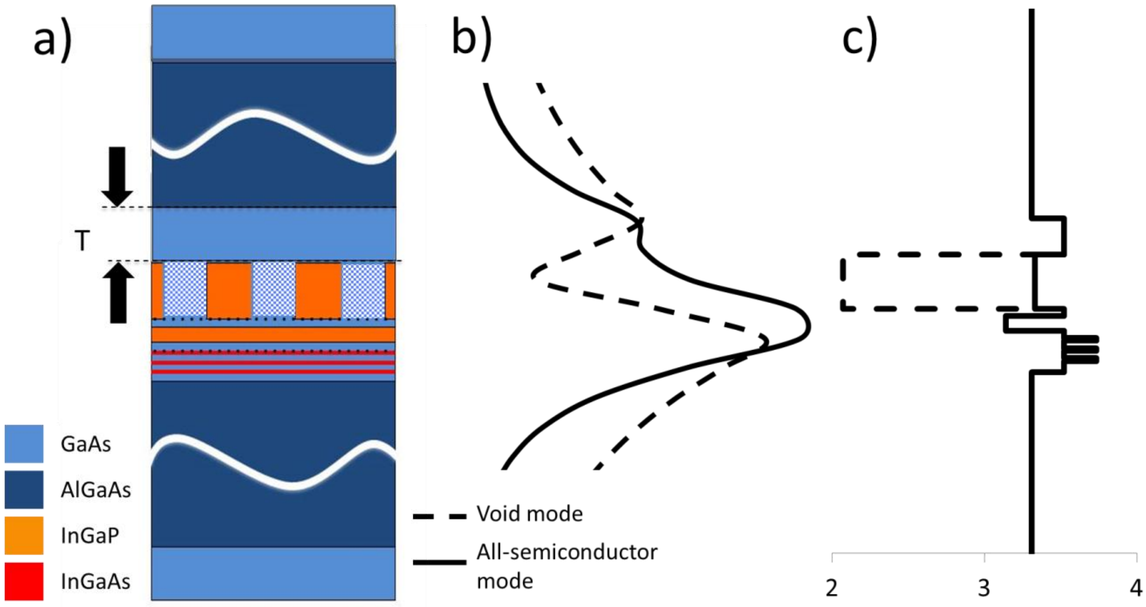

Figure 3.10 a) layer structure of a ballast PCSEL b) mode profile for a ballast layer all-semiconductor (solid line) and void containing PCSEL (dashed) and c) refractive index profile of the structure

Ballast Layer Thickness

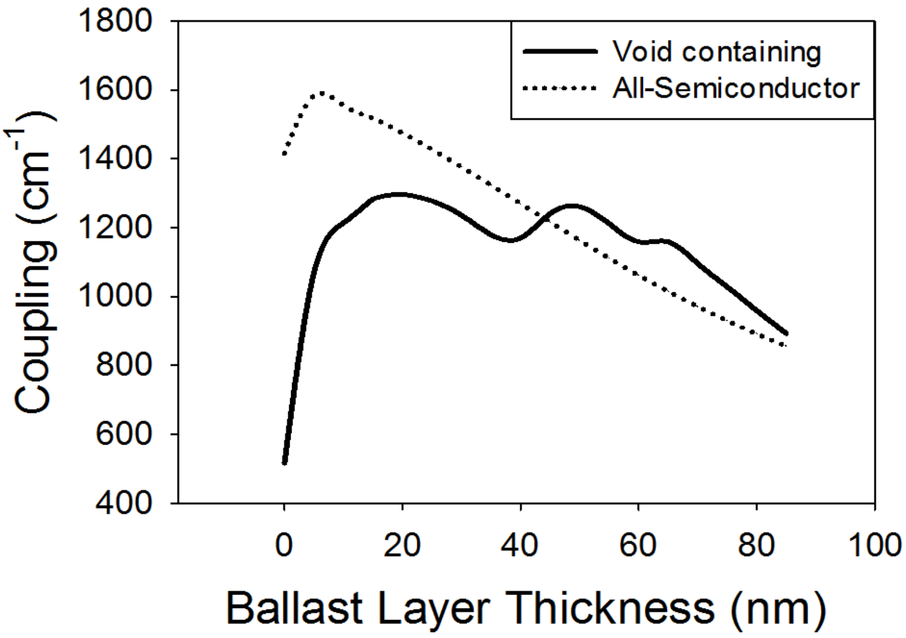

Figure 3.11 coupling variation of a Ballast layer PCSEL for void containing (dotted line) and all-semiconductor (solid line) PC regions, with ballast layer thickness considered from 0nm to 85nm

Figure 3.11 shows the in-plane coupling coefficient (K_3) for a ballast layer PCSEL where the thickness is increased from 0nm to 85nm. As the ballast layer thickness, T, increases the coupling for the all-semiconductor PCSEL initially increases and then monotonically decreases, while the void containing structure has peaks in coupling at 20nm and 50nm. The void containing PCSEL has a slightly higher coupling value for T>50nm, while all-semiconductor PCSEL has higher coupling value for T<50nm. By introducing the ballast layer into the structure the InGaP/void PCSEL has an increase in coupling from ~600cm^{-1} to ~1300cm^{-1} while the InGaP/GaAs PCSEL has an increase in coupling from ~1400cm^{-1} to ~ 1600cm^{-1}. This suggests that the mode peak has been pushed higher in the structure increasing the PC layer coupling coefficient.

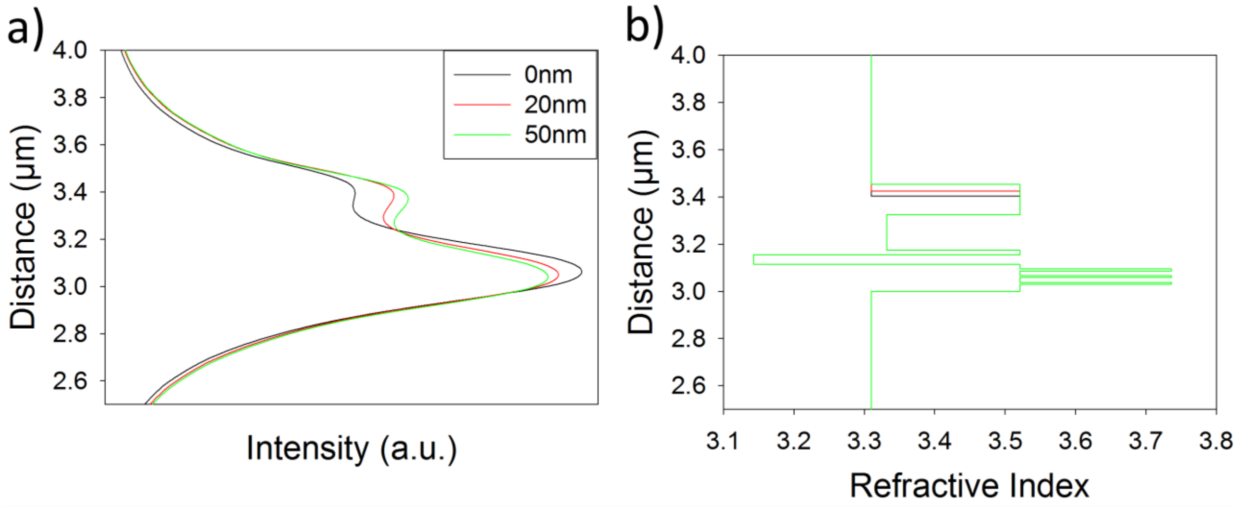

Figure 3.12 a) mode profile and b) refractive index variation of ballast layer all semiconductor PCSEL where the ballast layer is 0nm (black), 20nm (red) and 50nm (green)

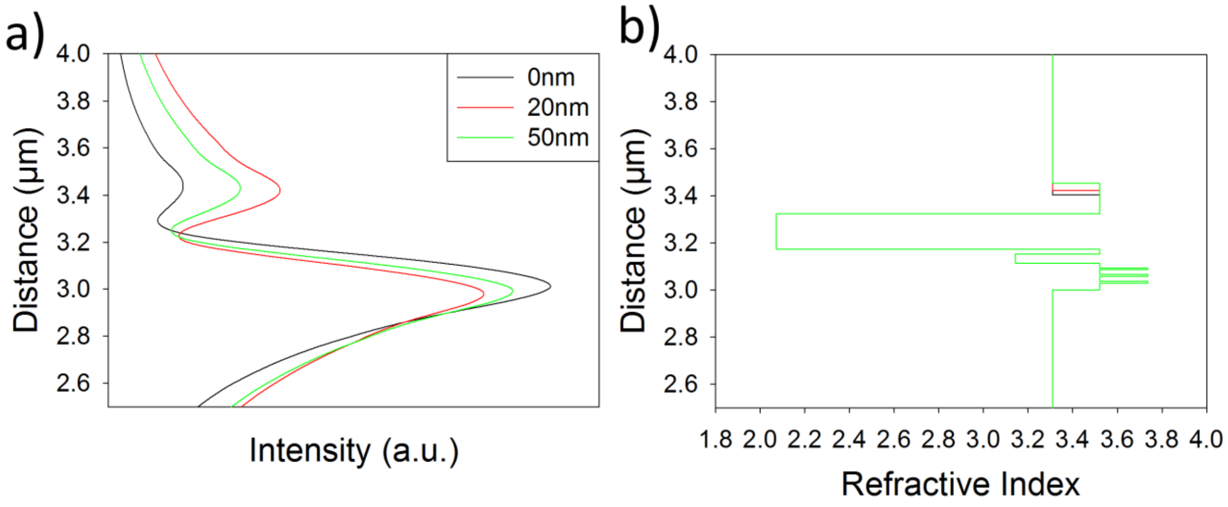

Figure 3.13 a) mode profile and b) refractive index variation of ballast layer all semiconductor PCSEL where the ballast layer is 0nm (black), 20nm (red) and 50nm (green)

Figure 3.12 and 3.13 show a) the modelled mode profile and b) refractive index profile of a void containing and all semiconductor ballast layer PCSEL, respectively. The ballast layer thickness is 0nm (black), 20nm (red) and 50nm (green). Each mode profile has a large peak overlapping the QW active layer and a second peak in the ballast layer. As the ballast layer thickness is increased from 0 to 20nm the percentage of the mode in the ballast layer increases.

Summary – Ballast Layer

This section considered a PCSEL structure with a ballast layer located above the PC region. The ballast layer was intended to counter the effect of the mode being distorted away from the void containing PC region due to its low refractive index. The ballast layer has been shown to increase PC coupling in both all-semiconductor and void containing structures. However, the coupling coefficient does not increase sufficiently to be greater than that of an all-semiconductor PCSEL with no ballast layer. The importance of this layer in void containing PCSEL design is highlighted. This will lead to possible trade-offs in p-doping of this layer with regard to reducing internal loss due to inter valance band absorption (IVBA), and electrical performance.

3.4 Double Decker PCSEL

The final structure considered in this section consists of two PC regions located above and below the active region, first proposed by Kurosaka *et, al.,* The intention with this structure is that by having 2 PC regions the coupling will be increased by virtue of there being more PC to overlap with the mode. The symmetry of the structure should also allow bound modes for void containing PCSELs to be realised and the high index contrast of void containing structures to be exploited.

Structure

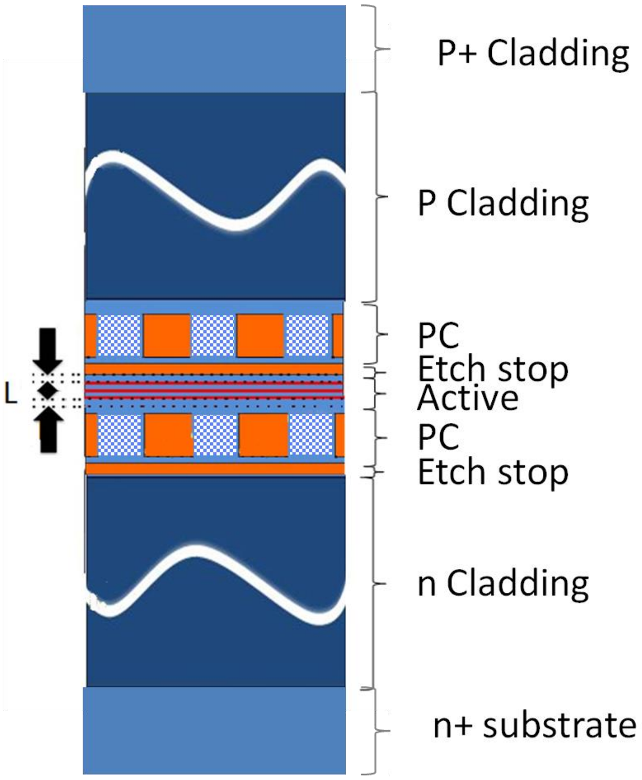

Figure 3.14 PCSEL structure incorporating a double PC above and below the active

Figure 3.14 shows a double decker PCSEL structure where the structure consists (from bottom to top) a n-type cladding layer, an etch stop layer, photonic crystal region, a three quantum well active layer, an etch stop layer, photonic crystal region, a p-type cladding layer and finally a highly doped p-type layer.

Cladding Aluminium Composition

Initially when the structure was considered (with 40% Al composition in the upper and lower cladding layers) the mode was unbound for the void containing PCSEL (similar to modes being unbound at low Al% in the basic structure), so the first challenge was confining the mode, which was accomplished by increasing cladding layer Al% in both layers.

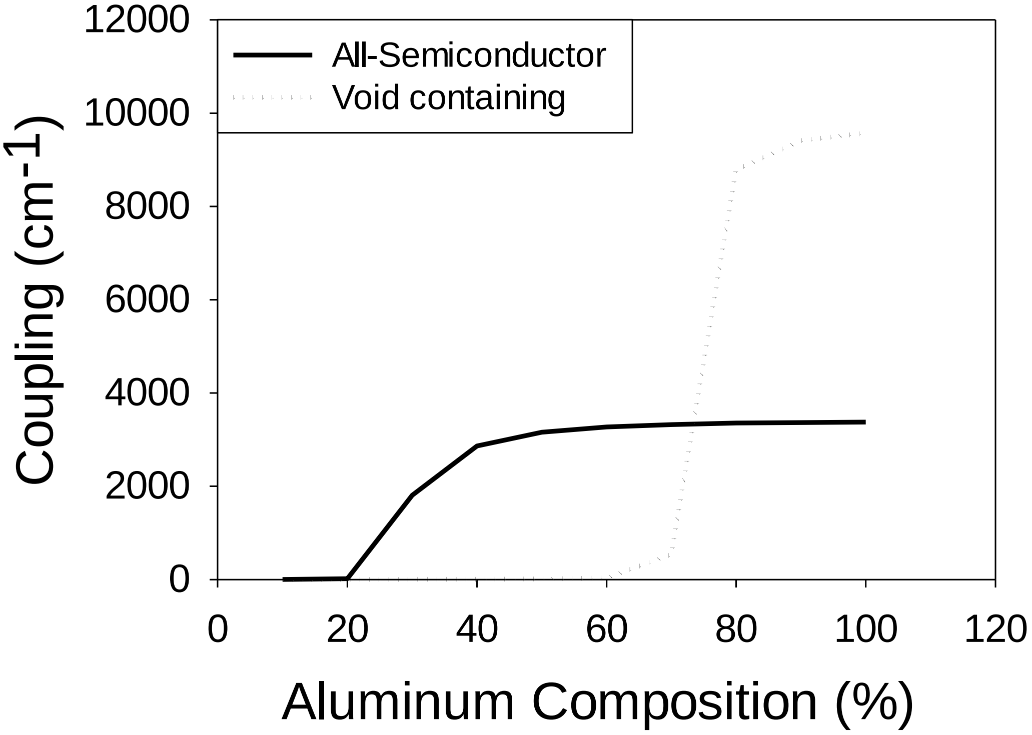

Figure 3.15 coupling values for double decker PCSEL showing void containing (dotted) and all-semiconductor (solid) PC regions for AlGaAs cladding Al composition of 0-100%

Figure 3.15 shows the coupling coefficient for a “double decker” PCSEL where the AlGaAs cladding Al composition in the upper *and* lower cladding is varied from 0-100%, areas where the coupling is ~0cm^{-1} represent values of Al where the mode is unbound. The all-semiconductor PCSEL has unbound modes at Al<20% but the void containing PCSEL mode is unbound for Al<70%.

In both cases the mode is unbound until the cladding layer refractive index is reduced sufficiently to give a bound mode. Coupling increases rapidly once a bound mode is obtained, but coupling reaches a maximal value shortly after. This is the first case I have considered where the void containing PCSEL has a higher coupling value than the all-semiconductor PCSEL, with the void containing PCSEL reaching K_3 ~ 9000cm^{-1}, the all-semiconductor

PCSEL only reaches K_3 ~ 3000cm^{-1}. In both cases, it is important to note, the maximum coupling achieved is higher than the maximum coupling in the other structures considered.

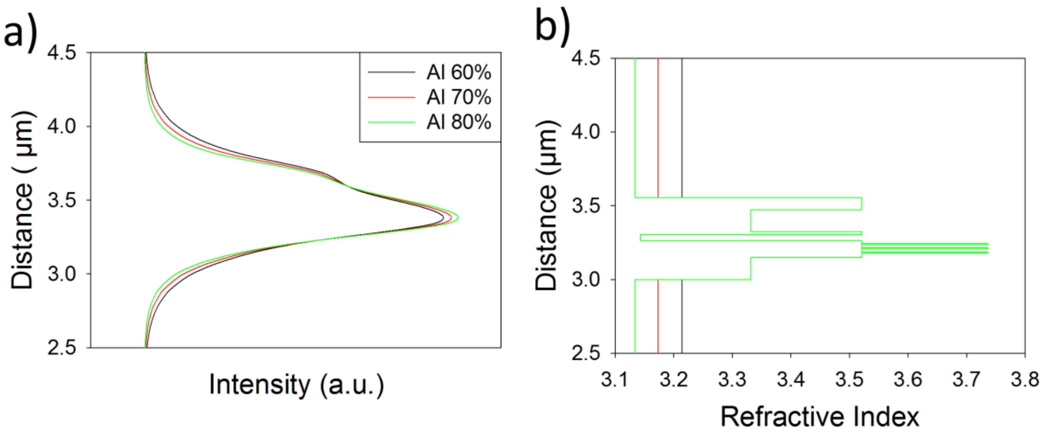

Figure 3.16 a) mode profile and b) refractive index variation of double decker all semiconductor PCSEL where the aluminium composition is 60% (black), 70% (red) and 80% (green)

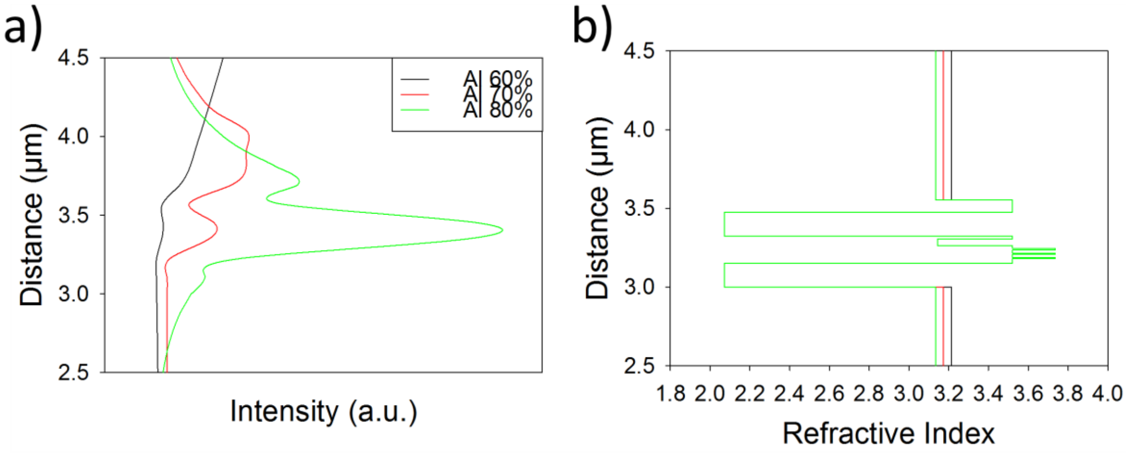

Figure 3.17 a) mode profile and b) refractive index variation of a double decker void PCSEL where the aluminium composition is 60% (black), 70% (red) and 80% (green)

Figures 3.16 and 3.17 show the mode profiles of an all semiconductor and void double decker PCSEL, respectively. The all semiconductor PCSEL has a bound mode and increasing the Al% slightly increases the mode confinement. The void containing mode is unbound at 60%

Al and bound at 70 and 80% with the mode having a higher overlap with the PC at 80% Al. In both cases the mode peak overlaps the active QW region and PC of the structure where the mode is bound the majority of the mode seems to be contained between the bottom of the lower PC and the top of the upper PC.

Separation Distance Variation

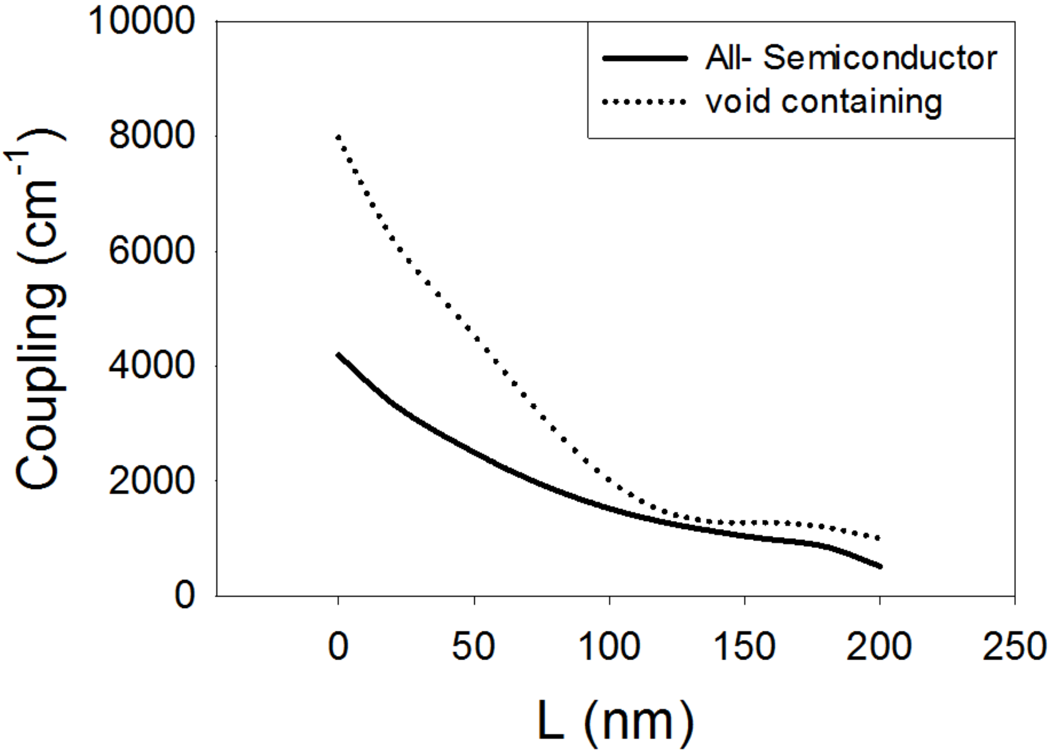

Figure 3.18 PC coupling for a double decker PCSEL for all-semiconductor (solid line) and void containing (dotted line) PC regions

Figure 3.18 shows the PC coupling for a double decker PCSEL for a separation distance from 0 to 200nm. In both cases the coupling decreases as the separation distance increases. The void containing PCSEL coupling is higher for the full range.

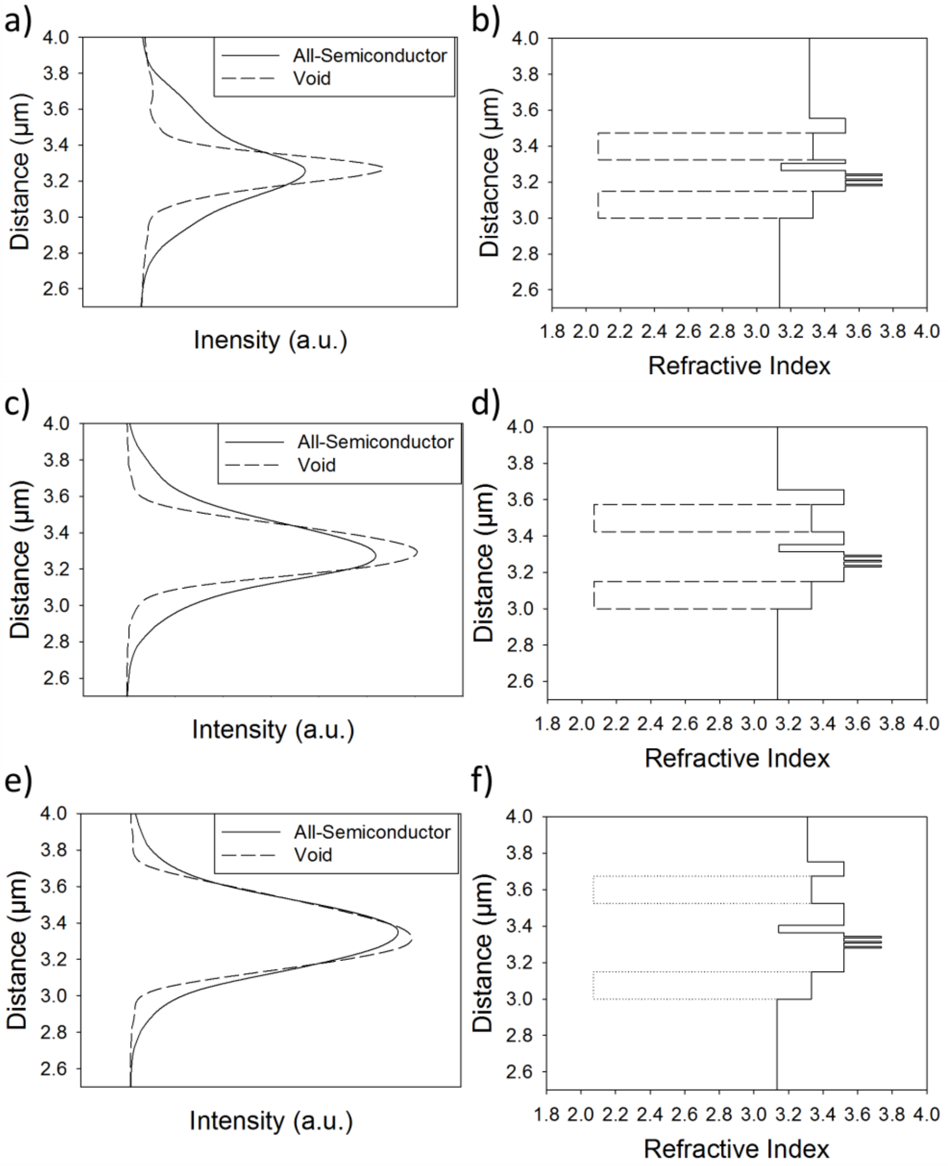

Figure 3.19 a), c) and e) show the mode profile of an all semiconductor (solid line) and void (dashed line) double decker structure for separation L 0nm, 100nm and 200nm, respectively. b), d) and f) show the refractive index profiles.

Figure 3.19 shows the normalised mode profiles of all semiconductor (solid line) and void (dashed line) double decker PCSEL where the separation is a) 0nm, b) 100nm and c) 200nm, respectively. In all cases the peak in the mode profile sits between the 2 PC layers, overlapping the QW active region. As the separation increases the mode widens and the overlap with the PC regions decreases.

Notwithstanding issues with regard to trade-offs in p-doping in the structure, as discussed previously, a double decker structure would pose significant fabrication challenges to manufacture. The initial problems may be in the production of the PCs themselves. As previously discussed there are two main production methods for PCSELs, wafer fusion and regrowth. It would be possible to utilise either method to produce a double decker PCSEL but both may have difficulties.

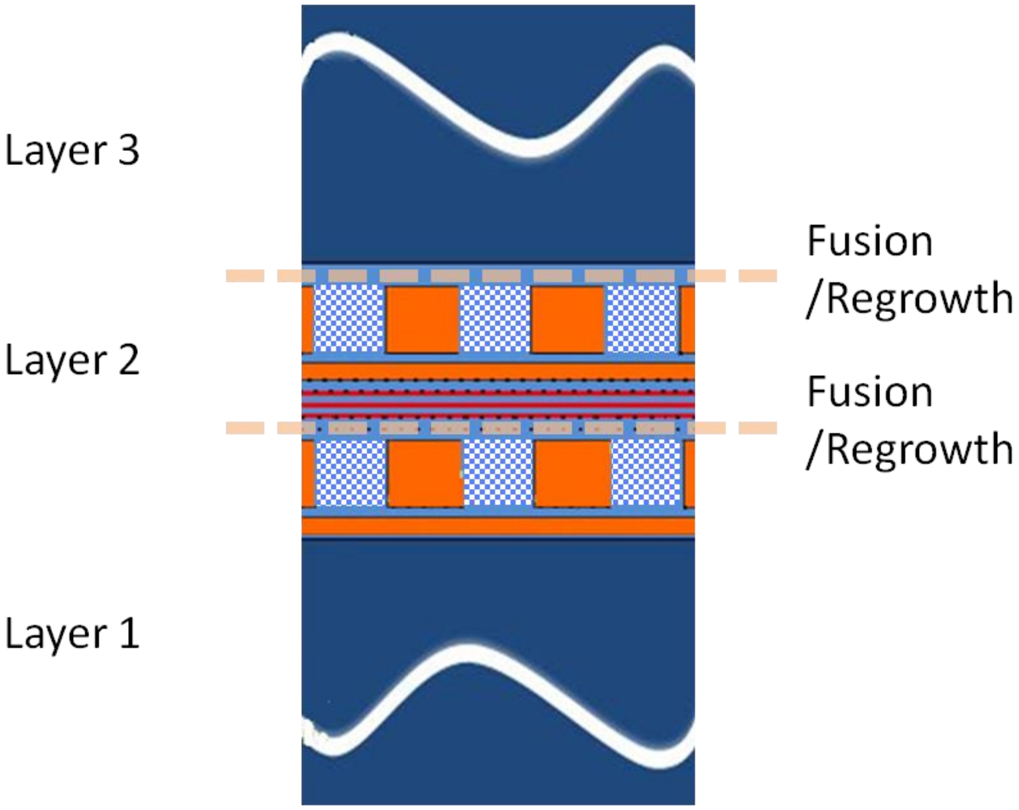

Figure 3.20 Double decker PCSEL structure indicating layers which need to be grown and location of fusion/regrowth interfaces

Figure 3.20 shows a double decker structure, indicating where the wafer fusion or epitaxial regrowth would be required to fabricate the double decker structure. Fabricating a double decker PCSEL with wafer fusion would leave a fusion interfaces within nm of the active region, which would result in defect states within the structure which may degrade device performance and reliability [12]. Additionally layers 1 and 2 would need to be perfectly aligned which would require nm precision over the 2-6 inch wafer, such technologies do not presently exist (i.e. wafer fusion with nm scale registration and alignment).

Fabricating a double decker PCSEL by regrowth would instead require multiple regrowths within nm of the active region, multiple regrowths are possible however planarization at the boundary between layer 1 and layer 2 would need to be ensured for growth of the quantum wells. All-semiconductor PCSEL growth has shown a non planar surface above the PC layer [13] and this would have to be overcome for growth of a double decker structure. Alignment would be less of an issue for regrowth because a feature could be etched into layer 1 to act as an alignment marker during the patterning of the PC layers. Nevertheless, "perfect" alignment would be a major technical challenge.

The high Al % required to get a bound mode in the void containing PCSEL poses further problems which would need to be overcome. The nature of AlGaAs means cladding of such high Al% would have poor electrical characteristics. The all-semiconductor PCSEL would only require an Al composition of 40% which is ideal for AlGaAs electrical characteristics.

Summary – Double Decker

This section considers a PCSEL structure with multiple PC layers located above and below the active region. The double decker structure was intended to increase the PC coupling within the structure by virtue of having a larger volume of PC for the mode to couple to and by increasing the symmetry of the refractive index throughout the structure. The double decker has been shown to give higher coupling values for both all-semiconductor and void containing PCSEL and has shown a higher value of coupling for void containing PCSELs than for all-semiconductor PCSELs. However the void containing PCSELs only give a bound mode for high cladding Al composition which is known to give poor electrical properties. Further gains in coupling value may be possible by increasing the volume of the PC layer. Fabrication issues have been considered and a double decker structure (whether void containing or all-semiconductor) would have significant processing issues to overcome, whichever fabrication route is used.

Summary – GaAs 980nm Structures

This chapter has considered 980nm structures based on GaAs. A structure from Williams *et, al.,* was modelled and it was demonstrated that for a void containing structure the mode profile was distorted away from the PC layer due to the low a refractive index given by a weighted average of the refractive index of its constituent parts of the PC layer. Attempts were made to increase the mode overlap for the void containing PCSEL in order to give a high coupling coefficient. This was achieved by engineering the structure to have a reduced refractive index of the lower cladding layer and including an additional ballast layer in the structure. All these modelled structures give a higher coupling coefficient for the all-semiconductor PCSEL as compared to the void containing case. The double decker structure is the only structure in which the void containing PCSEL has a higher coupling coefficient than the all-semiconductor PCSEL. Potential issues with the fabrication of the double decker structure make this an impractical device at present.

This chapter has focused on designing the waveguide to give high PC coupling coefficient, to give high power per unit area. It is worth considering however, that this does not take into account the design of the PC itself. As described in chapter 1 there has been much work on optimising design of the PC. This has included considerations of lattice geometry [14-16], side wall verticality [17] and atom shape [18]. It is the design of the PC that ultimately determines the properties of a PCSEL laser PC design which has been considered in chapter 2, a strategy which appears to be employed in the design of void containing PCSELs is to reduce the feature size in the PC to increase the average refractive index of the PC layer. In all modelling carried out I have maintained a 50% fill as shown to be ideal in Chapter 2.

3.5 Material and Wavelength Considerations

As discussed in chapter one, PCSELs offer some advantages over Fabry Pérot (FP), distributed feedback (DFB) and vertical cavity surface emitting lasers (VCSEL) lasers. They promise high brightness [19, 20], power scaling, low divergence [19], beam steering [21, 22] and circular beams [23]. Many of these properties are desirable in a wide range of applications, for example low divergent circular beams are desirable for working towards lens-less laser modules. However the various applications of semiconductor lasers normally require specific wavelengths. Short wavelengths are desirable for many applications including 405nm for optical data storage [24], optical gyroscopes [25], laser lighting, and biomedical applications [26]. 1.3µm and 1.55 µm lasers are desirable for optical communications because of the dispersion and absorption properties of glass fibre [27]. Infra-red (IR) quantum cascade lasers (QCLs) are desirable for a range of applications including target illumination, counter measures, and for gas sensing [28].

This section considers PCSEL designs for different material systems and wavelengths. The wavelengths considered are 405nm[29], 1.3µm[30] and 10µm. each structure is modelled as a 1D waveguide where the PC region is considered as a layer with a refractive index determined by an average of the PC constituents. As before, the 1D 2nd order coupling coefficient is calculated for separation thickness variation.

In all cases, regardless of the PC fill factor used in the literature (if a PCSEL has been realised) a 50% fill factor is considered here. This is an optimal value as shown in chapter 2. This allows a like-for-like comparison of all-semiconductor and void containing structures, as performed for GaAs based structures in section 3.2.

GaN/InGaN/AlGaN 405nm Structure

GaN is the material of choice for short wavelength lasers ~400nm. This has been primarily targeted for applications in optical data storage, displays, and biomedical applications [24,26]. Incorporating a photonic crystal within a GaN laser structure would allow the aforementioned advantages of PCSELs to be realised at these wavelengths. A ~400nm void containing PCEL has been realised by Kawashima *et, al.*, [29].

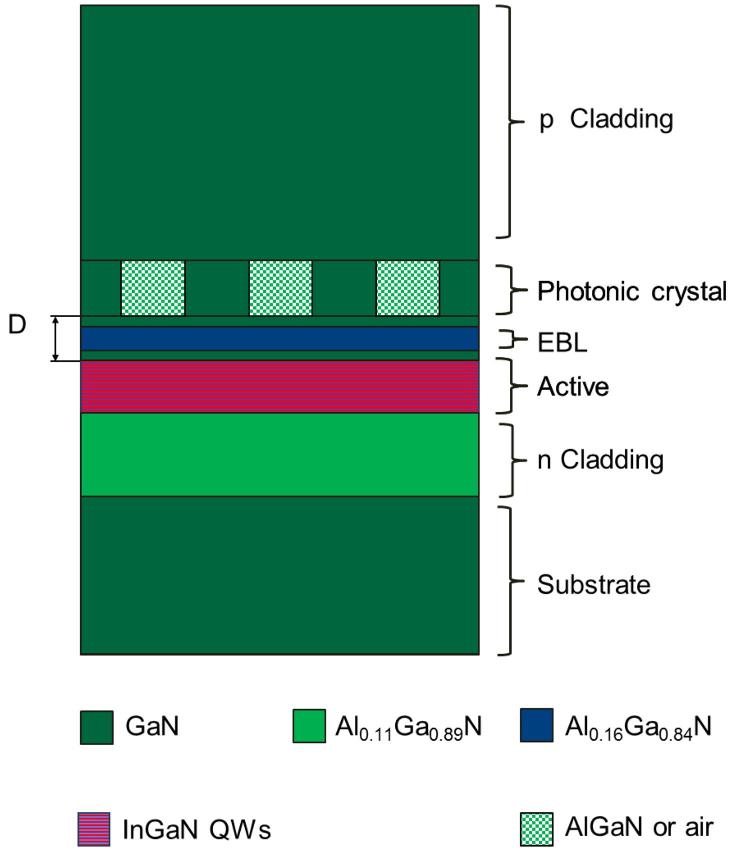

Figure 3.21 Layer structure of a 405nm wavelength PCSLE based on GaN

Figure 3.21 shows the structure of a ~400nm PCSEL design after the layer sequence described in Kawashima *et al.*, [29]. The structure consists of (from bottom to top) n-type $Al_{0.11}Ga_{0.89}N$ cladding layer, multiple quantum wells, an 80-nm-thick undoped GaN layer, a 20-nm-thick p-$A_{0.16}Ga_{0.84}N$ electron-blocking layer, a 115-nm-thick p-GaN layer, a PC layer, a 40-nm-thick p-GaN layer and a 115-nm-thick p+-GaN contact layer. The MQWs consist of three 2.5-nm-thick $In_{0.09}Ga_{0.91}N$ well layers and 7.5-nm-thick GaN barrier layers. The PC region is 220nm thick and consists of GaN/$Al_{0.11}Ga_{0.89}N$ or GaN/air with a 50% fill factor.

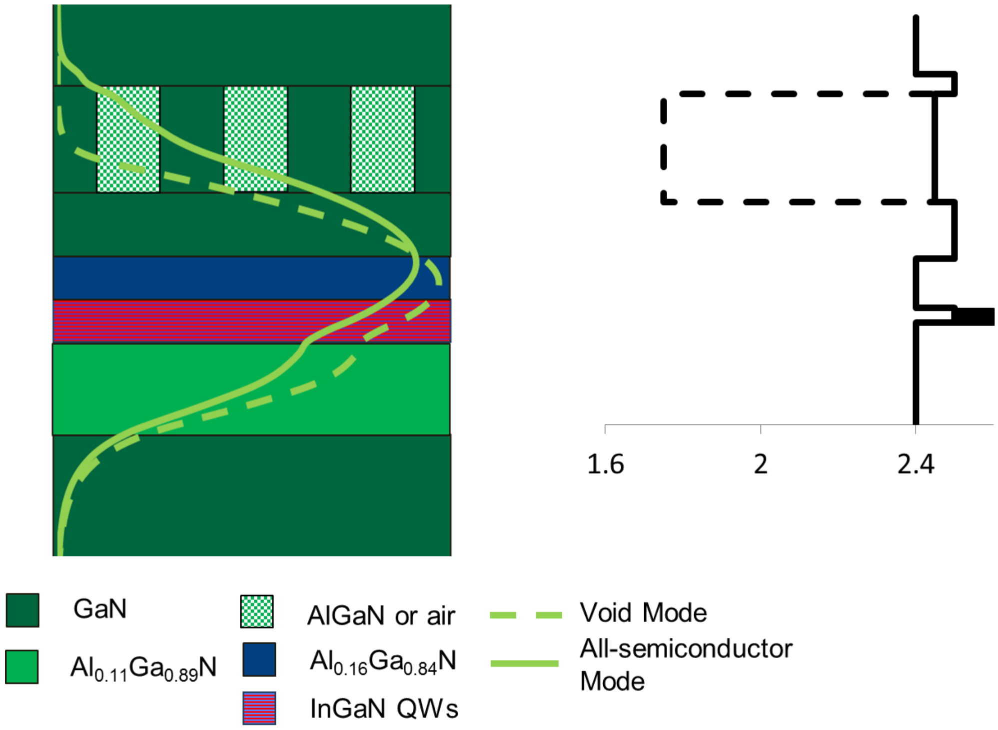

Figure 3.22 mode profile overlaid on PCSEL structure for void (Dashed line) and all-semiconductor (solid line) GaN 405nm PCSEL over laid on the device structure with the refractive index profile shown on the right

Figure 3.22 shows a schematic of the ~400nm GaN PCSEL where the mode for a void containing PC (dashed line) layer and an all-semiconductor PC (solid lime) are shown overlaid on the device structure. The mode of the all-semiconductor PCSEL has significantly higher overlap with the PC layer than the void containing PCSEL, this is again due to the low weighted average of the refractive index of its constituent parts of the void containing PC pushing the mode away. Refractive indices are taken from Laws *et, al.*, [31]

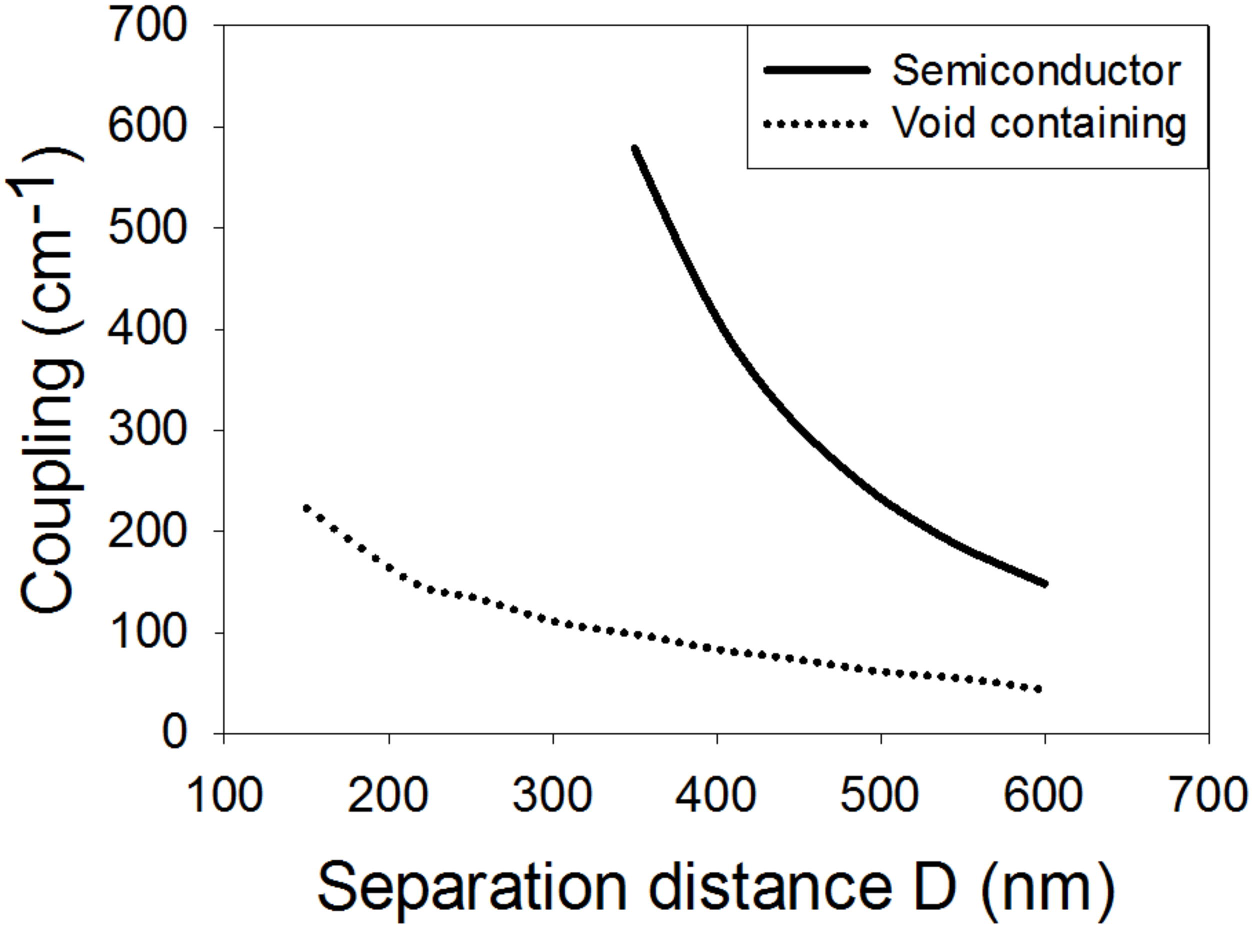

Figure 3.23 Coupling variation for separation width from 150 to 600nm for GaN based 405nm PCSEL showing all-semiconductor (solid) and void containing (dashed) containing structures

Figure 3.23 shows coupling as separation width increases from 150nm to 600nm for all-semiconductor (solid) and void containing (dotted) PCSELs for a GaN based 405nm PCSEL, from Kawashima *et al.*, [29]. There are no coupling values for the all-semiconductor structure for separation distances less than 350nm because below this value the mode is unbound. In both cases the coupling decreases as the separation thickness D increases, and as expected the coupling tends to zero for large values of D. The all-semiconductor PCSEL has a higher K_3 for the entire range considered.

InP/InGaAsP 1.3μm Structure

The absorption and dispersion characteristics of optical fibre gives two wavelength widows for optical communications, these are 1.55μm and 1.3μm [27]. Incorporating a photonic crystal within a InP laser structure would allow the advantages of PCSELs for optical communication applications, in particular low divergent circular beams for lens-less optical communications.

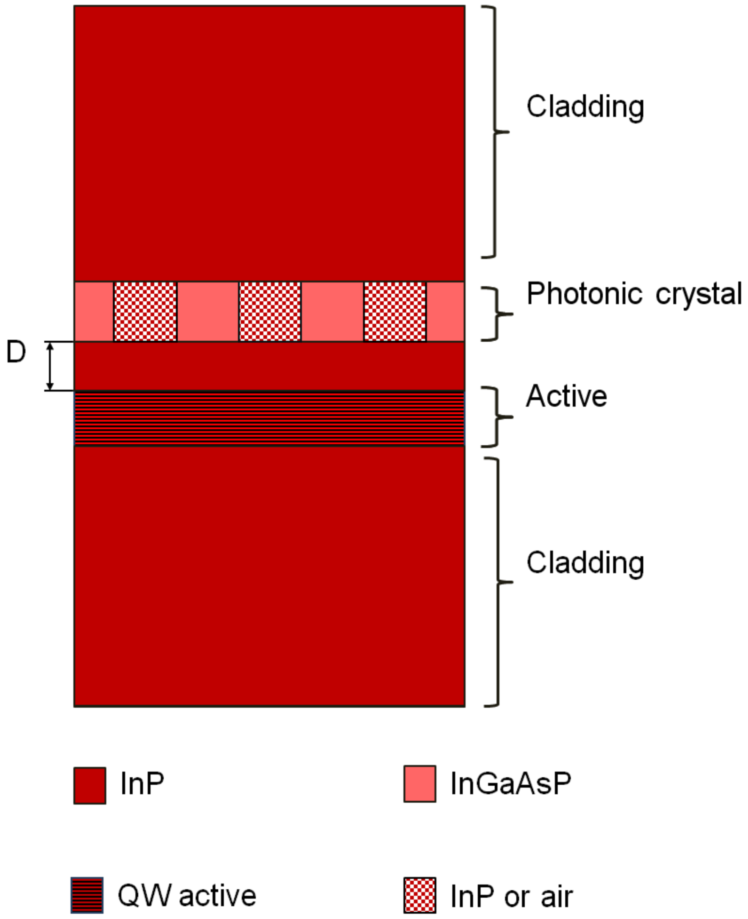

Figure 3.24 Layer structure of a 1.3μm wavelength PCSEL based on InP

Figure 2.24 shows the structure of a 1.3µm PCSEL which is based on a structure from Imada *et al.*, [31] consisting (from bottom to top): InP substrate, 1.4µm cladding layer, 240nm QW active layer consisting of seven 7nm InGaAsP quantum wells with 15nm InP barriers, a photonic crystal consisting of either InGaAsP /InP or of InGaAsP/air with a 50% fill factor and a 1.4µm InP cladding layer.

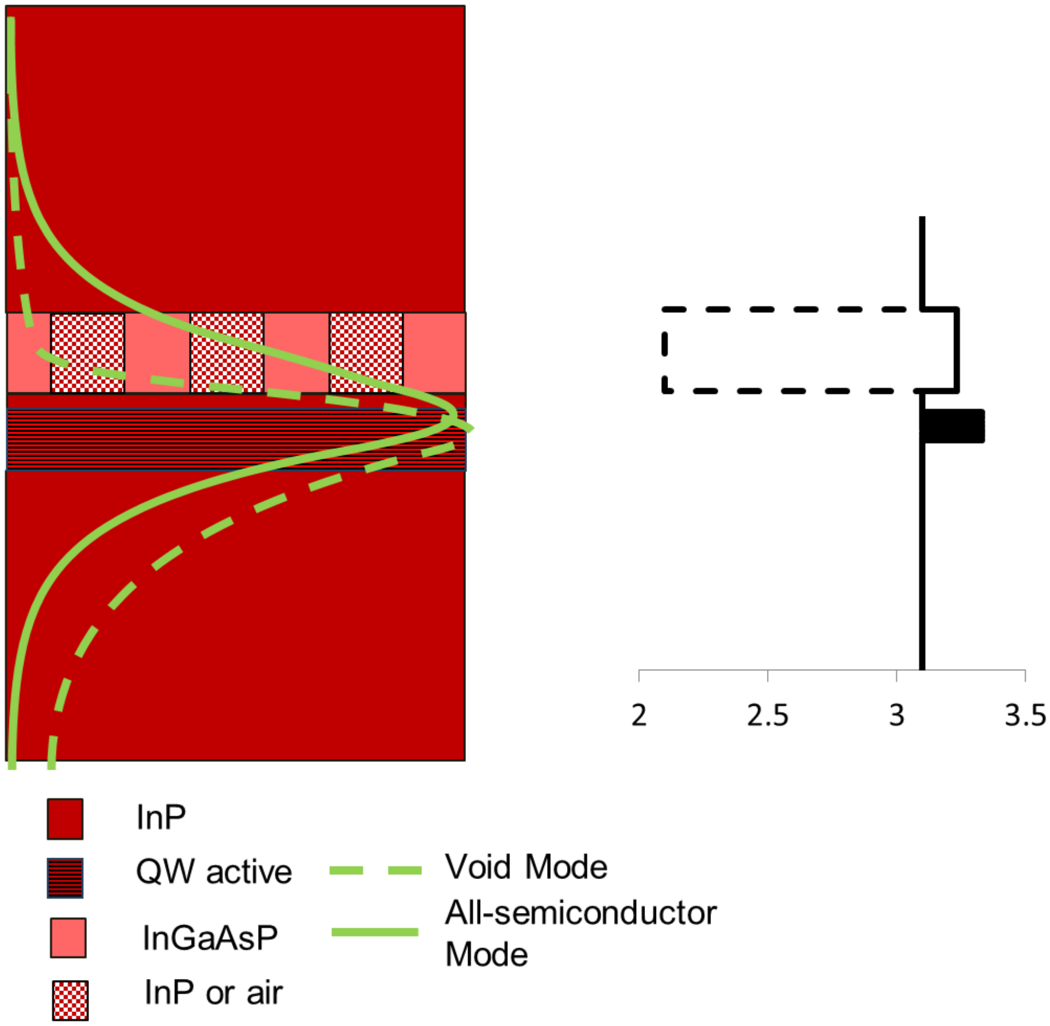

Figure 3.25 mode profile overlaid on PCSEL structure for void containing (dashed line) and all-semiconductor (solid line) 1300nm PCSEL over laid on the device structure with the refractive index profile shown on the right

Figure 3.25 shows the modelled mode profile of a 1.3µm PCSEL layer sequence from Imada *et, al.*, where the mode for a void containing PCSEL (dashed line) layer and an all-semiconductor PC (solid lime) are shown overlaid on the device structure. As observed in GaAs and GaN devices the mode of the all-semiconductor PCSEL has significantly higher overlap with the PC layer than the void containing PCSEL.

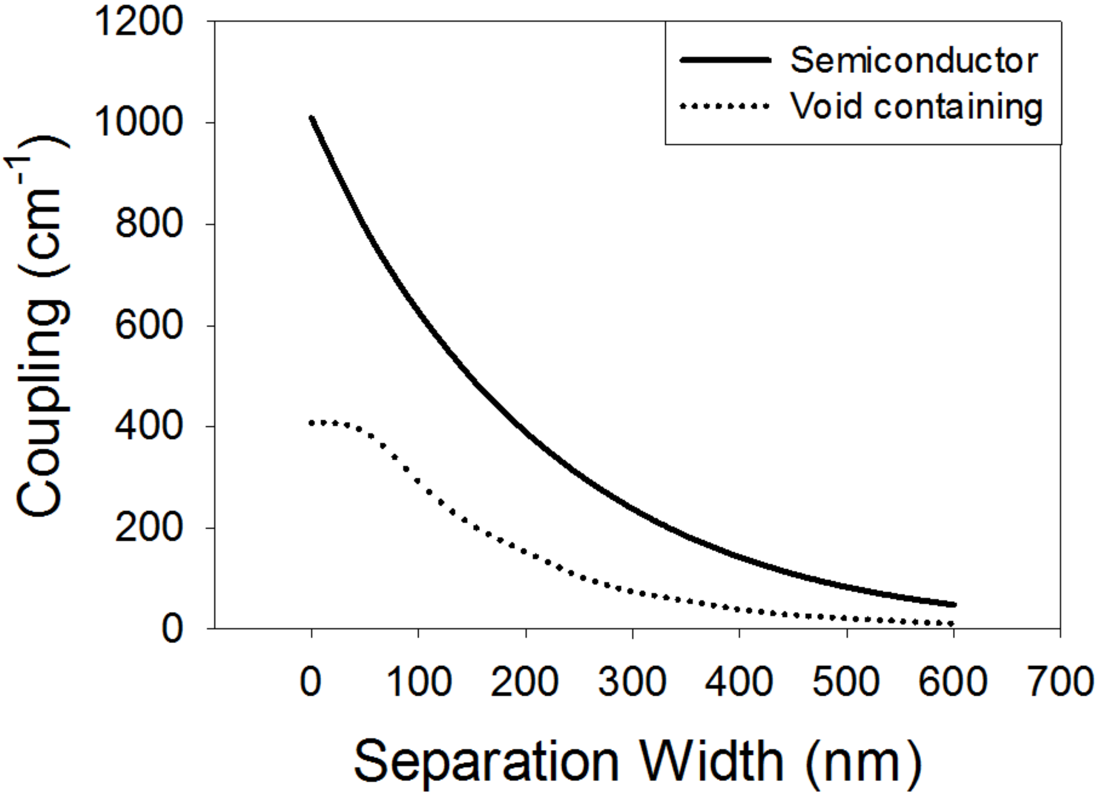

Figure 3.26 Coupling variation for separation width from 0 to 600nm for GaAs based 1.3µm PCSEL showing all-semiconductor (solid) and void containing (dotted) containing structures

Figure 3.26 shows the modelled photonic crystal coupling of a 1.3µm PCSEL where the separation between the photonic crystal and the active region is varied from 0 to 600nm, for all-semiconductor (solid line) and void containing (dotted line) photonic crystals. The all-semiconductor PCSEL has a higher coupling value for the whole range considered with the maximum in both cases being when the separation distance is small. The peak in coupling for the all-semiconductor PCSEL is 1000 cm^{-1} and the peak in coupling for the void containing structure is 400cm^{-1}. As expected, for large values of separation the coupling tends to zero.

InP/AlInAs/InGaAs 10µm Structure

InP based quantum cascade lasers (QCLs) have shown promise in a range of applications including military applications such as target illumination and industrial applications such as gas sensing [28].

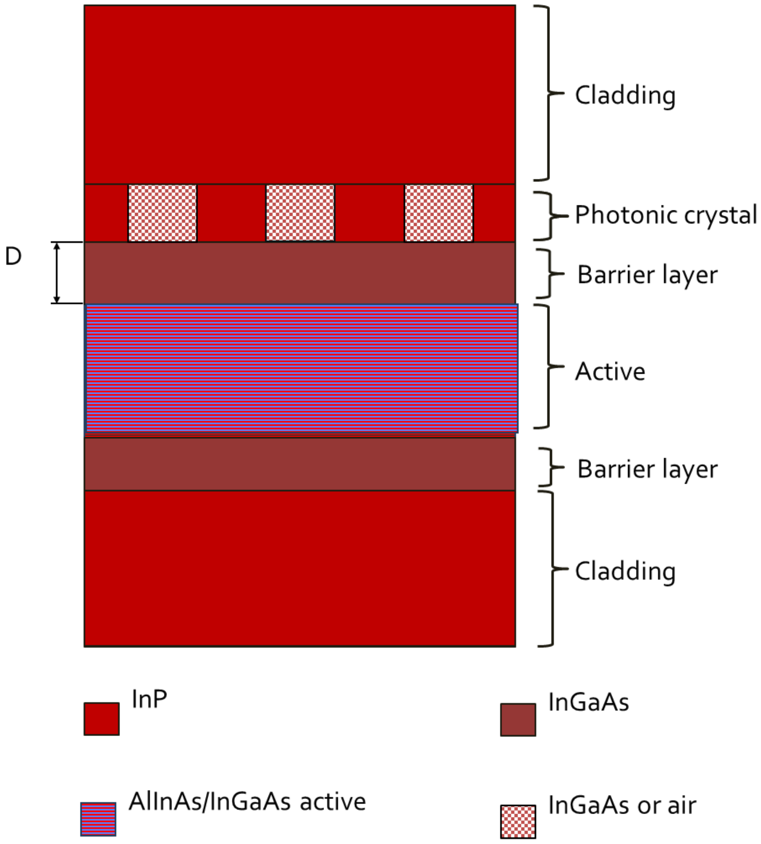

Figure 3.27 Layer structure of a 10µm wavelength quantum cascade PCSEL based on InP

Figure 3.27 shows a 10µm quantum cascade PCSEL. Based on edge emitting laser work by K. Kennedy[32]. The structure consists of (from bottom to top): 2.5µm InP cladding layer, 270nm InGaAs barrier layer, active region consisting of 35-stage region with the nominal layer structure of (thicknesses in Angstroms); **35** / 23 / **8** / 66 / **9** / 64/ **9** / 58 / **20** / 40 / **12** / 40 / **12** / 40 / **13** / 39 / **17** / 38 / **21** / 35 / **22** / 35 where bold refers to InAlAs and normal type refers to InGaAs, a photonic crystal region which consists of either InP/InGaAs or InP/air and has a 50% fill factor, and a 3.5µm InP upper cladding layer.

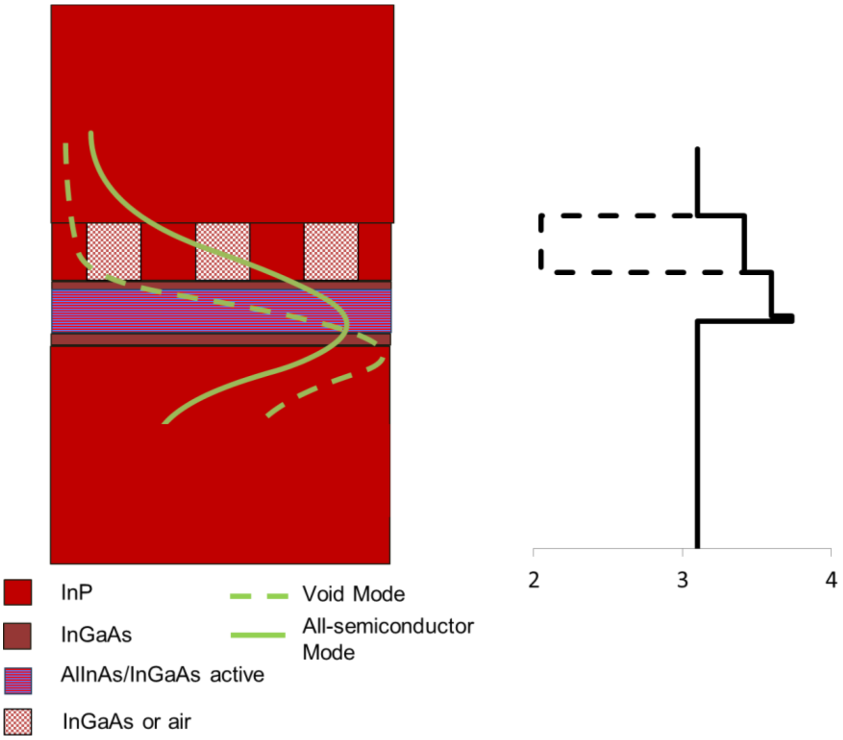

Figure 3.28 mode profile overlaid on PCSEL structure for void containing (Dashed line) and all-semiconductor (solid line) InP 10µm PCSEL over laid on the device structure with the refractive index profile shown on the right

Figure 3.28 shows the modelled mode profile of a 10µm InP QCL PCSEL where the mode for a void containing PC (dashed line) layer and an all-semiconductor PC (solid line) are shown overlaid on the device structure. Refractive indices are taken from Chen *et,al.,* [33]. As observed in all previous cases, The mode of the all-semiconductor PCSEL has significantly higher overlap with the PC layer than the void containing PCSEL.

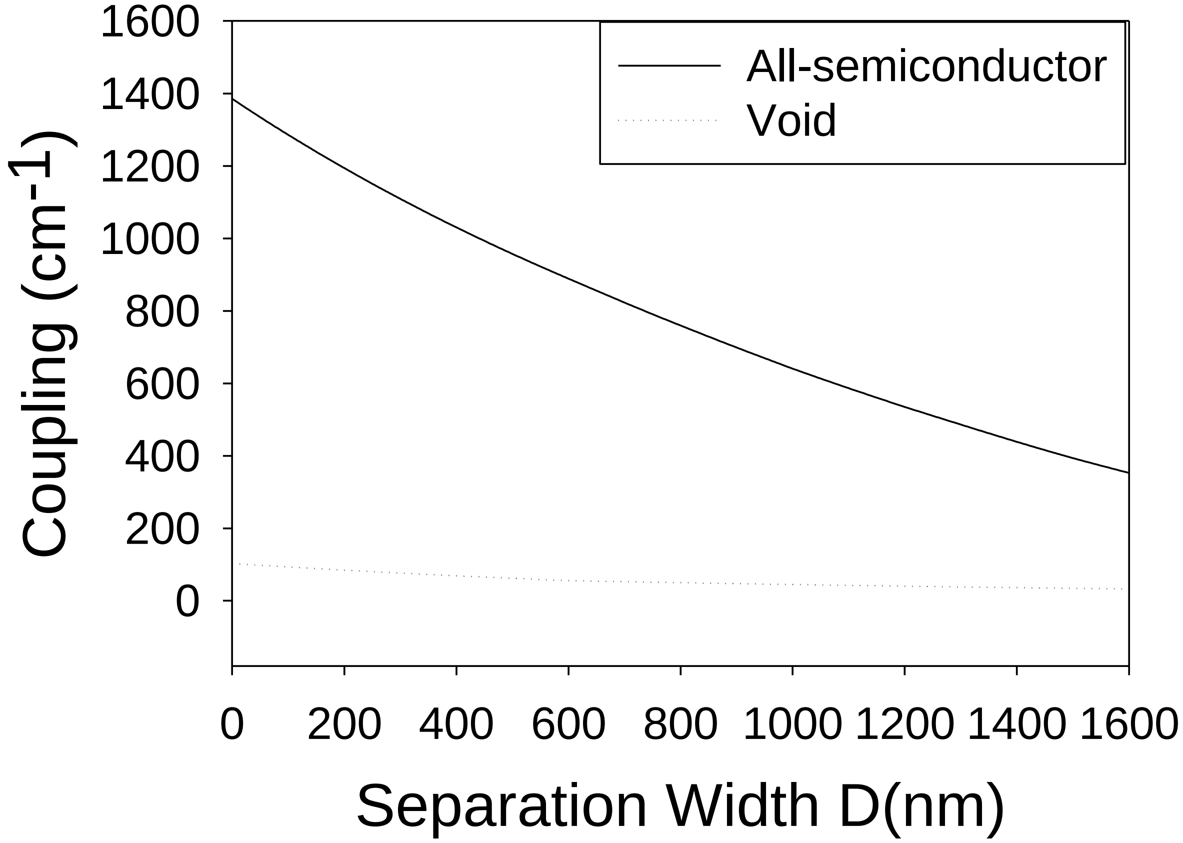

Figure 3.29 Coupling variation for separation width from 0 to 1600nm for InP based 10μm QCL showing all-semiconductor (solid) and void containing (dotted) structures.

Figure 3.29 shows the photonic crystal coupling of a 10μm PCSEL where the separation between the photonic crystal and the active region is varied from 0 to 1600nm, for all-semiconductor (solid line) and void containing (dotted line) photonic crystal. The all-semiconductor PCSEL has a higher coupling value for the whole range considered with the maximum in both cases being when the separation distance is small.

Summary – Material and Wavelength Considerations

In this section three PCSEL structures with emission spanning the UV to mid-IR (400nm, 1300nm and 10µm) have been considered. To a first approximation the device design is an existing edge emitting laser structure, with a PC layer in the upper waveguide cladding. All three structures have been modelled as a 1D waveguide and PC coupling coefficients have been calculated. In each case the all-semiconductor PCSEL had higher coupling than the void containing PCSEL. This highlight that it should be possible to obtain relatively high values of coupling, by including an all-semiconductor PC layer above the active region, tried and trusted edge emitting laser structures. This is however, not the case for void containing PCSELs as additional structural modification may be required to gain high coupling coefficients, as described previously for GaAs based PCSELs in section 3.3/3.4.

It is worth noting here that each of the material systems considered will have their own limitations and issues to overcome and the key loss mechanisms will be different. The 400nm GaN devices will require a PC period of 200nm and an atom radius of 50nm, such a small feature size will be difficult to fabricate and the overgrowth will have to be slow to avoid voids in the PC layer. At this time GaN growth has high defect density with defects causing carriers to recombine non-radiatively reducing device performance. The device operating at 10µm would have fabrication advantages, because the required PC period is ~3µm with a 1.2nm atom radius, this feature size could be fabricated with standard photolithography and fabrication would therefore be quick and cheap. The major loss mechanisms for QCLs is typically non-radiative phonon interactions, for this reason the device may be limited to operating at cold temperatures.

3.6 Conclusions

In this chapter PCSEL structures have been considered as a one dimensional waveguide where the PC region is considered as a layer with refractive index determined by the average of the PC constituents. Initially a basic PCSEL structure is considered from Williams *et al.,* [1-3] and it is found that that all-semiconductor PCSEL has a higher value of PC coupling despite having a much lower difference in refractive index (Δn). The lower coupling in the void containing PCSEL is attributed to the low weighted average of the refractive index of the PC layer, pushing the mode away from the PC region and giving a very low mode overlap with the PC. To address this problem other structures were considered. Firstly, a ballast layer is included above the active region to draw the mode back towards the PC region.

Secondly a structure is considered that has two PC regions (located above and below the active region) aimed at increasing coupling by virtue of there being more PC for the mode to couple to and creating symmetry in the waveguide. The ballast layer improves the coupling in the void containing PCSEL, although the increase is more significant in the void containing structure. The importance of such ballast layer in void containing PCSEL design is highlighted. The double decker PCSEL structure gives the highest coupling values of the structures considered, and is the only structure to give higher coupling for void containing PCSELs. Significant issues with growth and fabrication of the double decker PCSEL are considered and it may not be possible to produce such a device, at present. It is also worth noting that the double decker structure only has bound modes for $Al_xGa_{(1-x)}As$ cladding Al composition >70% and at such high Al compositions the electrical characteristics are undesirable.

Three PCSEL structures operating at a range of key laser wavelengths, manufactured in different material systems were considered. The PC coupling coefficient was shown to be higher in each all-semiconductor PC cases as compared to void containing case. This work, in conjunction with mode profile modelling of GaAs based structures shows that because an all-semiconductor PC layer can have a similar refractive index to the core of the waveguide, high coupling can be obtained without significant modification to the design of almost any edge-emitting laser structure. This is well known for realising DFB lasers, but the high aspect ratio and 3D nature of PCSEL structures poses new future challenges in epitaxial growth.

References

[1] D. Williams

"All-semiconductor photonic crystal surface emitting lasers at 980 nm through epitaxial regrowth"

PhD thesis, University of Sheffield, 58, 2014

[2] D. Williams, K. Groom, D. Childs, R. Taylor, S. Khamas, R. Hogg, B. Stevens, N. Ikeda, Y. Sugimoto

"Optimisation of coupling between photonic crystal and active elements in an epitaxially regrown GaAs based photonic crystal surface emitting laser"

Japanese journal of applied physics, **51**, 02BG05-1-3, February 2012

[3] D. Williams, K. Groom, D. Childs, R. Taylor, S. Khamas, R. Hogg, B. Stevens, N. Ikeda, Y. Sugimoto

"Epitaxially regrown GaAs-based photonic crystal surface emitting laser"

IEEE photonics technology letters, **24**, 11, 966-968, June 2012

[4] http://www.photond.com/products/fimmwave.htm

[5] C. Nguyen

"Analysis Methods for RF, Microwave, and Millimeter-Wave Planar Transmission Line Structures"

Wiley, 191, 2000

[6] R. Taylor, D. Williams, J. Orchard, D. Childs, S. Khamas and R. Hogg

"Band structure and waveguide modelling of epitaxially regrown photonic crystal surface emitting lasers"

Journal of Physics D, 46, 26, 264005, 2013

[7] R. K. Hunsperger

"Integrated optics theory and technology"

Springer, 17, 2009

[8] A. Yariv

"Optical Electronics in Modern Communications"

492, Fifth Edition, Oxford University Press (1997)

[9] B.J. Stevens

"Advanced Gallium Arsenide Based Lasers"

PhD Thesis, University of Sheffield, 2009

[10] M. Fukuda, Optical semiconductor devices, Wiley, 1999

[11] http://refractiveindex.info/legacy/?group=CRYSTALS&material=AlGaAs

[12] http://www.ioffe.ru/SVA/NSM/Semicond/AlGaAs/reference.html

[13] R. Taylor, D. Williams, D. Childs, B. Stevens, L. Shepherd, S. Khamas, K. Groom, R. Hogg, N. Ikeda, and Y. Sugimoto

“Photonic crystal surface emitting lasers based on epitaxial regrowth”

IEEE Journal of Selected Topics in Quantum Electronics, 19, 4, 4900407, July 2013

[14] K. Sakai, E. Miyai, T. Sakaguchi, D. Ohnishi, T. Okano and S. Noda.

“Lasing band-edge identi_cation for a surface-emitting photonic crystal laser”

IEEE Journal of Selected Areas of Communication., **23**, No. 7, 1335, 2005

[15] M. Plihal and A. A. Maradudin.

“Photonic band structure of two-dimensional systems: The triangular lattice”

Physics Review B, **44**, No. 16, 8565, 1991

[16] J. B. Nielsen, T. Sondergaard, S. E. Barkou, A. Bjarklev, J. Broeng and M. B. Nielsen.

“Two-dimensional Kagome structure, fundamental hexagonal photonic crystal configuration”

Electronics Letters, **35**, No. 20, 1736, 1999

[17] P Ivanov, Y-L D Ho, M J Cryan and J Rorison

“Modelling investigations of DBRs and cavities with photonic crystal holes for application in VCSELs”

Journal of Optics, **14**, 125103, 2012

[18] Y. Kurusaka, K. Sakai, E. Miyai and S. Noda

“Controling vertical optical confinement in two-dimensional surface-emitting photonic-crystal lasers by shape of air holes”

Optics express, **16**, 22, 18485, 2008

[19] M. Imada, S. Noda, A. Chutinan, T. Tokuda, M. Murata and G. Sasaki

”Coherent two-dimensional lasing action in surface-emitting laser with triangular-lattice photonic crystal structure”

Applied Physics Letters, **75**, 3, 316, 1999

[20] K. Hirose, Y. Liang, Y. Kurosaka, A. Watanabe, T. Sugiyama & S. Noda,

”Watt-class high-power, high-beam-quality photonic-crystal lasers”

Nature Photonics, **8**, 406-411, 2014

[21] Y. Kurosaka, S. Iwahashi, Y. Liang, K. Sakai, E. Miyai, W. Kunishi, D. Ohnishi & S. Noda

”On-chip beam-steering photonic-crystal lasers”

Nature Photonics, **4**, 447 – 450, 2010

[22] M. T. Johnson, D. F. Siriani, M. P. Tan, and K. D. Choquette

”Relative phase tuning of coupled defects in photonic crystal vertical-cavity surface-emitting lasers”

Journal of Selected Topics in Quantum Electronics, **19**, 1701006, 2013.

[23] E. Miyai, K. Sakai, T. Okano, W. Kunishi, D. Ohnishi and S. Noda,

“Photonics: Lasers producing tailored beams”

Nature, **441**, 946, 2006

[24] Y. Mitsuhashi

“Optical storage: science and technology”

Japanese Journal of Applied Physics, **37**, 2079-2083, 1997

[25] A. Pavlath

”Fiber-optic gyroscopes”

IEEE Lasers and Electro-Optics Society Annual Meeting Conference Proceedings, Volume 2, 237–238, 1994

[26] M. E. Brezinski

”Optical Coherence Tomography: Principles and Applications.”

Amsterdam, The Netherlands/Boston, MA: Academic Press, 2006

[27] Mitschke F., *Fiber Optics - Physics and Technology*, chapter 6, Springer, 2009

[28] P. Werlea, F. Slemra, K. Maurera, R. Kormannb, R. Mucke and B. Janker

“Near- and mid-infrared laser-optical sensors for gas analysis” optics and lasers in engineering **37**, 101-114, 2001

[29] S. Kawashima, T. Kawashima, Y. Nago, Y. Hori, H. Iwase, T. Uchida, K. Hoshino, A. Numata and M. Uchida

”GaN-based surface-emitting laser with two-dimensional photonic crystal acting as distributed-feedback grating and optical cladding”

Applied Physics Letters, **97,** 251112, 2010

[30] M. Imada, S. Noda, H. Kobayashi, and G. Sasaki

“Characterization of a Distributed Feedback Laser with Air/Semiconductor Gratings Embedded by the Wafer Fusion Technique”

IEEE journal of quantum electronics, **35**, 9, 1277-1283, 1999

[31] G. Laws, E. Larkins, I. Harrison, C. Molloy, and D. Somerford,

“Improved refractive index formulas for the AlxGa1−xN and InyGa1−yN Alloys”

Journal of Applied Physics, **89**, 1108, 2001

[32] K. Kennedy, D. G. Revin, A. B. Krysa, K. M. Groom, L. R. Wilson, J. W. Cockburn and R. A. Hogg

”Fabrication and Characterization of InP-Based Quantum Cascade Distributed Feedback Lasers with Inductively Coupled Plasma Etched Lateral Gratings”

Japanese Journal of Applied Physics, **46**, 2424, 2007

[33] A. Li, J. Chen, Q. Yang, Y. Zhang, C. Lin,

“The effect of dispersion of the refractive index on the performance of mid-infrared quantum cascade lasers”

Journal of Crystal Growth, 227–228, 2001

4. Coupled Array

Williams *et, al,* demonstrated lasing for the first all-semiconductor PCSELs operating at 980nm based on GaAs epitaxial regrowth in 2011 [1-3]. At that time the devices were shown to operate at a range of temperatures up to room temperature operated under pulsed drive conditions [1]. These devices had a threshold current density (J_{th}) of 10kA/cm^2, a divergence of 2.7° and a line width of 0.25nm.

Chapters 2 and 3 showed that there is considerable complexity in the design of photonic crystal lasers. For the band structure modelling (Chapter 2) there are two areas of particular interest, r=0.15a and r=0.4a. For r-0.15a the ratio of in-plane to out-of-plane coupling is maximum while at r=0.4a the absolute values of coupling are maximum. While the waveguide modelling (Chapter 3) found that void structures have lower mode overlap with the PC region for a Basic PCSEL waveguide and that the coupling is highest when active and PC layers are close. It was also shown that the mode overlap in void PCSELs can be improved with waveguide modifications. As only all semiconductor PCSELs are considered, the structure in this section is the "basic" structure shown in figure 3.3, and is the same as in previous work with the active and PC layers very close. The PC region has been modified such that the atom radius has been increased to 0.4a, this will give higher values of both in-plane and out-of-plane coupling.

This chapter will discuss progress in all-semiconductor PCSELs by initially describing the growth and fabrication of PCSEL devices, showing the realisation of CW operation at room temperature. Subsequently, a 2D PCSEL array is demonstrated where devices separated by a large distance can have their coherence controlled electronically. It is also shown that neighbouring devices can mutually increase their power and are thermally isolated. This opens up opportunities for new schemes in power scaling.

Growth and Fabrication

This section briefly outlines the growth and fabrication methods used to produce the all-semiconductor PCSELs described later in this chapter. I would like to take this opportunity to acknowledge and thank all the people involved in the growth and fabrication of these devices. Wafer growth and overgrowth was conducted by Dr B. Stevens at the EPSRC National Centre for III-V Technologies at the University of Sheffield; Electron beam lithography (EBL) and etch of PC was conducted by G. Ternent, S. Thoms and H. Zhou in the James Watt Nano-Fabrication Centre at the University of Glasgow. Device fabrication was conducted by N. Babazadeh, K. Kennedy, K. Groom and L. Shepherd in the clean rooms of the EPSRC National Centre for III-V Technologies at the University of Sheffield. I performed the device design and test.

Initial growth was carried out on a GaAs substrate and consisted of: 1.5µm of n-$Al_{0.4}Ga_{0.6}As$, three 8nm $In_{0.2}Ga_{0.8}As$ quantum wells (QW) (separated by GaAs barriers 20nm thick), a 40 nm p-$In_{0.48}Ga_{0.52}P$ etch stop layer and a 20 nm p-GaAs buffer layer. Above this is 150 or 300 nm of p-$In_{0.48}Ga_{0.52}P$ (depending on the structure) and a 20 nm p-GaAs terminating layer. Electron beam lithography (EBL) is used to define the 150µm by 150 µm photonic crystal area, the PC region itself consists of circular atoms on a square lattice with a period of between 285 and 297 nm, after the EBL the atoms are etched. (The EBL and the etching were carried out by colleagues at Glasgow University.) Figure 4.1 shows the scanning electron microscope (SEM) image of a PC region after etching but before regrowth from the top (a) and side (b). Showing the atoms have vertical sidewalls and that the atom period is consistent across the PC region. After etching prior to regrowth the patterned wafer is etched in buffered HF for 30 seconds prior to being loaded into the growth reactor. This step removes native oxide, removing any residual particles or stains.

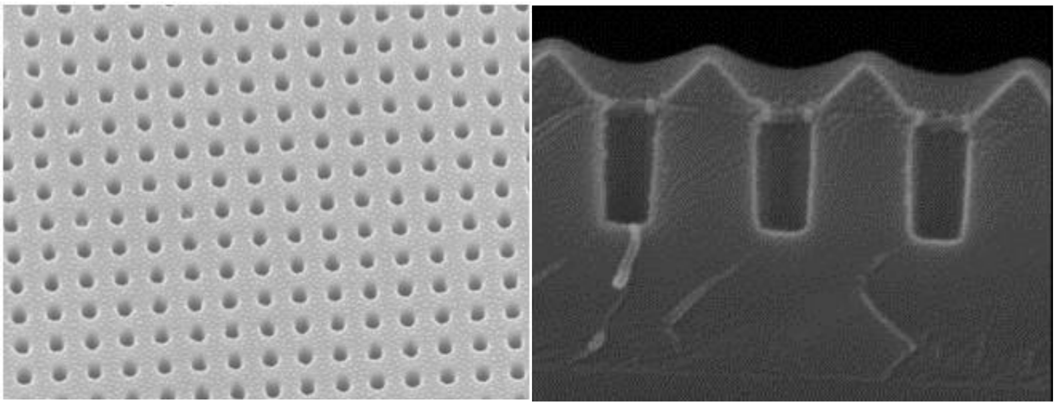

Figure 4.1 Scanning electron microscope (SEM) image of a PC region after etching but before regrowth from the top (a) and side (b) (images curtsey of G. Ternent)

Figure 4.2 (a), shows the TEM image of the initial regrowth where the wafer misorientation is 3^o off (110). Within the photonic crystal layer circular voids can clearly be seen. As described in chapter 2 this structure is not optimal, having a void containing PC layer, so efforts were made to optimise the growth to remove these voids. The regrowth was altered such that the misorientation and V-III ratio was increased. The V-III ratio was increased because it was believed that this would promote Ga diffusion and inhibit void formation. Figure 4.2(b) shows the TEM image of a regrowth after the misorientation and v-iii ratio increase. The voids are still visible within the PC layer but have a reduced volume and the shape has changed from spherical to droplet shaped. The final regrowth kept all the parameters constant but reduced the PC layer thickness from 300nm to 150nm. Figure 4.2(c) shows the final regrowth showing that the voids have been completely removed from the PC layer, however the GaAs AlGaAs interface is not planar and the thickness has been reduced compared to the other cases.

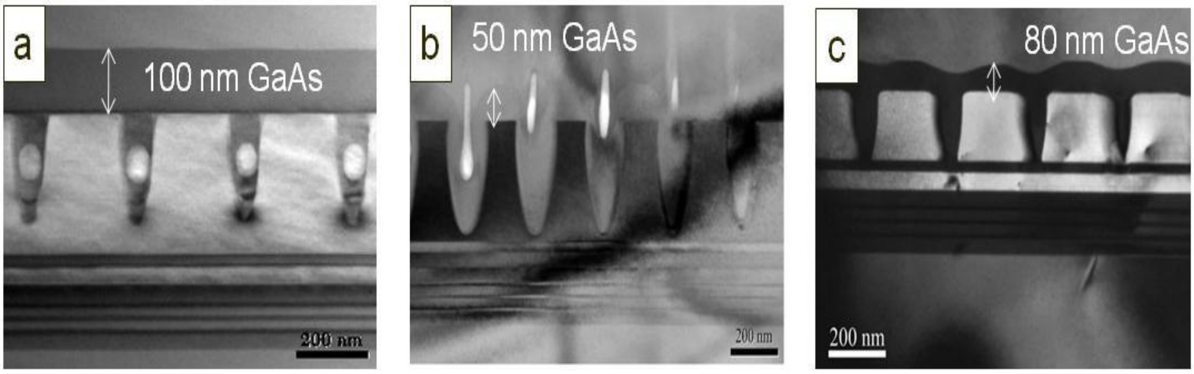

Figure 4.2 TEM image of successful regrowths, images are supplied by Integrity Scientific [1-3]

Following regrowth, devices were formed by etching a 100µm mesa in the p+GaAs contact layer above the centre of the photonic crystal. An annular gold contact was defined, providing a 52 µm aperture for light extraction. The electrically driven region (100µm diameter plus current spreading) is smaller than the regrown photonic crystal area (150µm x 150µm).

4.1 Characterisation of a Single PCSEL

In this section a single PCSEL device is characterised, the device has the same structure as in Wiliams *et. al.,* and is shown in figure 3.3. Figure 4.3 shows the electroluminescence (EL) spectra of an all-semiconductor PCSEL, the current applied to the device is continuous wave (CW) at 70mA, the collection angle is 18°. The inset (top right) shows the same spectra in more detail, showing the device has a narrow line width of 0.5nm. The lasing peak occurs at 991nm. The inset (top left) shows the subthreshold spectra of the same device operating at 20 (blue), 40 (red) and 60mA (green).

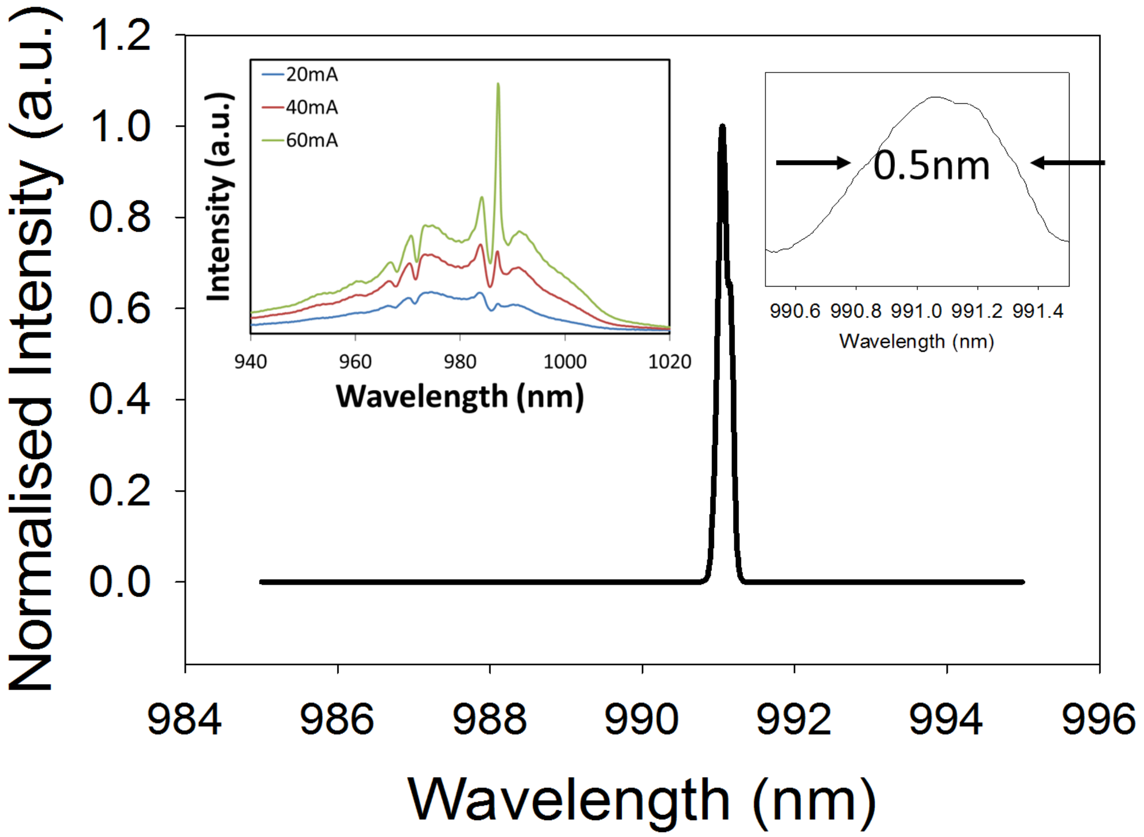

Figure 4.3 Electroluminescence and spectra of single device at 70 mA

Figure 4.4 shows the electroluminescence spectra of a PCSEL from William measured at room temperature under pulsed conditions operating at 100mA (blue) and 250mA (red). The peak lasing wavelength is ~960nm and the lasing linewidth is 0.5nm. The difference in lasing wavelength is due to a difference in device period.

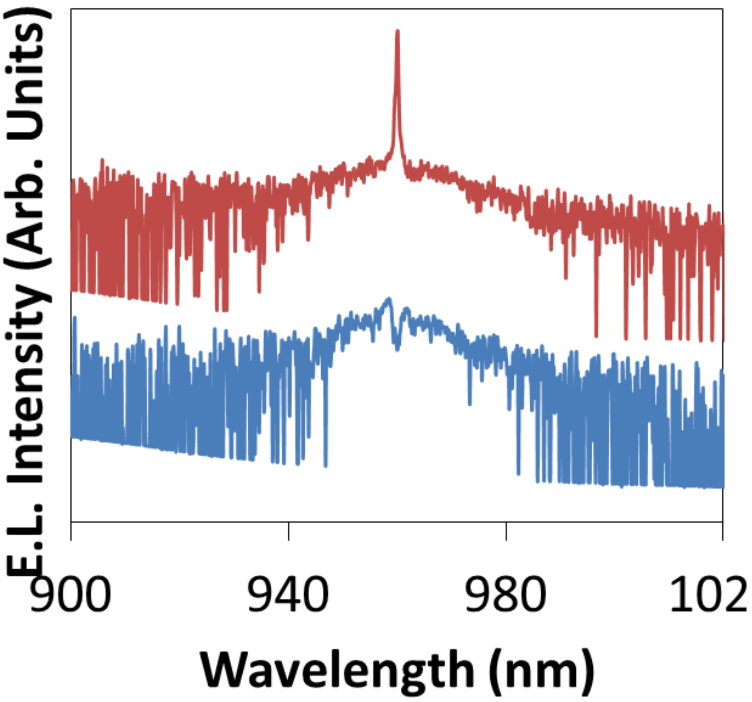

Figure 4.4 electroluminescence spectra of a PCSEL from Williams *et. al.*, [1-3]

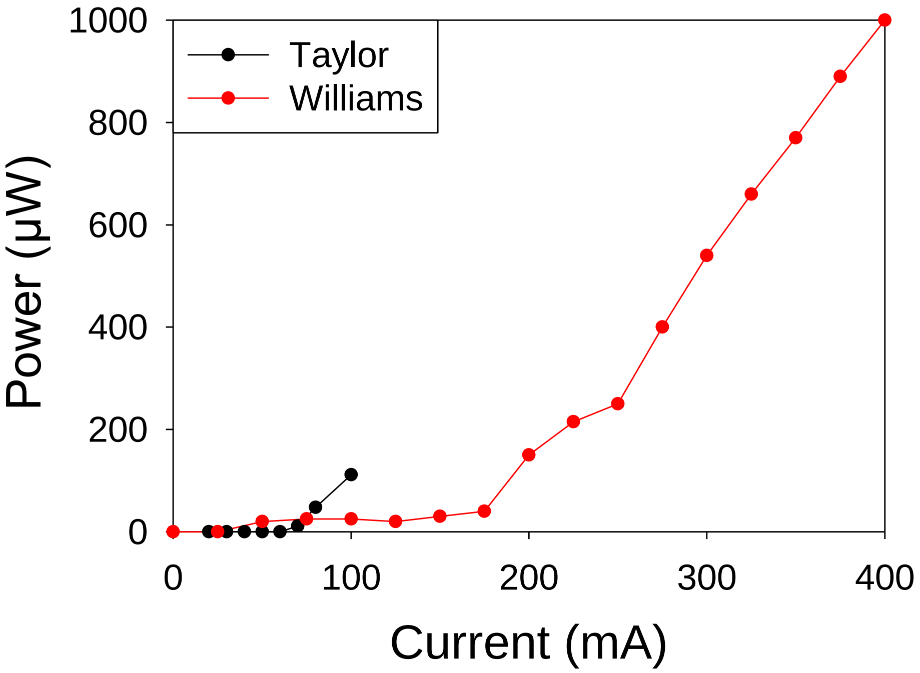

Figure 4.5 Spectral power peak output as a function of current for a device from Williams *et. al.*,[red] and from this work (black)

Figure 4.5 plots the LI characteristics of a PCSEL device from this work (black) and from Williams *et al.,* where the device from this work is operated CW room temperature and the device from Williams *et al.,* is operated pulsed. The threshold current (I_{th}) of the device is 65mA, which gives a threshold current density (J_{th}) of ~0.8kA/cm^2. Devices in Williams *et, al.,* had a threshold current of 200mA and a diameter of 50µm, giving a J_{th} of ~10kA/cm^2. The external differential efficiency of the Williams device is 5µW/mA compared to 3.3µW/mA. This is a significant reduction in the J_{th} and can be attributed to a number of possible differences between the two devices. Firstly, these devices have an atom radius of 0.4a (compared to ~0.2) which is shown in chapter 3 to give a high coupling coefficient, reducing threshold gain, secondly the cleaning process before re-growth was improved by Ben Stevens, and finally the re-growth process has been improved which may result in fewer defect states.

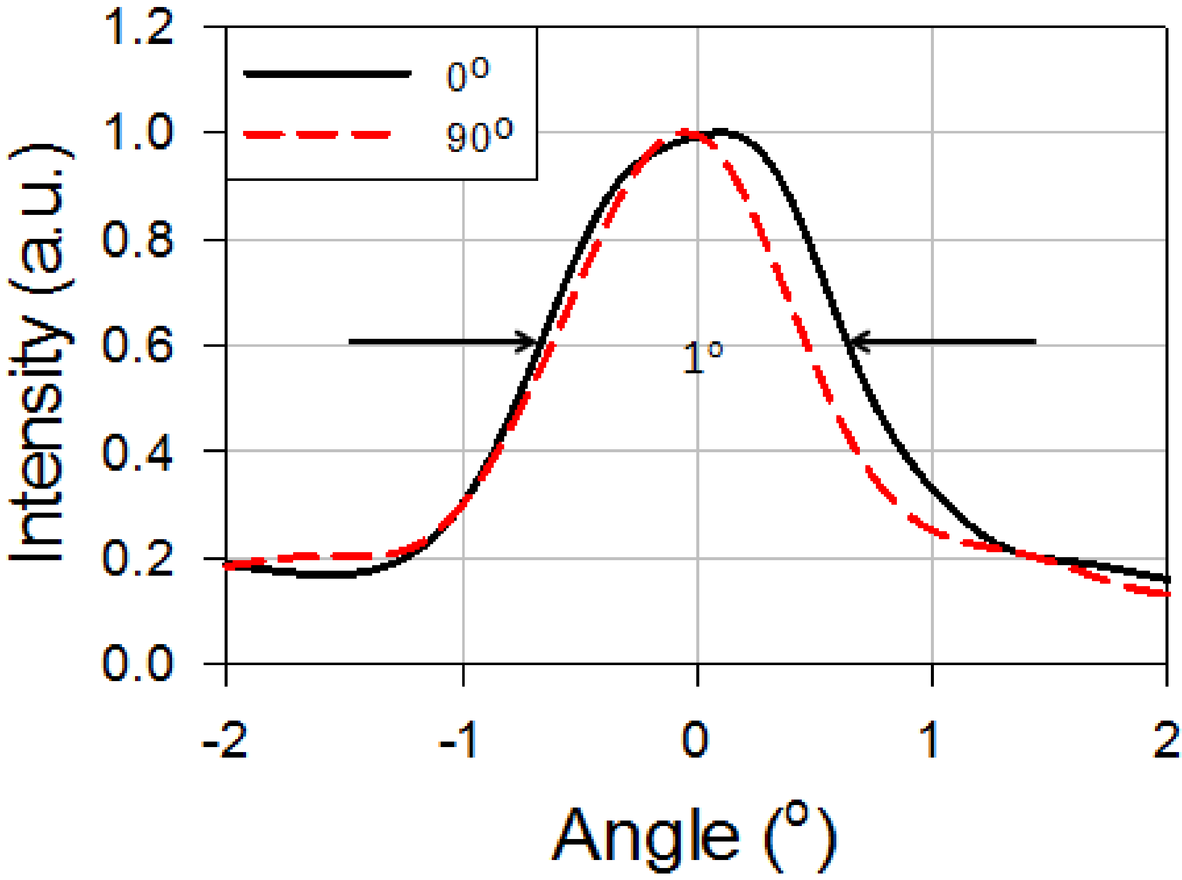

Figure 4.6 Farfield cross section of θ = 0º (black line) and θ=90º (red dashed line)

Figure 4.6 shows the two perpendicular cross sections 0º (solid black line) and 90º (red dashed line) of the normalised farfield pattern of a typical PCSEL operating at 100mA CW at room temperature. Figure 4.7 shows the farfield of a PCSEL from Williams *et. al.*,for a device operating above threshold showing the device farfield is 2.7º . The difference in the divergence angle may be a result of the side wall verticality. This demonstrates a divergence of ~1º, Williams *et, al.*, demonstrated divergence of similar devices of ~2.7º [1-3]. A value of ~1º is similar to Imada *et, al.*, [4]. For both the directions (0º and 90º) the divergence is ~1º however the 90º cross section has a very slightly lower divergence indicating the far field patter is slightly cylindrical. Williams *et, al.*, achieved a power ~1mW while these devices are limited to only ~100µW, this power is much less than Hirose *et, al.,* [5] The reduced divergence and power may be a result of a difference in side walls. The side walls in this case are more vertical than in Williams *et, al.,* The effect of asymmetry on the output power has been discussed for PCSELs by Hirose *et, al.,*[5] and sidewall verticality in PC containing VCSELs by Ivanov *et, al.,* [6] the effect of varying PC fill along the growth direction can be expected to increase far field angle.

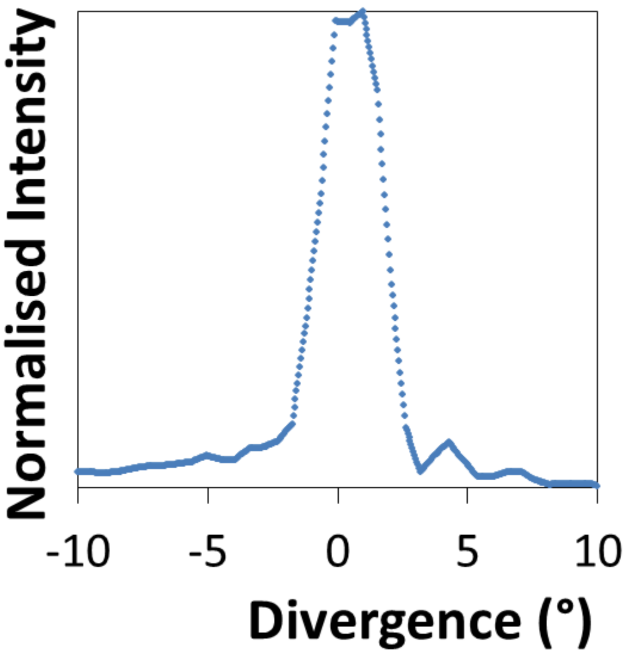

Figure 4.7 farfield patern of a PCSEL from Williams et. al., [1-3]

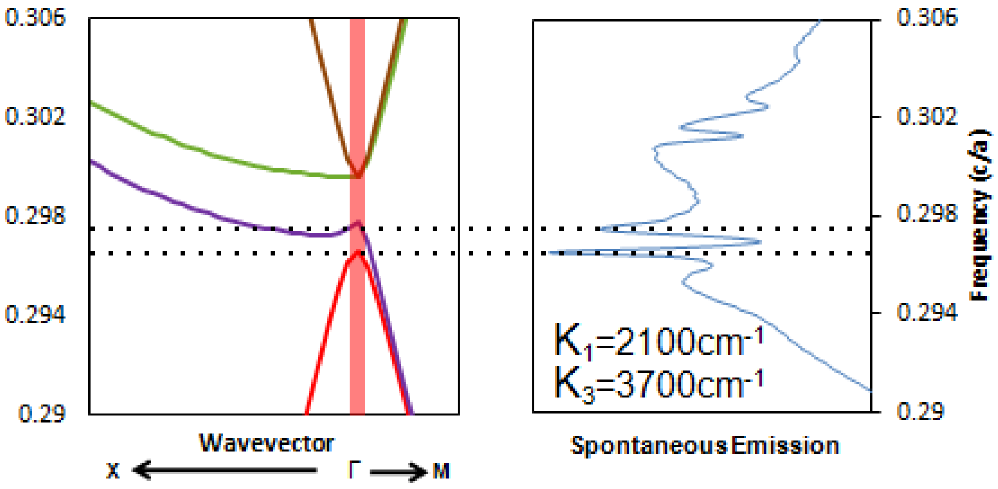

Figure 4.8 the modelled bandstructure of a PCSEL and the measured spectra

Figure 4.8 shows the modelled band structure of a PC (on the left) and the measured sub threshold spectra (shown on a log scale) of a device with the same parameters (on the right). Modelled data was obtained using MIT photonic bands (MPB) [7], and follows Taylor *et, al.*, [8], the structure modelled is assumed to be infinite and to contain only a PC consisting of circular "atoms" on a square lattice where the atom radius is 0.4 c/a and assumes a period of 293nm. The spectrum, shown on the right, is for a PCSEL device with a period of 295nm. The device was operated at room temperature under CW conditions and was measured using an optical spectrum analyser (OSA) with laser emission collected into a multimode fibre, NA=0.48 (i.e. over a range of k). The modelled data is in units of c/a, data (measured in nm) in converted to these units by dividing the period by the wavelength. The spectrum shows multiple peaks corresponding to PC band edges. The lowest frequency peaks in the spectrum fit very well to the lowest energy bands of the modelled band structure, whilst the higher frequency peaks appear at higher energy than predicted by the modelled band structure. The discrepancies between the modelled and experimental data are likely to be caused by a combination of a range of deviations from perfection, such as: the etched holes not having a perfectly flat bottom; the atom radius not being equal for all atoms; the regrown structure where GaAs becomes AlGaAs not being taken into account; and the fact that the E-field is not constant across the PC in our waveguide. We note that this sort of fit (lowest frequency fitting very well, while the remainder of the band structure fitting poorly) is observed in a range of reports [9].

Summary – Individual Device

This section demonstrated CW room temperature operation of all-semiconductor PCSELs showing that these devices lase at ~990nm, have a lasing threshold of 65mA (J_{th}=800Acm^{-2}), have low divergence (~1°) and that the modelled band structure (from chapter 2) closely predicts the spectral emission of devices. The devices shown here have a lower threshold current density, lower divergence and a lower power than previously reported all-semiconductor PCSELs. These differences are attributed to a combination of factors affecting device performance. Firstly the atom radius is increased in these devices which (as shown in chapter 3) has an effect on device coupling and hence threshold gain. Secondly, side wall verticality is much steeper in these devices and the different overgrowth may have resulted in fewer defects within the PC layer.

4.2 Coupled PCSEL Array

As discussed in chapter 1 PC micro cavity arrays have been demonstrated and coherent coupling between these cavities has been shown [10], in general micro cavities have low power due to their low mode volume and due to strong confinement exhibit highly divergent beams. VCSEL arrays with a PC grating in the top contact have shown coherence and beam steering [11]. PCSEL arrays have demonstrated power as high as 35W [12] but the devices in these arrays have not demonstrated coherence or that coherence can be controlled, the devices are also close to one another and therefore lateral heat extraction may be an issue.

This section demonstrates a PCSEL array which consists of individual PCSEL mesa diodes, described in the previous section. The devices are separated by 1mm and between the devices is a contacted region which does not contain PC patterning. Power scaling is demonstrated, where applying current to the region between the PCSEL devices allows power from one device to be increased by increasing the current applied to another device in the array. Then adjacent devices are shown to be coherent and that the coherence can be controlled electronically. Finally, coupling of PCSELs in a 2D array is demonstrated.

Power Scaling

As mentioned in previous sections PCSELs have the potential to deliver power which scales with area. There are however problems with increasing device power by increasing device size. As device size increases it is necessary to apply current over the whole device area, lateral current spreading is generally of the order of the current spreading layer thickness. As a results specialist electrical contacts are required, for example transparent contacts (such as ITO) [13]. If current is not applied uniformly across the whole device then coherence may not be maintained. Also as device size increases, the applied current must increase, leading to additional heat generation and lateral heat extraction becomes a problem. It is these factors that will ultimately limit the power scalability of PCSELs. This section demonstrates power scaling from a 2D coherent PCSEL array. Individual PCSELs are separated by a large distance (1mm) and are thermally isolated, these devices are connected in an array (figure 4.6) and power scaling between two devices is shown.

Figure 4.9 shows the schematic of a 2x2 PCSEL array, where each PCSEL is an electrically isolated mesa diode laser with a 100µm contact and a 50µm aperture. Devices are separated by 1mm, a gold 100µm wide contact is situated between each device (this will be referred to as the coupler). This array takes advantage of the in-plane scattering of the PC. Within a single device any light scattered in-plane at the edge of the photonic crystal would simply travel into the un-pumped waveguide and be absorbed, acting as a loss mechanism. By pumping the region between devices into transparency it is possible for this light to be coupled between adjacent devices.

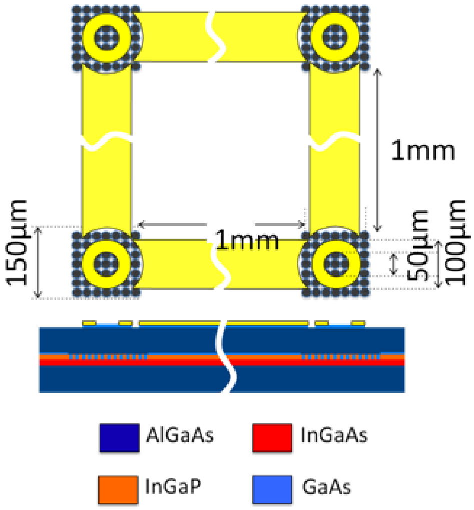

Figure 4.9 Schematic of 2 by 2 coupled PCSEL array

Figure 4.10 shows the lasing spectra of 4 different PCSELs on the same coupled device. Each of the devices was operated CW at 100mA at room temperature. The peak lasing wavelength of the 4 devices is 990nm and there is almost no variation between devices.

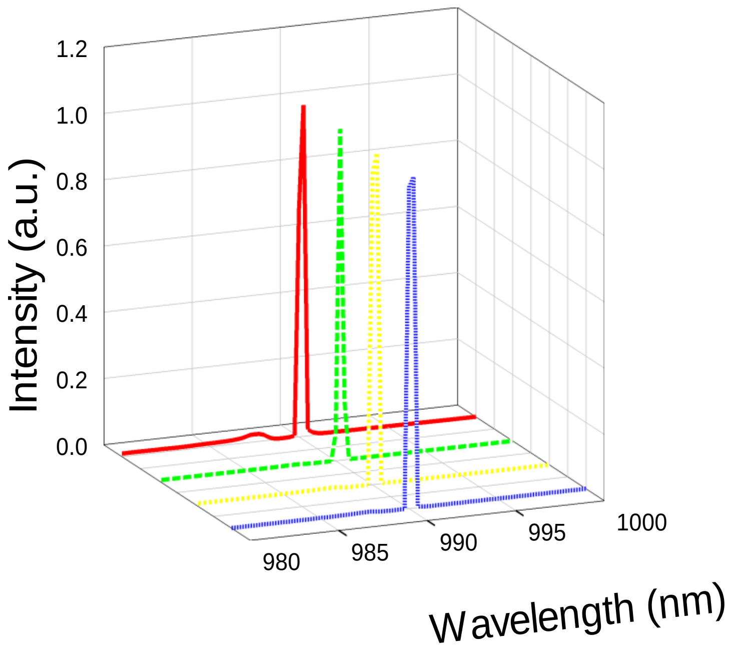

Figure 4.10 spectra of 4 neighbouring devices on the same coupled device with each device operated at 100mA CW at room temperature

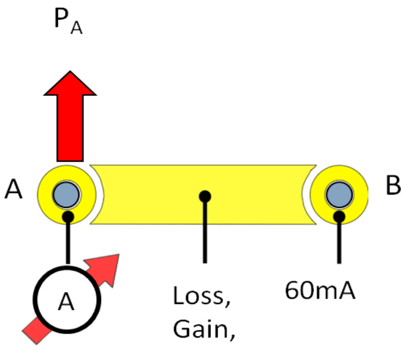

Figure 4.11 Schematic of 1 by 2 PCSEL array showing applied current values of each section of the device, in this configuration PCSEL A is observed and has applied current varied, PCSEL B is sub threshold and the coupler is either in gain or loss.

For simplicity, to explain power scaling effects, figure 4.11 shows the schematic of a 1 by 2 PCSEL array. PCSEL A is observed and has its applied current varied, PCSEL B is operated sub threshold and the coupler is either in gain or loss. Characterisation of the gain material suggests J_0 is 210Acm^{-2} (courtesy of Alex Crombie). J_0 is the threshold current density of an infinitely long laser and was obtained by measuring the threshold current density for different lengths of coupler, plotting J_{th} against inverse cavity length and extrapolation to 1/L=0, this give the current density required to overcome the internal loss and allows us to operate the coupler close to transparency. However the current was carefully varied in the coupler to determine a loss $I_l(J_l)$ of 200mA (200A/cm^2) and a gain $I_l(J_l)$ of 220mA (220A/cm^2). It is worth emphasising the "loss" and "gain" are very close to transparency.

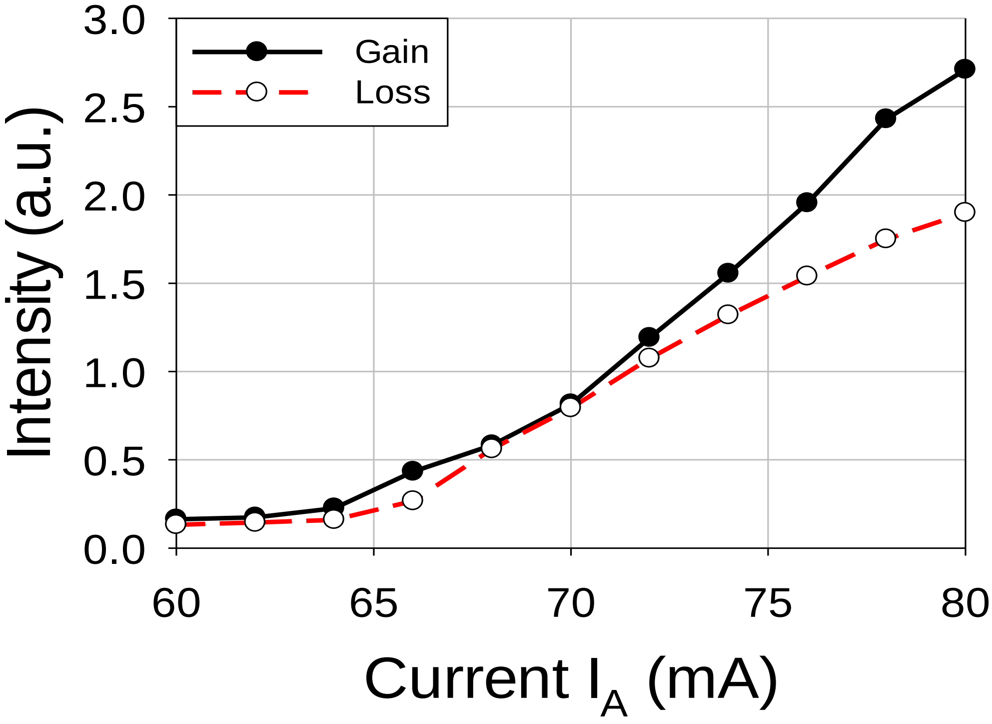

Figure 4.12 Power as a function of current for PCSEL A with PCSEL B kept below threshold and the coupler in loss (red dashed) and in gain (black solid)

Figure 4.12 shows the LI characteristics of PCSEL A for a range of currents from 60mA to 80mA. PCSEL B is kept sub threshold (60mA), with the coupler in loss (red dashed line) and in gain (black solid line). While the coupler is in loss the figure shows the threshold of

PCSEL A at ~65mA. When the coupler is in gain, the output of PCSEL A is increased. The increase in output power of PCSEL A is caused by light scattered in-plane from PCSEL B traversing the region between devices and being coupled out of PCSEL A. For this to be possible the region between the PCSELs must be transparent which is achieved by applying sufficient current to the coupler.

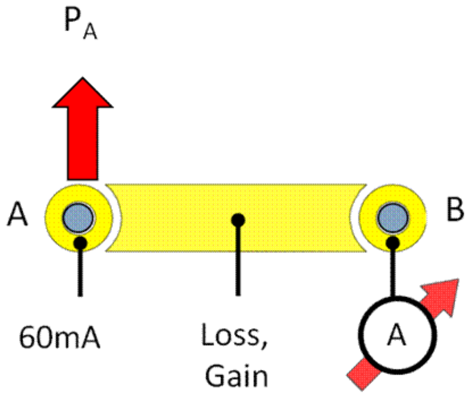

Figure 4.13 Schematic of 1 by 2 PCSEL array showing applied current values of each section of the device, in this configuration PCSEL A is observed and has applied current sub threshold, PCSEL B current is varied and the coupler is either in gain or loss.

Figure 4.13 shows the schematic of the complementary experiment on the 1 by 2 PCSEL array. In this experiment PCSEL A is observed and is kept sub threshold, PCSEL B has its current varied and the coupler is either in gain or loss.

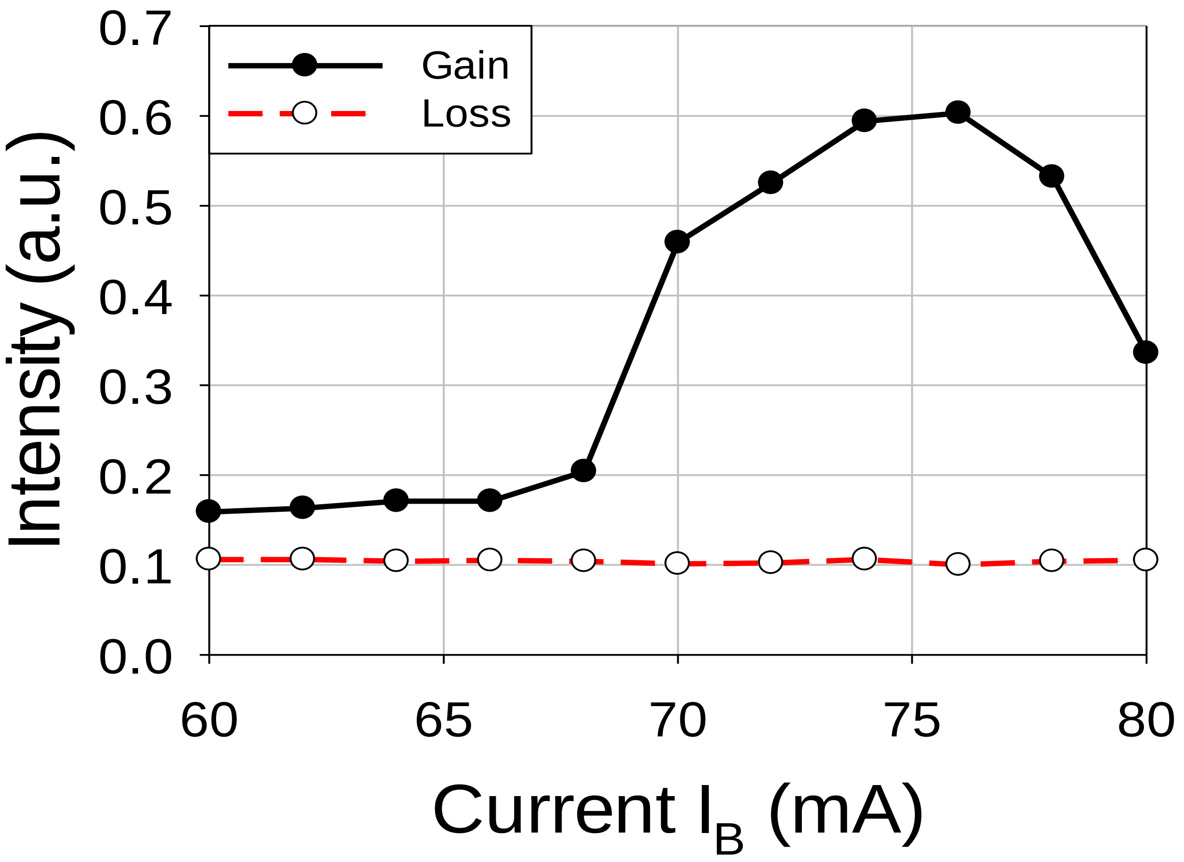

Figure 4.14 Power as a function of current for PCSEL A below threshold, PCSEL B current varying from 60mA to 80mA and the coupler in loss (red dashed) and in gain (black solid)

Figure 4.14 shows the LI characteristics of PCSEL A in this case with the current applied to PCSEL B varying from 60mA to 80mA with the coupler in loss (red dashed line) and in gain (black solid line). While the coupler is in loss the emission intensity of PCSEL A does not increase for the full range of currents considered, this shows that varying the current on PCSEL B has no effect on the optical power from PCSEL A. This demonstrates that the devices are electrically, optically and thermally isolated. With the coupler in gain optical power from PCSEL A is increased. The lasing threshold of PCSEL B is ~ 65mA and power from PCSEL B is travelling along the coupler and being scattered out of PCSEL A. For current I_B>75mA the power from PCSEL A decreases but remains at a level greater than for the coupler in loss. This roll-over in power is self heating of PCSEL B and the wavelength no longer matches the wavelength of the optical band of PCSEL A.

Summary – Power Scaling

This section demonstrates the use of a PCSEL array for power scaling. While the coupler is in loss the devices are demonstrated to be electrically, optically and thermally isolated. By applying sufficient current to the coupler section, the power output from a single PCSEL is increased by increasing the current applied to an adjacent device, this array promises a route to high brightness devices by allowing devices to be coupled over a large area.

4.3 Coherence Control

In this section the coherence of adjacent PCSELs in an array is demonstrated. When devices are coupled (and the coupler is in gain) they are shown to be coherent only when both devices are lasing. The devices are shown to be incoherent when either one of the devices is sub threshold or when the coupler is in loss. Electronically controllable coherence between the lasers is therefore demonstrated. The same is shown for a 2 by 2 array demonstrating a 2 dimensional array with coherence control.

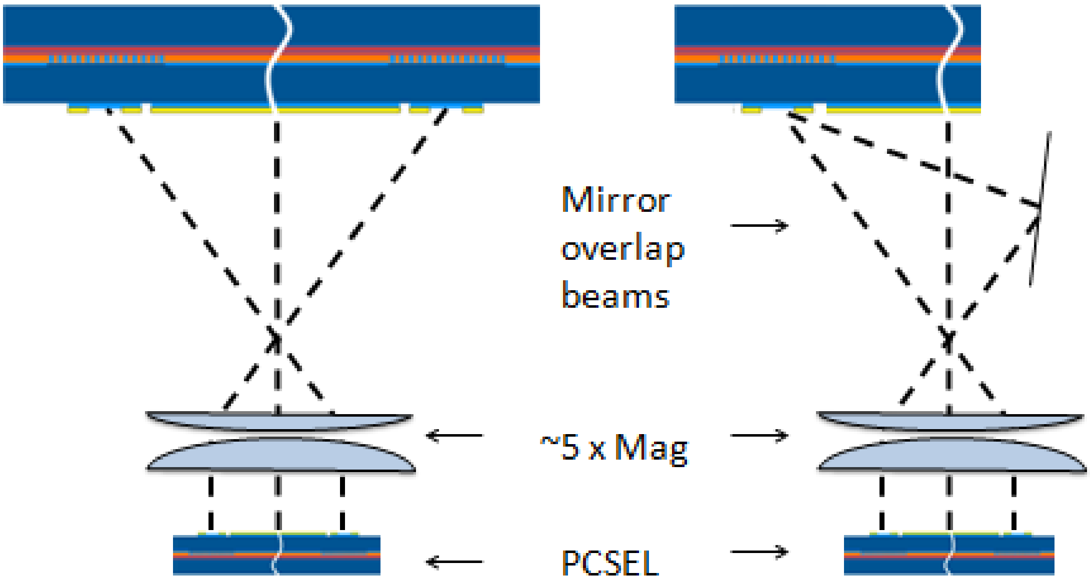

Figure 4.15 schematic of experimental setup for coherence control, left hand image shows near field image of a PCSEL array magnified onto a camera while in the right hand image a mirror reflects the nearfield image of one PCSEL so that it overlays the image of another PCSEL

Figure 4.15 shows a schematic of the experimental setup for demonstrating coherence. The left hand of the figure shows the near field image of a PCSEL array being cast through a lens onto a camera, the right hand of the figure shows the schematic where the same image is cast but a mirror reflects the near field image of one device so that it overlays the nearfield image onto that of another device. If the two sources are coherent then overlaying the images will result in interference giving a number of dark and light fringes [14], where the fringe spacing is determined by the path length difference and the fringe spacing will be $S = \frac{\lambda D}{d}$ where S is fringe spacing, $\boldsymbol{\lambda}$ is the vacuum wavelength of light, d is the separation of sources and D is the distance between source and image [15]. This is essentially a Young's double slit experiment realised in the solid state.

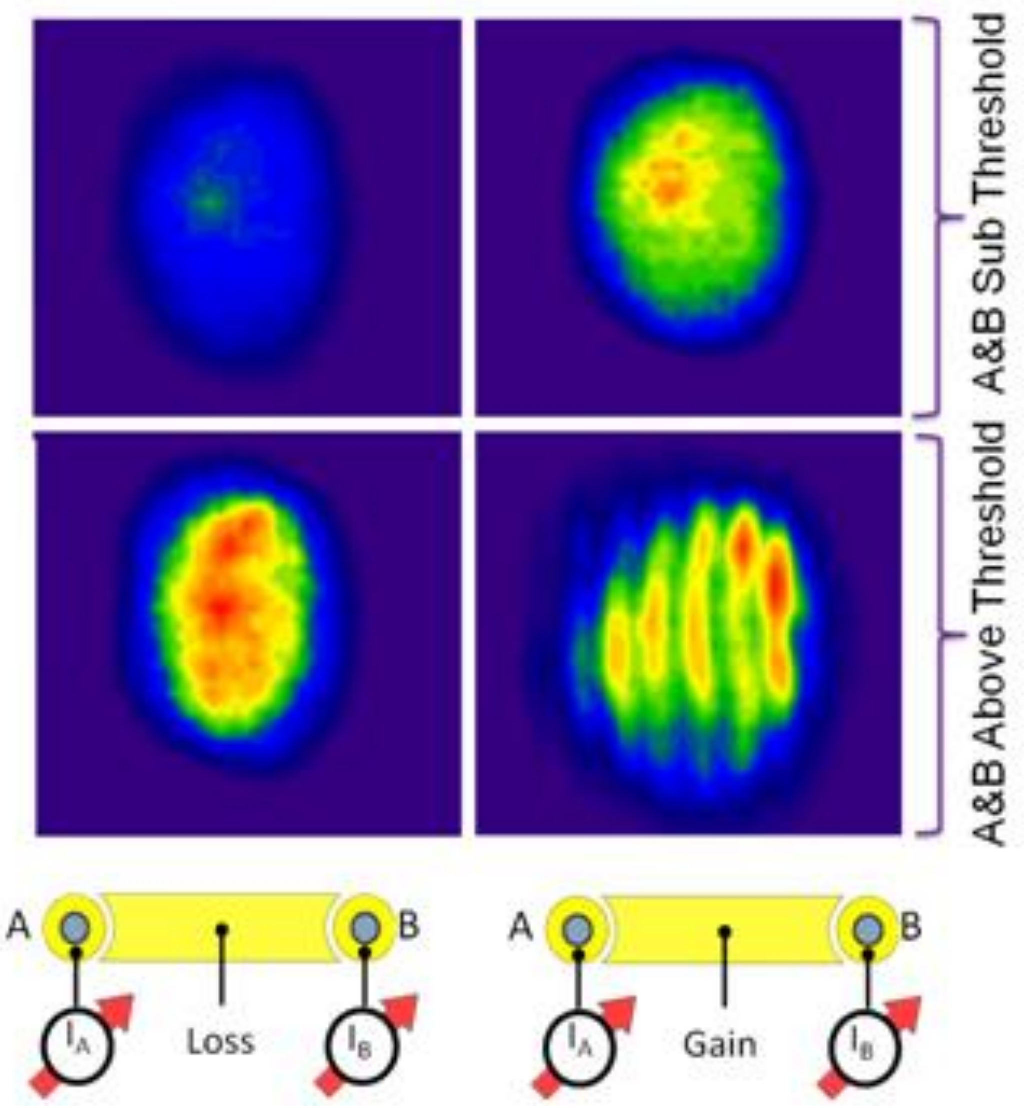

Figure 4.16 near field images of two PCSELs overlaid where both devices are subthreshold and the coupler is in loss (top left) both devices are subthreshold and the coupler is in gain (top right) both devices are lasing and the coupler is in loss (bottom left) and both devices are lasing and the coupler is in gain with schematics showing both where current is applied

Figure 4.16 shows results from the experiment described in figure 4.12. The top left image shows the case where both devices are sub threshold and the coupler is in loss, this shows a low intensity and no fringes, demonstrating that the devices are incoherent. The top right image shows the case where both devices are subthreshold and the coupler is in gain. For this case there are still no fringes but the intensity is increased due to some additional spontaneous emission from the coupler being coupled out by the PCSEL. The top right image shows the case where both devices are lasing and the coupler is in loss. This shows an increase in intensity again, but still shows no fringes demonstrating that although the devices are lasing they are incoherent, and the two devices are operating independently. The bottom right image shows the case where both devices are lasing and the coupler is in gain, in this case there is a fringe pattern demonstrating that the devices are now coherent. This shows that not only are the devices coherent with each other but also that they are coherent across the whole device area. In addition to demonstrating electronically controlled coherence between PCSELs for the first time, this is a first demonstration of coherence across the whole device area of one PCSEL. Previously, the identical lasing wavelength over the device area had been taken as proof of this [4].The calculated fringe spacing of this setup is 36µm, the measured spacing 36.6µm (±5µm), which is in excellent agreement.

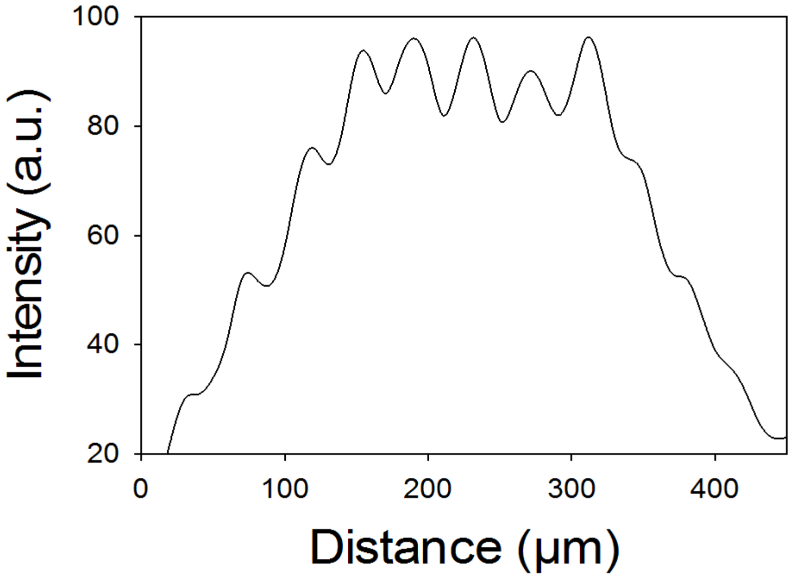

Figure 4.17 cross section of intensity through image where the near field image of 2 devices is overlaid, both devices are lasing and the coupler is in gain

Figure 4.17 shows the intensity pattern as a slice through the image from figure 4.2.7 where both devices are lasing and the coupler is in gain. The modulation depth is 20% and the fringe spacing is again ~36.6µm (±5µm).

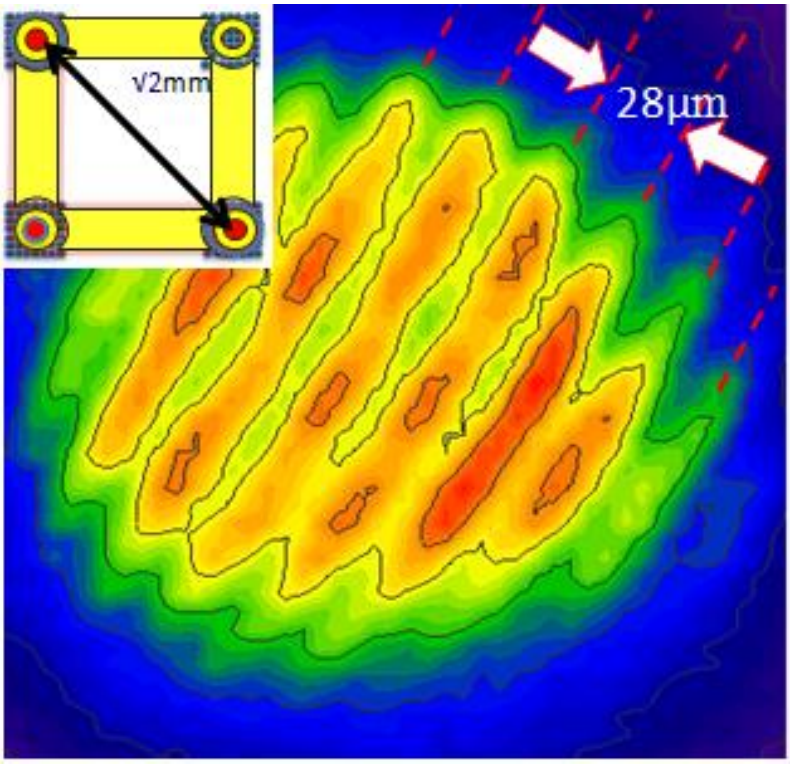

Figure 4.18 overlaid near field image of 2 PCSELs diagonally separated with both devices lasing couplers between them in gain and device between them sub threshold, inset shows schematic of how devices are operating

The inset to figure 4.18 shows a coherence experiment where PCSELs are coupled via a neighbouring PCSEL through a 90° bend. Both lasers are operated at 100mA (I_{th} =65mA), the PCSEL they are coupled through is operated at threshold (65mA) to overcome all losses. The two couplers are operated just above transparency (220mA). Figure 4.18 shows the near field images of the 2 corner PCSELs overlaid. This image shows a fringe pattern where the fringe spacing is 28µm, the theoretical spacing should be 25.5µm (36/√2) 26µm. This therefore demonstrates that the two devices are coherent with each other and that each device is coherent across its own emission area. This shows that using a PCSEL array can give 2 dimensional coupling with electronic coherence control.

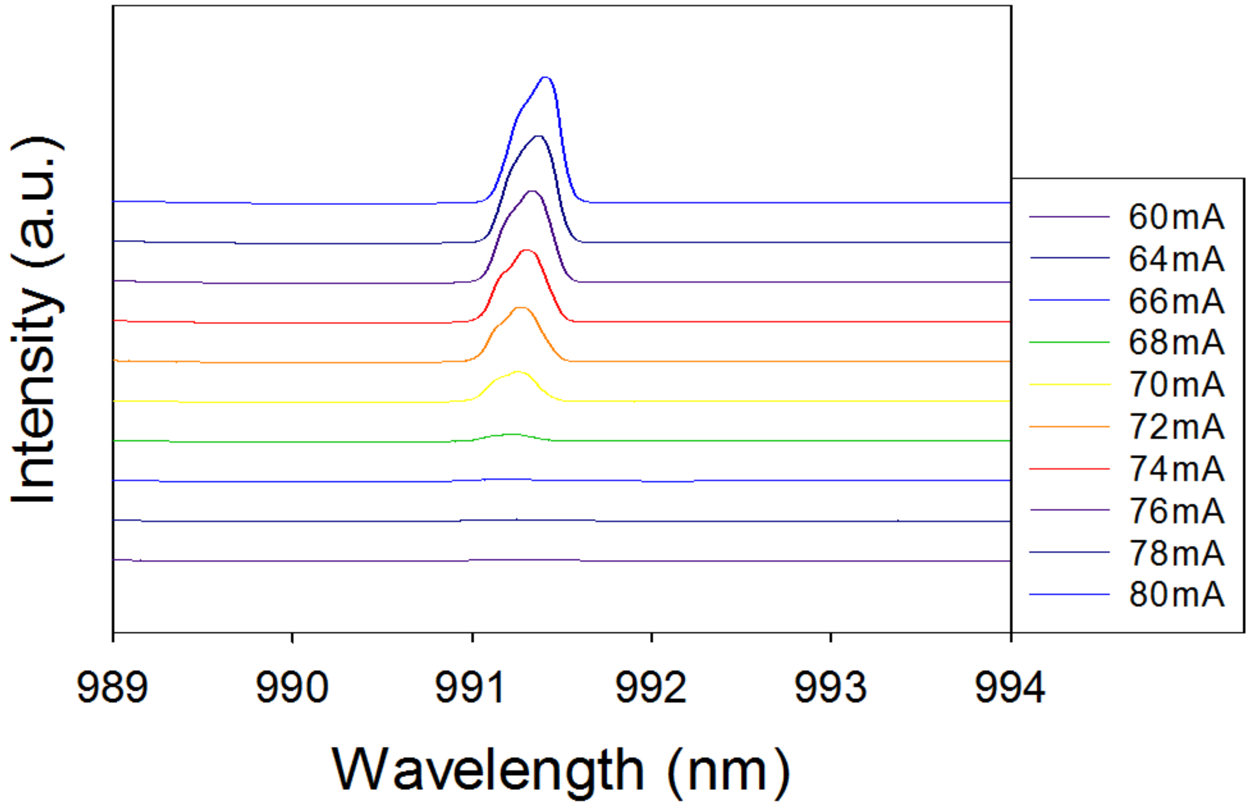

Figure 4.19 electroluminescence spectra of 1x2 PCSEL array where the current in the observed PCSEL (I_A) is varied from 60mA to 80mA, the coupler is in loss with the coupler current at 200mA and the unobserved PCSEL current (I_B) is 80mA. Values of I_A are offset as an aid to the eye.

Figure 4.19 shows the electroluminescence spectra of 1x2 PCSEL array where the current in the observed PCSEL (I_A) is varied from 60mA to 80mA, the coupler is in loss with the coupler current at 200mA and the unobserved PCSEL current (I_B) is 80mA. As the current I_A is increased the lasing peak of the PCSEL is observed.

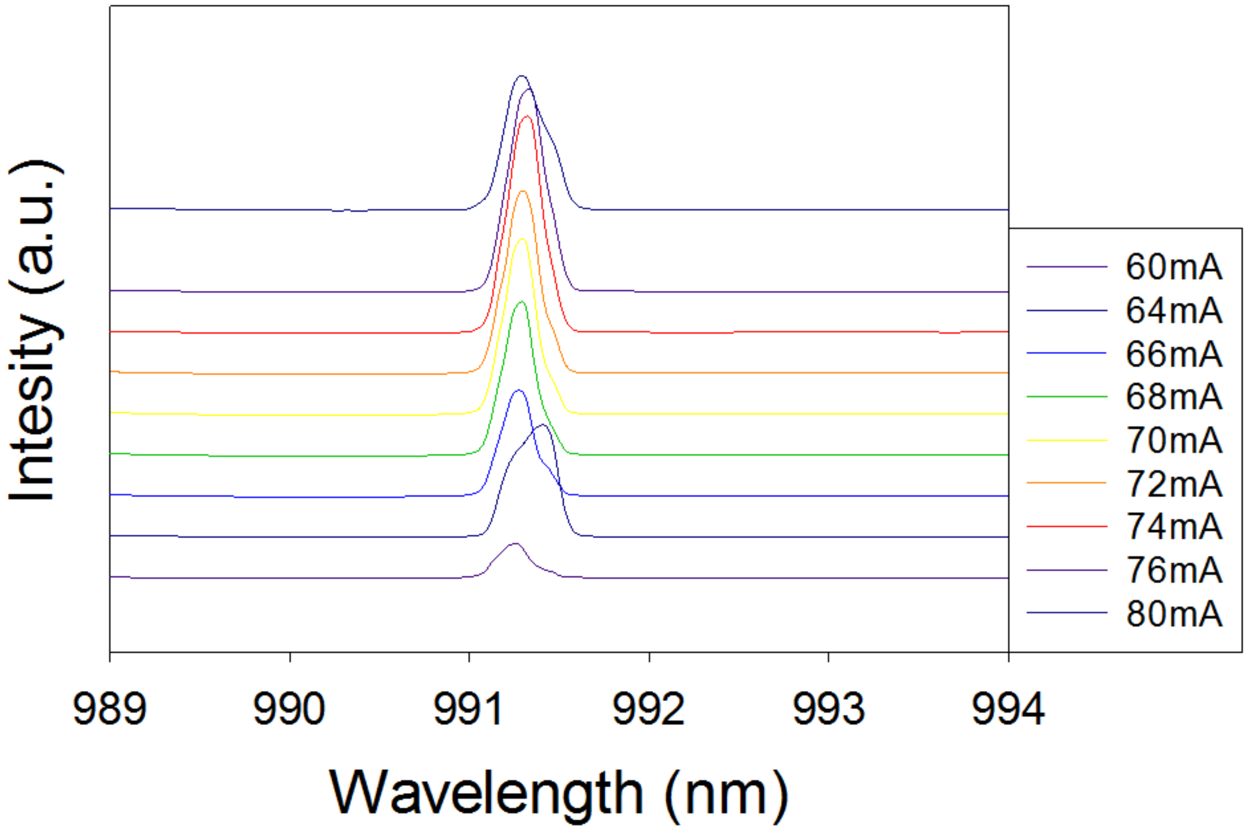

Figure 4.20 electroluminescence spectra of 1x2 PCSEL array where the current in the observed PCSEL (I_A) is varied from 60mA to 80mA, the coupler is in Gain with the coupler current at 220mA and the unobserved PCSEL current (I_B) is 80mA. Values of I_A are offset as an aid to the eye.

Figure 4.20 shows the electroluminescence spectra of 1x2 PCSEL array where the current in the observed PCSEL (I_A) is varied from 60mA to 80mA, the coupler is in Gain with the coupler current at 220mA and the unobserved PCSEL current (I_B) is 80mA. The peak observed at low current can be attributed to Light scattered from the adjacent PCSEL traveling along the coupler region and being scattered out of $PCSEL_A$. Once $PCSEL_A$ is above threshold (65mA) the lasing peak of the observed $PCSEL_A$ is then seen and the peak is at a slightly lower wavelength.

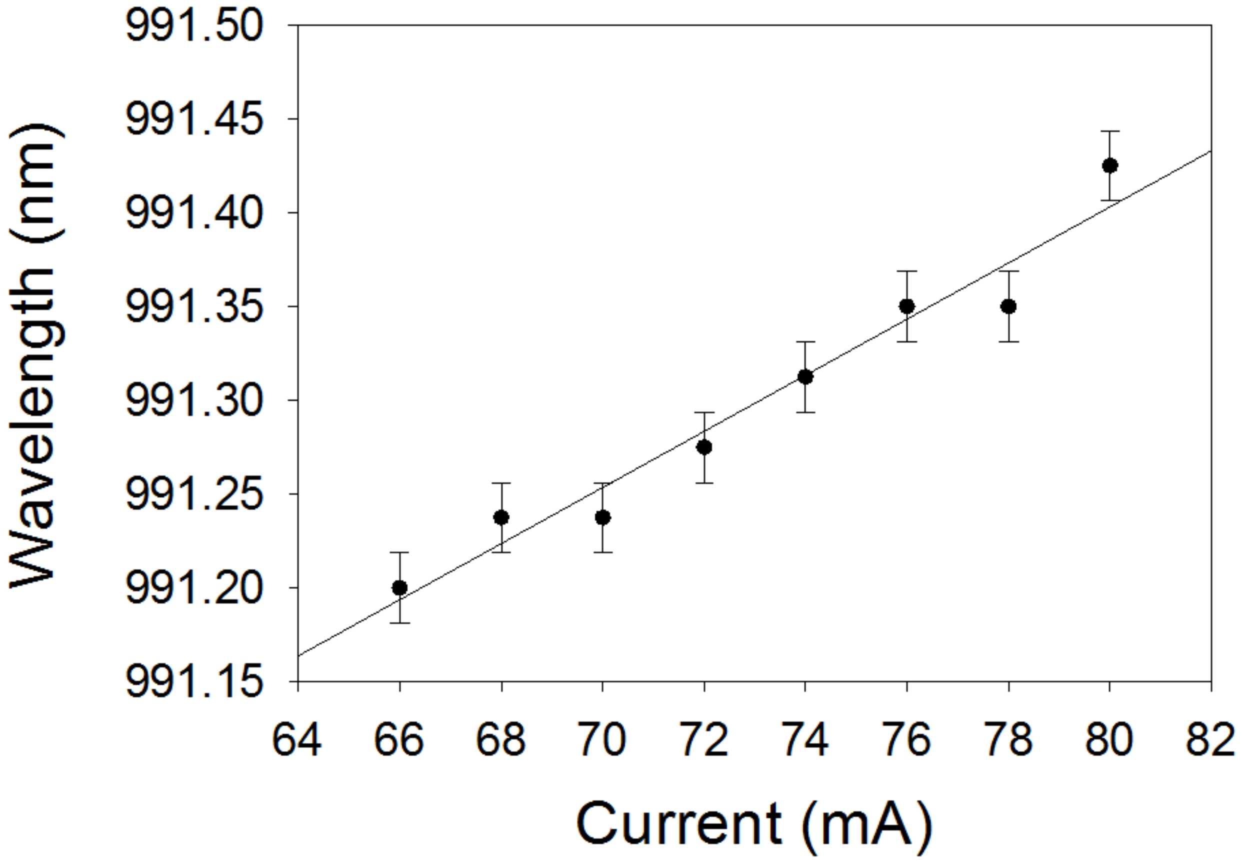

Figure 4.21 peak wavelength vs applied current for a 1x2 PCSEL array where the current in the observed PCSEL$_A$ is varied from 66mA to 80mA, the coupler is in loss with the coupler current at 200mA and the unobserved PCSEL$_B$ current is 80mA

Figure 4.21 shows the peak wavelength as a function of applied current for a 1x2 PCSEL array where the current in the observed PCSEL$_A$ is varied from 66mA to 80mA, the coupler is in loss with the coupler current at 200mA and the unobserved PCSEL$_B$ current is 80mA, peak wavelength is taken from figure 4.16. the peak wavelength increases as current increases and for the range of currents measured the wavelength increases from 991.2nm to 991.43nm over a current range from 66 to 80nm, giving a peak shift of 0.016nm/mA.

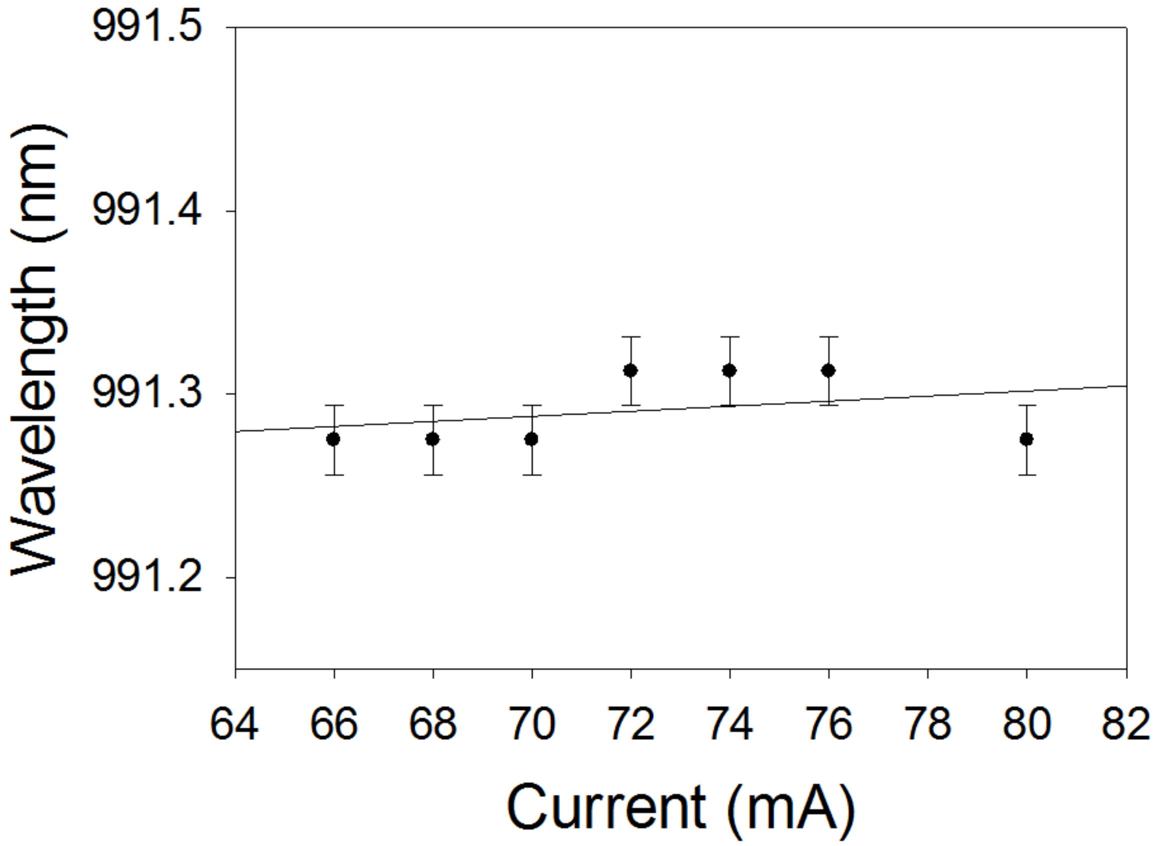

Figure 4.22 peak wavelength vs applied current for a 1x2 PCSEL array where the current in the observed PCSEL$_A$ is varied from 66mA to 80mA, the coupler is in Gain with the coupler current at 220mA and the unobserved PCSEL$_B$ current is 80mA

Figure 4.22 shows the peak wavelength as a function of applied current for a 1x2 PCSEL array where the current in the observed PCSEL$_A$ is varied from 66mA to 80mA, the coupler is in gain with the coupler current at 220mA and the unobserved PCSEL$_B$ current is 80mA, peak wavelength is taken from figure 4.17. For the full range of observed currents the peak wavelength is either 991.275nm or 991.325nm indicating that the peak wavelength is effectively constant. This indicates that with the coupler in gain the observed PCSEL is insensitive to heating, which may be due to the device becoming locked with the adjacent device.

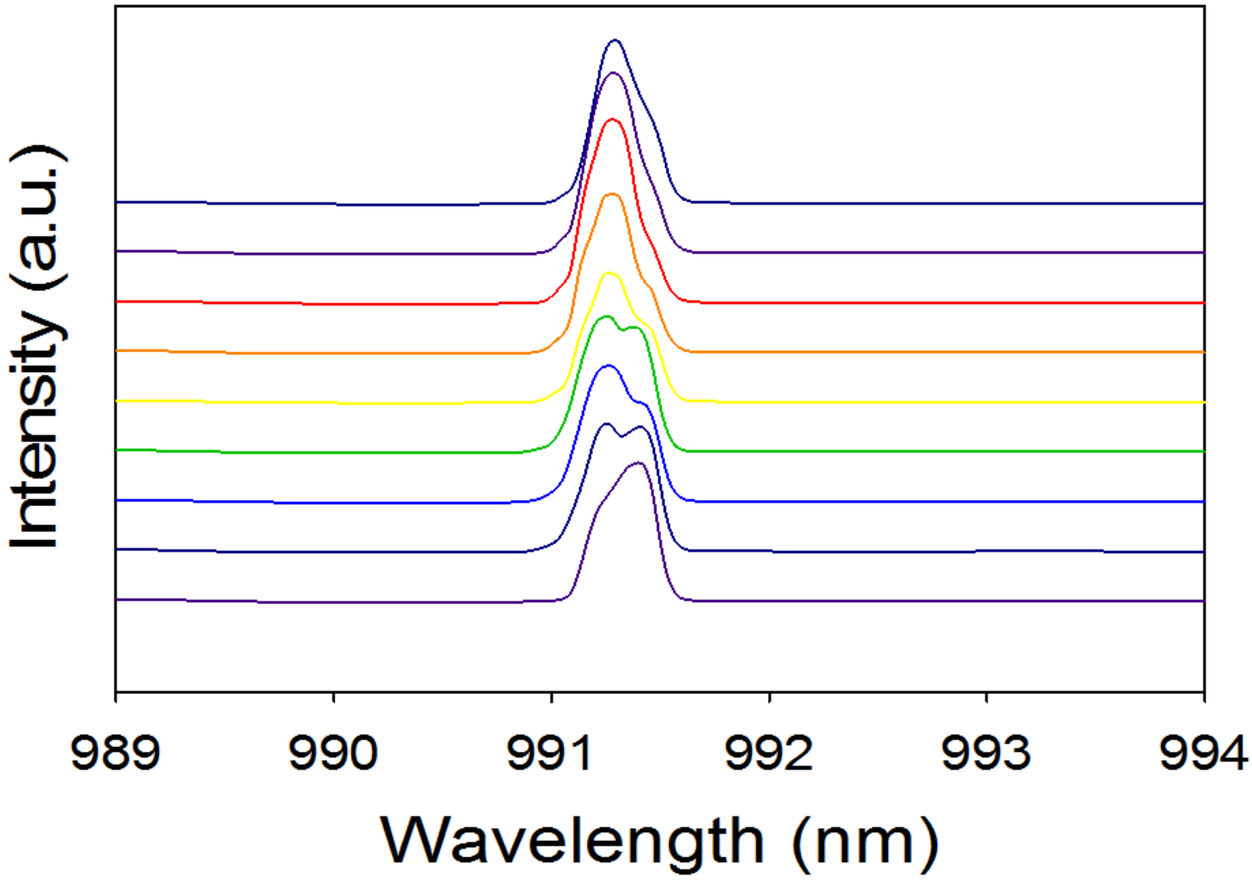

Figure 4.23 electroluminescence spectra of 1x2 PCSEL array where the current in the observed PCSEL$_A$ is at 80mA, the coupler is in gain with the coupler current at 220mA and the unobserved PCSEL$_B$ current varied from 60mA to 80mA. Values of I$_A$ are offset as an aid to the eye.

Figure 4.23 shows the electroluminescence spectra of 1x2 PCSEL array where the current in the observed PCSEL$_A$ is kept at 80mA, the coupler is in Gain with the coupler current at 220mA and the unobserved PCSEL$_B$ current is varied from 60mA to 80mA. Initially a peak can be seen which is attributed to the lasing peak of the observed device, as the applied current is increased the a second peak attributed to the lasing of the other device emerges. The second peak which appears is at a lower wavelength and becomes the dominant peak at current greater than 66mA.

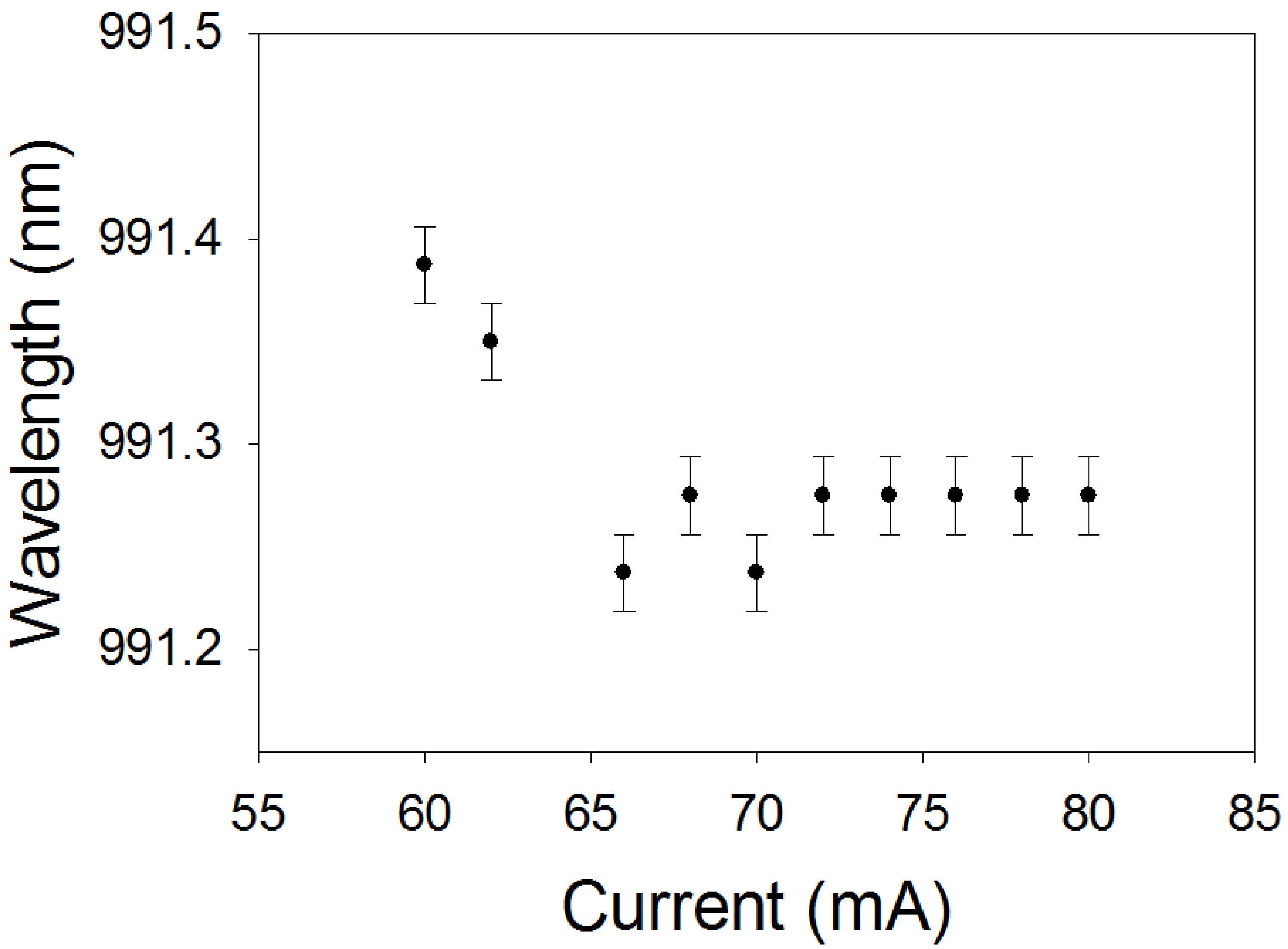

Figure 4.24 peak wavelength vs applied current for a 1x2 PCSEL array where the current in the observed PCSEL$_A$ is kept constant at 80mA, the coupler is in gain with the coupler current at 220mA and the unobserved PCSEL$_B$ current is varied from 60 to 80mA

Figure 4.24 shows the peak wavelength as a function of applied current for a 1x2 PCSEL array where the current in the observed PCSEL$_A$ is at 80mA, the coupler is in Gain with the coupler current at 220mA and the unobserved PCSEL$_B$ current is varied from 60mA to 80mA, peak wavelength is taken from figure 4.20. As the applied current is increased from 60mA to 66mA the peak wavelength reduces from ~991.4nm to ~991.25nm, for currents $I_B >$ 66mA the peak wavelength is either 991.28nm or 991.24nm. This result suggests that the peak of the observed PCSEL is locking to the peak of the other PCSEL and that this occurs at about the threshold of the PCSEL.

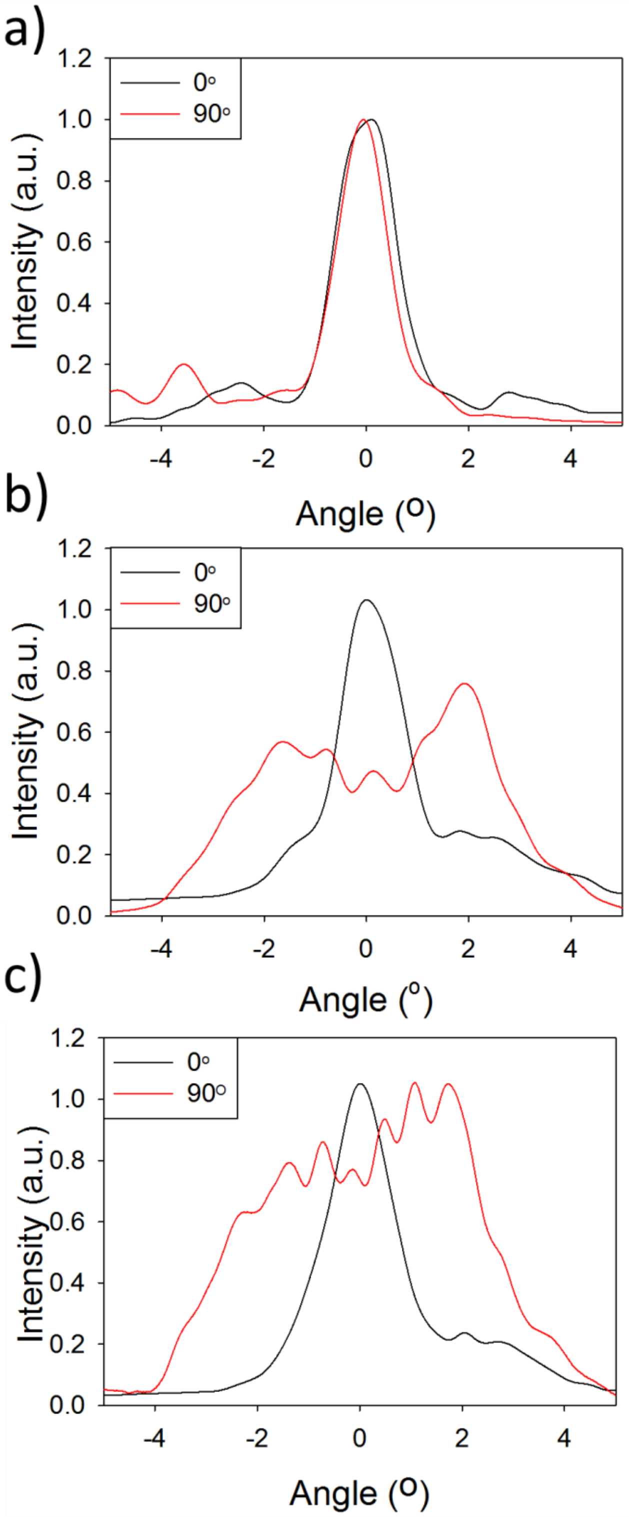

Figure 4.25 far field patter of a 1 x 2 PCSEL array where a) PCSEL$_A$ is lasing b) PCSEL$_A$ and PCSEL$_B$ are lasing and the coupler is in loss and c) PCSEL$_A$ and PCSEL$_B$ are lasing and the coupler is in gain

Figure 4.25a) shows the far field pattern of a 1 x 2 PCSEL array where $PCSEL_A$ is lasing. Figure 4.25b) and c) show the far field patter when both $PCSEL_A$ and $PCSEL_B$ are lasing and the coupler is in loss (200mA) and in gain (220mA) respectively. In figure 4.25a) a single peak is observed with a divergence of ~1°. In figure 4.25b) the 0° direction shows no change but the 90° direction shows 2 peaks at 2 and -2 degrees each peak is likely be to from each of the two PCSELs. The far field in figure 4.25c) shows again an unchanged 0° direction while the 90° direction shows multiple peaks, these peaks could be further evidence of the PCSELs being coherent.

Summary – Coherence Control

This section demonstrates electronic control of coherence for a PCSEL array. The coherence between adjacent devices is electronically controllable. With two devices lasing and the intervening coupler/PCSEL region in loss the two devices are incoherent. With the two PCSELs lasing and the intervening coupler/PCSEL regions in gain the devices become coherent. Furthermore, 2D arrays coupling at 90° is demonstrated.

4.4 Conclusions

This chapter demonstrated a PCSEL array where each PCSEL is an independent mesa diode laser with a 100µm contact and a 50µm aperture. Devices are separated by 1mm, a gold 100µm wide contact (coupler) is positioned between devices. Initially individual devices are characterised and shown to have a threshold of 65mA, the far field is measured and a divergence of 1° is shown and the laser line width is 0.5nm. The array demonstrates power scaling between neighbouring devices. With the coupler in loss the two devices are electrically, thermally and optically isolated. With the coupler in gain, increasing the current on one device increases the output power of an adjacent device. This demonstrates power scaling over a large distance (1mm) and offers power scaling over a large area and a potential route to high brightness devices. The arrayed devices are then used to demonstrate electronic control of coherence between devices. If the coupler is in loss, adjacent devices are incoherent irrespective of whether the individual devices are lasing. With the coupler in gain two neighbouring devices are shown to be coherent and electronic control of coherence is possible. This demonstrates that the coherence of devices is electronically controllable. The coherence and its control is then shown to operate over 2 dimensions, and through 90^o scattering in a 3rd PCSEL. Next the spectra of an arrayed is observed and the peak wavelength when the coupler is in loss is shown to increase as applied current increases. However, when the coupler is in gain and current to the observed PCSEL is varied the peak wavelength becomes effectively constant, this suggests that the lasing wavelength of the two PCSELs is locked. Finally the far field of a coupled array is observed and found to give two peaks when the coupler is in loss but to show numerous peaks when the coupler is in gain.

References

[1] D. M. Williams

“All-semiconductor photonic crystal surface emitting lasers at 980 nm through epitaxial regrowth”

PhD thesis, University of Sheffield, 58, 2014

[2] D. Williams, K. Groom, D. Childs, R. Taylor, S. Khamas, R. Hogg, B. Stevens, N. Ikeda, Y. Sugimoto

”Optimisation of coupling between photonic crystal and active elements in an epitaxially regrown GaAs based photonic crystal surface emitting laser”

Japanese journal of applied physics, **51**, 02BG05-1-3, February 2012

[3] D. Williams, K. Groom, D. Childs, R. Taylor, S. Khamas, R. Hogg, B. Stevens, N. Ikeda, Y. Sugimoto

“Epitaxially regrown GaAs-based photonic crystal surface emitting laser”

IEEE photonics technology letters, **24**, 11, 966-968, June 2012

[4] M. Imada, S. Noda, A. Chutinan, T. Tokuda, M. Murata and G. Sasaki.

“Coherent two-dimensional lasing action in surface-emitting laser with triangular-lattice photonic crystal structure”

Applied Physics Letters, **75**, 3, 316, 1999

[5] K. Hirose, Y. Liang, Y. Kurosaka, A. Watanabe, T. Sugiyama & S. Noda,

“Watt-class high-power, high-beam-quality photonic-crystal lasers”

Nature Photonics, **8**, 406-411, 2014

[6] P Ivanov, Y-L D Ho, M J Cryan and J Rorison,

“Modelling investigations of DBRs and cavities with photonic crystal holes for application in VCSELs”

Journal of Optics, **14**, 125103, 2012

[7] http://ab-initio.mit.edu/wiki/index.php/MIT_Photonic_Bands

[8] R. Taylor, D. Williams, J. Orchard, D. Childs, S. Khamas and R. Hogg

“Band structure and waveguide modelling of epitaxially regrown photonic crystal surface emitting lasers”

Journal of Physics D, 46, 26, 264005(8pp), July 2013

[9] K. Sakai, E. Miyai, T. Sakaguchi, D. Ohnihis, T. Okano and S. Noda

Lasing band edge identification for a surface emitting photonic crystal laser

IEEE Journal on selected areas in communicaions, **23**, 7, 1335, 2005

[10] Y. Sato, Y. Tanaka, J. Upham, Y. Takahashi, T. Asano and S. Noda

”Strong coupling between distant photonic nanocavities and its dynamic control”

Nature photonics, **6**, 56-61,2012

[11] M. T. Johnson, D. F. Siriani, M. P. Tan, and K. D. Choquette,

“Relative phase tuning of coupled defects in photonic crystal vertical-cavity surface-emitting lasers”

Journal of Selected Topics in Quantum Electronics, **19**, 1701006, 2013.

[12] T. Sakaguchi1, W. Kunishi1, S. Arimura, K. Nagase, E. Miyai, D. Ohnishi, K. Sakai and S. Noda

“Surface-Emitting Photonic-Crystal Laser with 35W Peak Power”

Conference on Lasers and Electro-Optics (CLEO) and the International Quantum Electronics Conference (IQEC), 2009

[13] H. Kim, A. Piqué, J. Horwitz, H. Mattoussi, H. Murata, Z. Kafafi and D. Chrisey,

“Indium tin oxide thin films for organic light-emitting devices”

Applied Physics Letters **74**, 3444, 1999

[14] R. Feynman

“The Feynman lectures on physics: the definitive edition”

volume I, pearson, 0-8053-9046-4, chapter 29, 2006

[15] M. Keating, Gemetric,

“physical and visual optics”

butterworth-heinmann, chapter 22, 2002

5. Conclusions and Future Work

5.1 Band Structure Modelling - Summary

For both type I and type II structures the band structure is observed to change as atom radius increases. For type I structure, the higher frequency bands are degenerate for r~≥0.2a and the lower frequency bands are split. As r increases to ~0.3a the bands have shifted and overlapped leaving no zone centre separation. As the radius is increased further (to r=0.4a) the zone centre separation has re-emerged with the lower frequency bands being degenerate and the higher frequency bands being split. For type II: the opposite is the case.

From band structure modelling, in-plane and out-of-plane coupling for type I and type II are calculated [1]. Both PC types follow a similar pattern with K_1 having a peak at r~0.4a and K_3 having 2 peaks at r~0.15a and r~0.45a. A choice of r~0.15a results in moderately high K_3 and low K_1. On the other hand a choice of r~0.45a results in both K_3 and K_1 being high. The double peak nature of the in-plane coupling is similar to results founds by M. Yokoyama and S. Noda [2] where Q-factor is found to be dependent on band structure and exhibits a double peak at r=0.15a and r=0.4a. A higher Q is obtained at r=0.15a. This is attributed to an increase in the in-plane coupling with increasing r. The independent control of the relative strength of K_3 and K_1 with atom radius is highlighted, and is expected to be a valuable tool in future PCSEL optimisation.

Finally, the effects of the magnetic field distribution bring about additional design considerations with regard to a change in the nature of the modes [3,4].

5.2 Band Structure Modelling - Future Work

An experimental confirmation of the effect of atom radius on band-structure and coupling coefficient would be a key first step. In particular, the effect of a change in the ratio of K_1:K_3 for r=0.2a and r=0.4a would be of interest. A possible issue would be in the large emission wavelength difference (~50nm) for such structures requiring two separate devices to be fabricated, leading to possible issues in making a fair comparison. However, the effect of the large difference in K_1 for these two structures should be evident.

In the short term, modelling of triangular PC shapes is of present need within the research group, as we are now in a position to move towards high powers [5]. The derivation of K_1 and K_3 for triangular and Kagome lattices would also be of interest, as these structures may have potential for high coupling. Kagome structures are known to produce flatter band-structure [6] leading to a difference in threshold and coupling, but have not yet been used in PCSELs.

The model considered in this thesis does not account for gain or loss within the PC, this could be included by having an imaginary component of the refractive index. Having regions of loss and gain within the PC will alter the in-plane magnetic field and it may be possible to change the symmetry and hence the nature of the modes and far field. Such a device could be realised by etching the PC through the active region and using over growth.

A significant issue in PCSEL design is the inverse problem, where calculating a particular band-structure and in-plane electric field distribution is simple for a given PC shape, but the inverse is computationally difficult (i.e. a solution may not exist). Solutions to this issue will need to utilise topographic optimisation strategies [7], such as brute force, or the adjoint method [8]. Optimisation of the PC for asymmetry of the in-plane electric field, and for the design of custom far-field patterns would be key outputs, as only trial and error has so far been applied [9,10].

In order to accurately characterise the complete band-structure, measuring the photocurrent at the X1, M1, and Γ 3 point could be performed. This may require some additional sample preparation steps, and may require specialist characterisation equipment (several tuneable lasers), but this would provide a unique and accurate tool to link modelling and fabrication.

Full 3D simulations are now becoming possible, and future development in this area will allow full flexibility in design for the PCSEL. Most notably, including asymmetry in the vertical direction has been highlighted as a key enabler for high output powers [5].

5.3 Waveguide Modelling – Summary

Initially, the effects of cladding layer refractive index and PC - QW separation thickness, were modelled for void containing and all-semiconductor PCSELs. In the structure considered (Williams *et, al.,* [11-13]) the all-semiconductor PCSEL is shown to give higher PC coupling coefficients in all cases. The mode profile suggest that the low weighted average of the refractive index of a void containing PC region is acting to push the mode away from the PC region which is giving the all-semiconductor PCSEL higher coupling.

A ballast layer structure is modelled and is intended to counter the effect of the mode being distorted away from the void containing PC region. The ballast layer is shown to increase PC coupling in both all-semiconductor and void containing structures. However, for the void containing structure the coupling coefficient does not increase sufficiently to be greater than that of an all-semiconductor PCSEL with no ballast layer. The importance of this layer in void containing PCSEL design is highlighted.

Next, the double decker structure is modelled and is also intended to increase the PC coupling within the structure. The double decker is shown to give higher coupling values for both all-semiconductor and void containing PCSEL and has shown a higher value of coupling for void containing PCSEL than for all-semiconductor PCSELs. However the void containing PCSEL only gave a bound mode for high cladding Al composition. Fabrication issues have been considered and a double decker structure (whether void containing or all-semiconductor) would have significant processing issues to overcome.

Finally, three PCSEL structures with emission spanning the UV to mid-IR (400nm, 1300nm and 10µm) were considered. To a first approximation the device designs were an existing edge emitting laser structure, with a PC layer in the upper waveguide cladding. In each case the all-semiconductor PCSEL had higher coupling than the void containing PCSEL. This highlight that it should be possible to obtain relatively high values of coupling, by including an all-semiconductor PC layer above the active region, in tried and trusted edge emitting laser structures. This is however, not the case for void containing PCSELs as additional structural modification may be required to gain high coupling coefficients.

5.4 Waveguide Modelling – Future Work

This work requires extension by considering the full range of PC fill-factors on both the mode profile and the relative strengths of K_1 and K_3. This would then provide a full understanding of design parameters on device performance. From work presented in chapter 3, a re-design of the standard University of Sheffield PCSEL structure would be beneficial.

In addition, the effect of thicker PC layers on the device operation should be explored. Whilst thicker PC layers will pose challenges for epitaxy, possible advantages in terms of coupling coefficients should be possible.

A limitation of this model is that is does not consider the gain or loss within the layers of the structure. The loss could be added into the model by modifying the refractive index to have an imaginary component. The PC region is expected to be lossy while the active region will have gain. Including gain and loss into the model is likely to modify the mode profile, in particular the mode may be further pushed away from the void PC. Future work should explore this further.

The different materials systems would benefit from investigation of the effect of ballast layers and double decker layers, to asses these as possible future devices.

5.5 Device – Summary

Continuous wave room temperature operation of all-semiconductor PCSELs is described, showing devices lasing at ~990nm, with a lasing threshold of 65mA (J_{th}=800Acm^{-2}), and a low divergence (~1°). The devices shown here have a lower threshold current density, lower divergence and a lower power than previously reported all-semiconductor PCSELs. These differences are attributed to a combination of factors affecting device performance. Firstly the atom radius is increased in these devices which (as shown in chapter 2) has an effect on device coupling and hence threshold gain Secondly, side wall verticality is much steeper in these devices and the different overgrowth may have lead to fewer defects within the PC layer.

An array of PCSELs demonstrates power scaling over a large separation distance (1mm). While the coupler is in loss the devices are demonstrated to be electrically, optically and thermally isolated. By applying sufficient current to the coupler section, the power output from a single PCSEL is increased by increasing the current applied to an adjacent PCSEL, this array promises a route to high brightness sources by allowing devices to be coupled over a large area.

Finally, electronic control of coherence for a PCSEL array is demonstrated for the first time. With two devices lasing and the intervening coupler/PCSEL region in loss the two devices are incoherent. With the two PCSELs lasing and the intervening coupler/PCSEL regions in gain the devices become coherent. Furthermore, 2D arrays coupling at 90^o is demonstrated.

5.6 Device – Future Work

The arrays demonstrated here are 2 x 2 arrays. Future work should investigate a larger array and examine the size/power limitations. Larger arrays would contain more electrical contacts leading to fabrication implications (e.g, vias) and would require significant heat sinking.

Having demonstrated power scaling, the research group is, now well placed to develop high power arrays. The next step therefore, is to change the atom shape from circular to triangular as in Hirose *et, al.*, [5]. This should give rise to high power all-semiconductor PCSELs and then high power PCSEL arrays. At present the low power of devices makes relative intensity noise (RIN) measurements impractical, and such higher power devices should permit RIN measurements to be performed. This would allow the sensitivity of the devices to external optical feedback to be measured. The comparatively low reverse coupling of external light into the waveguide may allow isolator free operation within a module.

As mentioned in chapter 2, light emitted out-of-plane is emitted equally in both directions meaning that as much light is absorbed by the substrate as is emitted. By placing a DBR underneath the active region (even if the reflectivity is low (0.8-0.95)) the output power of the PCSEL should be increased. Similarly placing a DBR around the PCSEL will reflect any light scattered in-plane but out of the PCSEL back into the PC. This system should increase the confinement and reduce the loss, reducing the threshold.

Finally, modelling should be extended to include the imaginary part of refractive index. This would allow areas of gain and loss to be positioned within the PCSEL and may result in novel in-plane electric fields, with low symmetry. These devices could be realised by etching into the QW layer and filling the pattern by epitaxial overgrowth [14].

References

[1] Y.Kurosaka, S. Iwahashi, K. Sakai, E. Miyai, W. Kunishi, D.Ohnishi and S. Noda

"Band structure observation of of 2D pgotonic crystal with various v shaped air hole arangements"

IEICE Electronics express, **6**, 13, 966, 2009

[2] S. Noda, M. Yokoyama, A. Chutinan, M. Imada, M. Mochizuki

"Polarization Mode Control of Two-Dimensional Photonic Crystal Laser by Unit Cell Structure Design"

Science, **293**, 1123, 2001

[3] M. Yokoyama, S. Noda

"Polarisation mode control of two-dimensional photomic crystal laser having a square lattice structure"

IEEE journal of quantum electronics,**39**, 9, 1074,2003

[4] S. Noda, M. Yokoyama, A. Chutinan, M. Imada, M. Mochizuki

"Polarization Mode Control of Two-Dimensional Photonic Crystal Laser by Unit Cell Structure Design"

Science, **293**, 1123, 2001

[5] K. Hirose, Y. Liang, Y. Kurosaka, W. Watanabe, T. Sugiyama and S.Noda

"Watt class high-power, high-beam-quality photonic-crystal lasers"

Nature photonics, **8**, 406-411, 2014

[6] H. Takeda, T. Takashima and K. Yoshino

"Flat Photonic bands in two-dimensional photonic crystals with Kagome lattices"

Journal of condensed matter, **16**, 631-6324, 2004

[7] P. Borel, A.Harpoth, L. Frandsen, M. Kristensen, P. Shi J. Jensen and O. Sigmund

"Topology optimisation and fabrication of photonic crystal structure"

Optics express, **12,** 9, 1996

[8] O. Miller

"Photonic design: from fundamental solar cell physics to computational inverse design"

PhD Thesis, chapter 5, page 62, University California, Berkley, 2012

[9] Y. Kurosaka, K. Sakai, E. Miyai, S. Noda,

"Controlling vertical optical confinement in two-dimensional surface-emitting photonic-crystal lasers by shape of air holes"

Optics express, 16, 22, 1848-18494, October 2008

[10] Y.Kurosaka, S. Iwahashi, K. Sakai, E. Miyai, W. Kunishi, D.Ohnishi and S. Noda

"Band structure observation of of 2D pgotonic crystal with various v shaped air hole arangements"

IEICE Electronics express, **6**, 13, 966, 2009

[11] D. M. Williams, K.M. Groom, D. Childs, R.J.E. Taylor, S. Khamas, R.A. Hogg, B.J Stevens, N. Ikeda, Y. Sugimoto

"Optimisation of coupling between photonic crystal and active elements in an epitaxially regrown GaAs based photonic crystal surface emitting laser"

Japanese Journal of Applied Physics, 51, 02BG05-1-3, February 2012

[12] D. M. Williams, K.M. Groom, D. Childs, R.J.E. Taylor, S. Khamas, R.A. Hogg, B.J. Stevens, N. Ikeda, Y. Sugimoto

"Epitaxially regrown GaAs-based photonic crystal surface emitting laser"

IEEE Photonics Technology Letters, 24, 11, 966-968, June 2012

[13] D. M. Williams, K.M. Groom, B.J Stevens, Q. Jiang, D. Childs, R.J.E. Taylor, S. Khamas, R.A. Hogg, N. Ikeda, Y. Sugimoto

"Realization of a photonic crystal surface emitting laser through GaAs based regrowth"

Proceedings of SPIE – The International Society for Optical engineering, 8255, Jan 2012

[14] K. David, G. Morthier, P. Vanwikelberge, R. Baets, T. wolf and B. Borchert

"Gain-coupled DFB lasers versus index coupled and phase shifted DFB lasers: comparison based on hole burning corrected yield"

IEEE Journal of quantum electronics, **27**, 6, 1991